Power Harvesting Using Piezoelectric Materials

Applications in Helicopter Rotors

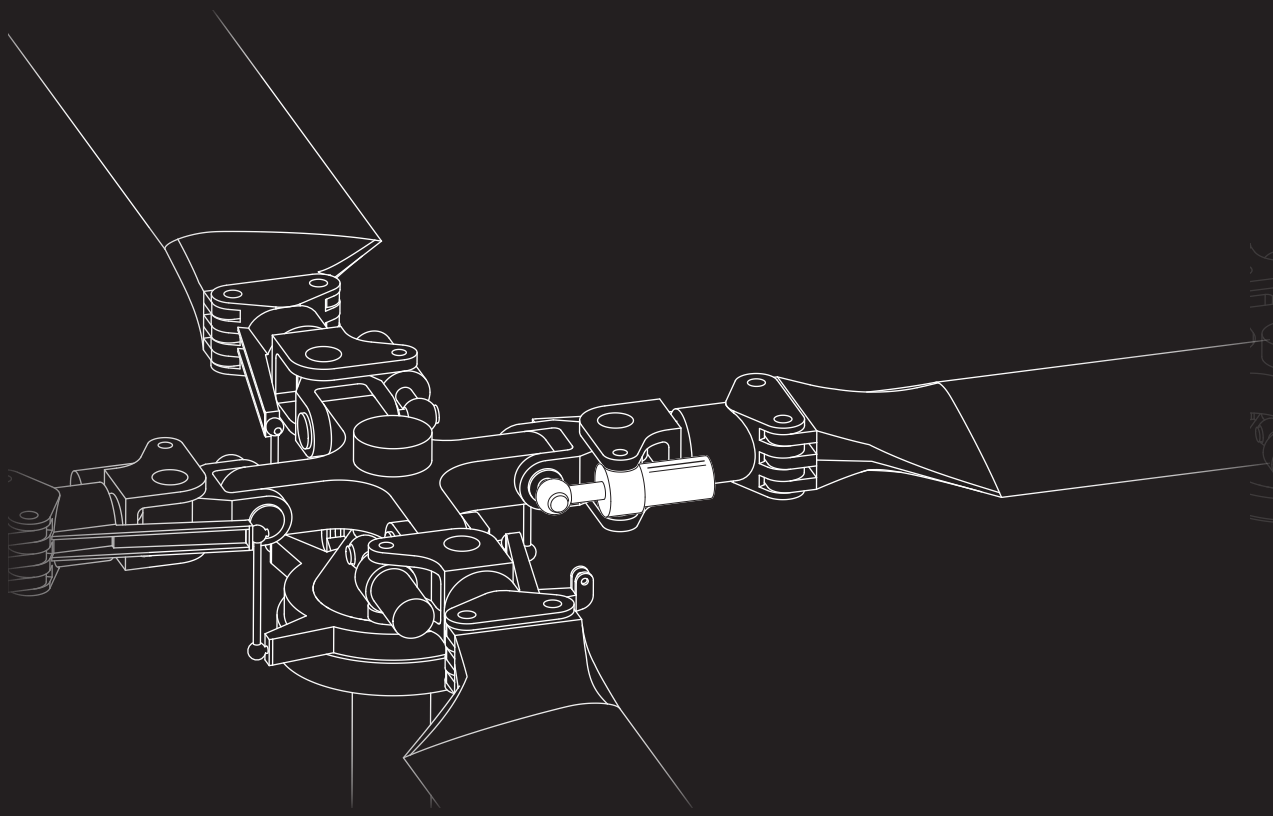

Pieter de Jong

POWER HARVESTING USING PIEZOELECTRIC MATERIALS

APPLICATIONS IN HELICOPTER ROTORS

Pieter Hilbrand de Jong

De promotiecommissie is als volgt samengesteld:

Voorzitter en secretaris:	
Prof. dr. F. Eising	Universiteit Twente
Promotor:	
Prof. dr. ir. A. de Boer	Universiteit Twente
Assistent-promotor:	
Dr. ir. R. Loendersloot	Universiteit Twente
Leden:	
Prof. dr. ir. R. Akkerman	Universiteit Twente
Dr. ir. A. P. Berkhoff	Universiteit Twente
Prof. dr. ir. W. A. Groen	Technische Universiteit Delft
Prof. dr. ing. A. J. H. M. Rijnders	Universiteit Twente
Dr. -Ing. P. Wierach	German Aerospace Center

The work describd in this thesis was performed at the Applied Mechanics group, of the Faculty of Engineering Technology, at the University of Twente, PO Box 217, 7500 AE Enschede, the Netherlands

This project is funded by the Clean Sky Joint Technology Initiative (grant number [CSJU-GAM-GRC- 2008-001]9) - GRC1 Innovative Rotor Blades, which is part of the European Union's 7th Framework Program (FP7/2007-2013).

Power harvesting using piezoelectric materials
de Jong, Pieter Hilbrand
PhD thesis, University of Twente, Enschede, The Netherlands
February 2013

ISBN 978-90-365-3511-3
DOI 10.3990/1.9789036535113
Subject headings: power harvesting, energy harvesting, piezoelectric, rotor craft

Printed by Ipskamp Drukkers B.V., Enschede, The Netherlands

On the cover: A simplified technical drawing of a helicopter rotor, showing the hub, flap and lag hinges, blade root, pitch control and lag damper. Additional cover design by Alexandre Paternoster.

POWER HARVESTING USING PIEZOELECTRIC MATERIALS
APPLICATIONS IN HELICOPTER ROTORS

PROEFSCHRIFT

ter verkrijging van
de graad van doctor aan de Universiteit Twente,
op gezag van de rector magnificus,
prof.dr. H. Brinksma,
volgens besluit van het College voor Promoties
in het openbaar te verdedigen
op donderdag 28 februari 2013 om 14.45 uur

door

Pieter Hilbrand de Jong

geboren op 27 augustus 1983

te Kinderdijk

Dit proefschrift is goedgekeurd door de promotor

Prof. dr. ir. A. de Boer

en assistent-promotor

Dr. ir. R. Loendersloot

Summary

The blades of helicopters are heavily loaded and are critical components. Failure of any one blade will lead to loss of the aircraft. Currently, the technical lifespan of helicopter blades is calculated using a worst-case operation scenario. The consequence is that a blade that may be suitable for, for example, ten thousand flight hours is discarded after only three thousand hours. The costs associated with this practice are enormous. For heavily loaded military aircraft this practice may be a reasonable approach. On the other hand, light duty aircraft in civil aviation may only use the blades for half or one third of the total technical lifespan, incurring unnecessarily high costs. Although the blade life could be extended through more advanced materials, extensive inspection regimes and better design, the uncertainty concerning the blade loads and fatigue issues remains. These options are all very costly.

Measuring systems are required within the blade in order to more accurately follow the actual loads that it is subjected to. In this manner it is possible to monitor the loads, calculate the actual fatigue within the blade and, finally, the end of life can be predicted far more accurately. This will result in blades being used longer, reducing maintenance costs for the operator and lowering the environmental impact of blade manufacturing.

The main challenge is supplying the sensors with electric power. Large rotorcraft have slip rings within the rotor head, supplying power for de-icing systems on the leading edge of the blade. This power is unsuitable for sensing and data processing because it is high voltage, and is not a stable source of power. Additionally, slip rings are maintenance intensive.

The idea proposed in this thesis is to generate the power needed for sensing within the blade itself. Many generation methods are available varying from traditional electromagnetic generators to solid state conversion mechanisms. In this work, piezoelectrics are considered as a candidate to harvest power. Piezoelectric material is a material which develops an electrical charge as it is mechanically stressed. It is shown in this thesis that a useful amount of power can be recovered from the blade when combined with the right electric circuit.

Chapter 3 covers a few basic power harvesting circuits. Two passive circuits are analysed first. Passive relates to the fact that these circuits do not manipulate the voltage of the patch in any way. Then two active circuits are analysed. These do manipulate the voltage in order to increase power output of the component. It is demonstrated that the choice of circuit does not simply mean choosing the one that is the most efficient. Depending on the coupling of the harvester under consideration a passive circuit may suffice, whereas the active variants may suppress the motion so much that less power is harvested.

Two concepts are developed in this thesis. The first, discussed in chapter 4, involves placing patches on the blade surface. Using data provided by Agusta Westland, the placement

of these patches is optimised and an output is determined. Although this concept is possible from a power harvesting point of view, it does not appear to be suitable when the dynamics and requirements of the rotorcraft are taken into account. Further pursuit of this concept must include a more detailed analysis of the dynamics of the blade.

The second concept involves modifying a viscous damper within the rotor (chapter 5). This damper is intended to damp blade oscillations, preventing dangerous resonance modes. By placing a piezoelectric stack in series with the damper, it is exposed to the loads generated by the damper, recovering energy in the form of electricity in the process. The initial investigation indicates that this concept is an excellent candidate in providing electricity for blade monitoring electronics. The concept is minimally intrusive and has a minimal influence on the rotordynamics. The design also excels in simplicity, involving only a stack of material, a spring and electronics. A number of design guidelines are also developed such that the performance is maximised and the effects on the rotorcraft are minimal.

Experimental validation is necessary to confirm the accuracy of the developed models (chapter 6). A setup is constructed with a small stack and a viscous damper. The various electrical circuits (summarised in chapter 3) are tested. The piezoceramic material shows some non-linear behaviour, complicating the study. Despite this, two of the three circuits immediately show acceptable agreement with the developed models.

The third circuit which is tested is more complex. It actively modifies the electrical state of the piezo element such that it increases the output over the other two passive circuits. Due to the complexity of the circuit, a number of challenges are encountered and consequently tackled. The circuit is extensively studied using a second electrical setup. Additional guidelines are formulated with respect to this circuit.

The developed damper concept shows great promise in providing sufficient power for a blade monitoring system. Aside from the concept, this work also provides more insight into the process of developing a power harvesting system.

Samenvatting

Helicopterbladen zijn critische componenten en worden zeer zwaar belast. Het falen van een enkel blad zal onvermijdelijk het verlies van de helicopter tot gevolg hebben. Volgens de huidige stand van de techniek wordt de levensduur van helicopterbladen bepaald aan de hand van een zeer conservatieve berekening waarbij van zeer zwaar gebruik uit wordt gegaan. Het gevolg van deze berekening is dat een blad geschikt is voor tienduizend vlieguren maar deze na slechts drieduizend al wordt afgedankt. De hieraan gerelateerde kosten zijn gigantisch. Voor zwaar belaste militaire helicopters is dit misschien een acceptabele benadering maar voor licht belaste civiele helicopters impliceert dit dat de bladen misschien wel twee- of driemaal langer mee kunnen. Dit vormt een hoge en vermijdbare kostenpost. De technische levensduur van de bladen kan verlengd worden middels betere materialen, uitgebreide inspectieprocedures en beter ontwerp, maar de onzekerheid betreffende de belastingen blijft. Dit zijn allemaal nog altijd dure opties.

Daarom zijn binnen de bladen meetsystemen vereist, zodat de belastingen zeer nauwkeurig in kaart gebracht kunnen worden. Op deze wijze is het mogelijk om de belastingen te meten, de werkelijke vermoeiing van het materiaal te bepalen en uiteindelijk de technische levensduur veel beter te voorspellen. Het resultaat zal zijn dat bladen langer gebruikt kunnen worden waarna de onderhoudskosten zullen dalen en de milieu-effecten van het produceren van deze bladen verminderd wordt.

De grootste uitdaging hierbij is hoe deze sensoren van electriciteit voorzien worden. Grote helicopters gebruiken vaak sleepringen om anti-ijsafzettingssystemen van energie te voorzien. Dit is echter onbruikbaar voor sensoren en data verwerking omdat dit vaak hogere electrische spanningen zijn en dit ook geen stabiele bron van electriciteit is. Bovendien zijn sleepringen zeer onderhoudsintensief.

In dit proefschrift wordt voorgesteld om de vereiste energie voor de sensoren ter plekke op te wekken. Vele technieken zijn mogelijk, variërend van electromagnetische technieken tot solid-state conversie principes. In dit werk wordt piezoelectriciteit voorgesteld als kandidaat voor het opwekken van de energie. Piezoelectrisch materiaal is in staat om een stroom op te wekken wanneer het mechanisch belast wordt. Wanneer dit gekoppeld wordt aan electronica kan een bruikbaar hoeveelheid vermogen opgewekt worden.

Hoofdstuk 3 bespreekt een aantal electrische circuits die aan het piezoelectrisch materiaal gekoppeld kunnen worden. Eerst worden twee zogenaamde passieve circuits besproken. Deze circuits manipuleren op geen enkele wijze de spanning van het element. Vervolgens worden twee actieve circuits behandeld die wel de spanning manipuleren om zo het vermogen te vergroten. Er wordt gedemonstreerd dat het maximaliseren van de output niet zo eenvoudig

is als het kiezen van het meest efficiente circuit. Afhankelijk van de mate van koppeling van het mechanische deel van de harvester voldoet soms een passief circuit al, omdat een actieve circuit de beweging zoveel onderdrukt dat er toch minder vermogen wordt opgewekt.

Twee concepten worden bestudeerd. De eerste, die besproken wordt in hoofdstuk 4, maakt gebruik van piezo electrische plaatjes die op de bladen geplakt worden. Met behulp van data die is aangeleverd door Agusta Westland, wordt de plaatsing van deze plaatjes geoptimaliseerd en kan een opgewekt vermogen berekend worden. Hoewel dit concept bruikbaar is vanuit het oogpunt van het terugwinnen van energie, lijkt deze minder goed toepasbaar wanneer de dynamica en randvoorwaarden van de helicopter in beshcouwing worden genomen. Indien dit concept verder wordt ontwikkeld is een dynamische analyse van het gedrag van het blad een vereiste.

Het tweede concept behelst het aanpassen van een viskeuze demper in de rotor (hoofdstuk 5). De taak van deze demper is het onderdrukken van bepaalde trillingen in de bladen die tot destructieve resonanties kunnen leiden. Door een stuk piezoelectrisch materiaal in serie met de demper te plaatsen wordt deze blootgesteld aan de opgewekte demperkrachten, waarmee vervolgens energie opgewekt kan worden. Het initiële onderzoek suggereert dat dit een uitstekende kandidaat is als energiebron voor een sensornetwerk. Het concept vereist weinig aanpassing van de bestaande componenten en heeft slechts een minimale invloed op de dynamica van het blad. Het concept blinkt ook uit in zijn eenvoud, er is slechts een stuk piezoelectrisch materiaal, een veer en enige electronica nodig. Een aantal ontwerpregels worden ook geformuleerd zodat de prestaties worden gemaximaliseerd en de invloed op de rest van de helicopter geminimaliseerd wordt.

Tevens is experimentele validatie vereist om vast te stellen of de ontwikkelde modellen nauwkeurig zijn, dit wordt gedaan in hoofdstuk 6. Er is een opstelling gebouwd bestaande uit onder andere een kleine viskeuze demper en een stuk piezoelectrisch materiaal. Verschillende electrische circuits (samengevat in hoofdstuk 3) worden getest. De validatie wordt enigszins bemoeilijkt door niet-lineair gedrag van het materiaal. Desondanks laten twee van de drie circuits een acceptabele overeenkomst zien met de ontwikkelde simulatiemodellen.

Het derde circuit is wat complexer van aard. Deze is in staat om de electrische toestand van het piezomateriaal aan te passen, teneinde de opgewekte energie flink te vergroten ten opzichte van de twee eerder genoemde passieve varianten. De complexiteit van het circuit stelt uitdagingen die succesvol worden aangepakt. Het circuit is uitgebreid bestudeerd aan de hand van een tweede opstelling die alleen het electrische gedeelte omvat. Ook uit dit tweede onderzoek volgen een aantal ontwerpregels.

Het ontwikkelde concept is een zeer geschikt ontwerp voor het opwekken van voldoende vermogen voor een blad monitoringssysteem. Naast het ontwikkelen van dit concept biedt dit werk ook veel inzicht in het proces van het ontwerpen van een dergelijk energie-terugwinsysteem.

Contents

Chapter 1

Introduction

1.1 Background

Over time technology advances such that devices become so small that they become portable. Consider the changes from home stereos to portable music players, and from desktop computers to laptops. In engineering, these advances in electronics have opened up new possibilities with regards to sensing: independent and self-sufficient wireless sensor nodes.

The greatest limitation of all these devices is the power supply. Electrochemical batteries must be used to provide energy, but then require regular recharging or replacement. One way to extend the time between recharging sessions is by increasing battery life. Driven by these advances in portable technology battery manufacturers have conducted an enormous amount of research towards increasing battery life, perhaps the most known example being the lithium ion battery, [1]. Another direction is decreasing the power consumption of electronics, which can be signified by improvements in computer processors. The nearly one hundred fold increase in CPU speed over the past 30 years would have been impossible without the miniaturisation and increased efficiency of modern transistors [2].

Another possibility which is quickly maturing is generating the required electricity locally. For demands in the order of kilowatts to a megawatt such methods have existed for years: wind turbines, hydroelectric dams, solar farms, internal combustion engines connected to a generator and so on. On a smaller scale, from microwatts to watts, one may consider kinetic watches, for instance, where a pendulum is connected to a spring or even a miniature generator.

A clear distinction exists between utilising fuel (generation) versus tapping into ambient energy, e.g. wind, wave, solar and kinetic. Techniques that utilise ambient energies are grouped by the term *energy harvesting*: they collect or harvest energy from the surrounding environment. No explicit energetic input is required to generate electricity, as opposed to traditional generating plants which are fuelled by coal, gas or nuclear fuel. Kinetic energy is more complex. This can result from a structure being influenced by the environment or as a side effect of human activity. Vehicles, rotating machinery, man-made structures excited by the wind, and so on. There is a tremendous potential energy source within ambient vibrations.

Vibrations are usually considered a nuisance. They imply that mass is in motion about an equilibrium point, which is typically not desired in structures. The most extreme technical

example is perhaps the Tacoma Narrows Bridge (figure 1.1) that collapsed spectacularly within months of completion due to undesired resonance conditions. In the Netherlands there is the example of the Erasmus Bridge in Rotterdam which showed excessive vibrations under specific wind conditions [3], requiring the retrofitment of dampers. The motion of the Millennium Bridge in London was caused by crossing pedestrians and their natural tendency to seek balance on the vibrating bridge, which required dampers to alleviate the problem. From a design standpoint these vibrations must be avoided or dissipated. This is done through damping, but it is also possible to recover this energy through *vibration based energy harvesting* (VBEH).

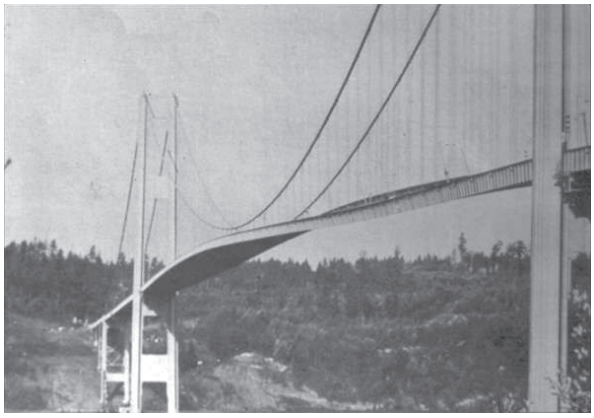

Figure 1.1: Tacoma Narrows Bridge undergoing excessive vibration.

For large scale motions, dampers may be converted to generators by forcing the fluid through turbines, instead of a valve in the piston. Consider using pyroelectric materials to convert a temperature difference (resulting from damping) across the material to an electrical charge, or the use of a linear generator [4]. Harvesting large amounts of energy from these global structure borne vibrations always calls for some mechanical design that requires maintenance.

On a smaller scale of milliwatts to watts, ambient energy may not be so obvious. When such small quantities of energy are desired, the aforementioned mechanical designs are unsuitable. The complexity of and maintenance requirement for a watt-scaled wind turbine or fossil fuel powered generator, for instance, are prohibitive, despite the relatively high energy density of electrical generator based designs. With such a small demand other forms of generation or harvesting, with a lower energy density, are more feasible. This is only true provided the design itself is less complex, cheaper or has few moving parts which require maintenance. Small scale harvesting methods are the main field of operation for vibration based energy harvesting.

It is not only the technical challenge itself which drives the development of VBEH. There is also a pull from industry for independent sensor nodes with respect to *health monitoring*. Nowadays companies strive to maximise the performance of their products. Part of improving performance is predicting the performance and the end of life of components and products,

instead of providing maintenance based on a fixed schedule. This is especially important for more modern materials such as composites where knowledge on fatigue and damage mechanisms is far less developed than metals.

For end of life prediction consider aircraft or rotorcraft whose safe use is strictly limited by phenomena such as material fatigue. This is the case for aircraft fuselages and helicopter rotor blades. Helicopter blades are designed with a technical lifetime of, for example, ten thousand hours [5]. However, they are replaced after only two to three thousand hours [6] to rule out any possibility of failure and loss of the aircraft. Extensive 'traditional' testing on blades in order to establish if they can still be used is not an option. It requires expensive techniques and many man-hours to establish the condition of the components. Costing in the order of millions of euros for a set, doubling the useful life represents an enormous return on investment for the end user when health monitoring systems are used.

This advantage also has an effect on the environment. The purpose of health monitoring in conjunction with power harvesting is to extend the lifetime of components. This means less demand for spare parts. For example, carbon composite parts incur a large cost in production, require a great deal of energy to produce and also require hazardous chemicals during manufacture.

In light of the aforementioned sensor nodes, small scale energy harvesting has the potential to allow for autonomous sensors by utilising a seemingly endless supply of energy. When, for instance, piezo electricity is used a fully maintenance-free unit can be devised due to the absence of relative motion between surfaces or sliding contact (e.g. rolling or sliding bearings). In combination with health monitoring techniques, it will greatly decrease the amount of, or in some cases completely negate the need for, service. Existing unmonitored structures can be equipped with self-powered sensors to establish their residual life. New designs can incorporate sensors in locations which are impossible to reach without major disassembly of the structure. For specific cases where the energy requirement is in the order of microwatts to watts, vibration based energy harvesting may provide the answer.

1.2 Literature review

The current status of VBEH is that of a technology which is just finding its way to commercial use. In the mid 90s one of the first analytic investigations towards power harvesting [7] considered only a generic coupling mechanism for the sake of analysis. Proposed coupling methods included electrostatics, electromagnetics and piezoelectrics. A number of experiments were conducted [8–10], using simple mechanisms in order to investigate the achievable power output in certain situations. Real understanding came around the early 2000s when more structured research was performed, aimed at linking theory to experiment for simple beam-structures [11–14]. The conclusion was also quickly reached that stacks are more difficult to use than patches. Stacks appeared more suitable for low frequency high force excitations [15].

From this point on research began to branch out into various fields. First is the application of advanced circuits, which received an enormous amount of attention [16–27]. The application of advanced circuits allows for more efficient use of the material and greatly boosts power output for non-resonant conditions [19]. Another field is increasing

the bandwidth of systems. This can be done by making a number of different resonators in a single device [28, 29], although this can be considered as installing many harvesters on a single vibration source. A more efficient alternative is a beam that can be tuned during operation as in [30]. Another issue is that piezoelectric harvesters perform better at higher frequency. Systems were devised to upscale the frequency [31, 32]. Another field is that of geometry optimisation. Various geometries, such as beams or cymbals [33], are optimised towards a maximum power per unit volume [34–37].

Power harvesting is also just becoming a commercial business. A number of companies such as Midé and Microstrain are selling energy harvesting packages consisting of a resonant beam, conditioning electronics and a storage medium. The beam is tunable within a certain range to tailor the system to the ambient vibration. Piezoceramic manufacturers are also selling power harvesting demo kits to interested customers, showing the potential of the technique.

Power harvesting is clearly a technique which still needs to find a use in commerce and industry. The knowledge is present but it has not yet been used in a design in such a way that it clearly benefits the overal system.

1.3 Vibration based energy harvesting

In [38] a brief summary is given of the energy density of various generation or energy storage methods which may be used for sensor nodes. It shows that for short periods (months to a year) fixed energy content methods such as batteries or fuel cells are sufficient. Fixed energy methods possess a given amount such as a quantity of fuel or a battery without any charging equipment. As the desired lifespan increases the constant output energy harvesting methods become interesting. These are systems of which the output is a constant amount of power, consider solar cells under constant illumination or windmills under constant wind conditions. However, even when compared to solar energy under less than optimal conditions, vibratory sources are an excellent alternative. The data is summarised in table 1.1.

Table 1.1: Volume normalised power output for various energy storage and harvesting methods [38].

	Technique	Power density (1yr) [$\mu W/cm^3$]	Power density (10yr) [$\mu W/cm^3$]
Constant output	Solar (outdoor)	150-15.000	150 - 15.000
	Solar (indoor)	6	6
	Vibration (piezoelectric)	250	250
	Vibration (electrostatic)	50	50
	Acoustic noise	.003 (75dB) 0.96 (100dB)	.003 (75dB) 0.96 (100dB)
	Thermal gradient	15 (10 ^oC)	15 (10 ^oC)
Fixed content	Non-rechargable lithium battery	45	3.5
	Rechargeable lithium battery	7	0
	Micro heat engine (hydrocarbon)	333	33
	Methanol fuel cell	280	28

As the name indicates, vibration based energy harvesting involves extracting energy from ambient vibrations. An example of various everyday vibration sources with the dominant frequency and acceleration amplitude is given in [39]. It takes little imagination to find vibration sources: rotating machinery always contain an imbalance, bridges are excited by the wind and traffic, and vehicles themselves require dampers to keep the vibrations at a comfortable level. Anything that moves, rotates or is susceptible to air/fluid flow vibrates. When this vibration is essentially undesired it becomes a potential energy source. Currently all these vibrations are damped out. Consider dampers under an automobile, flexible mounts for machinery and in high-rise buildings 'tuned mass dampers' are used to dampen the motion of the top of the building (see figure 1.2).

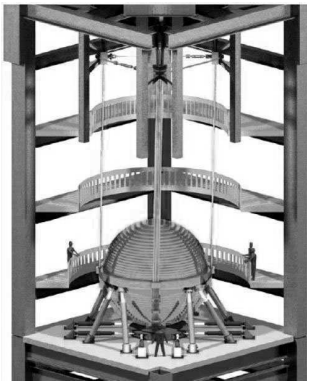

(a) The tuned mass damper in the Taipei-101 skyscraper.

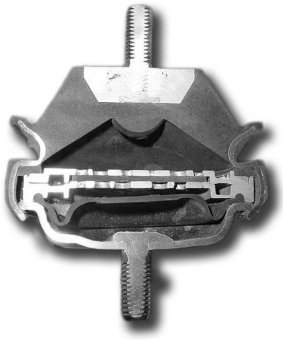

(b) A section view of a hydraulic engine mount.

Figure 1.2: Examples of vibration damping components.

Harvesting energy from these vibrations requires that a transducer, be it electromechanical, electrostatic, piezoelectric or any other technique, be coupled to this vibration. For large amplitude vibrations (> 1 cm) electromechanical methods such as linear generators may be used. The two parts (stator and coil) are then connected to separate components which move relative to each other. A good example of energy recovery using a linear motor / generator is the German (figure 1.3) and Japanese variants of the MagLev train. Although in perception these are motors, they brake electromechanically when approaching a station, recovering a large amount of the energy intitially required to accelerate the vehicle. This principle is also used by hybrid electric vehicles under light braking.

A second mechanical solution concerns vehicles where the dampers in large trucks can generate up to 1 kW per unit which is sufficient to do away with a traditional alternator for electricity generation [40]. Traditionally damping is achieved by forcing oil through an orifice in the piston. The energy harvesting damper instead runs the oil through a turbine connected to a small generator. Under highway conditions this system could generate up to 1 kW per wheel. Considering that a truck and trailer combination can have up to 6 axles, this represents 12 kW of energy which can be recovered.

Figure 1.3: The German MagLev, a big linear motor and generator.

For lower power levels the available methods typically rely on material behaviour and the strain rate, converting mechanical energy into a voltage change or charge displacement. Electrostatics utilises the variation in capacitance of an electrical insulator under tension or compression. Magnetostriction (figure 1.4(a)) works by compressing a material which then generates a magnetic field. By wrapping this material in a coil an electric current is then induced within the coil [41]. A third possibility is to use piezoelectricity (figure 1.4(b)). Here a material is used which can convert mechanical strain directly into an electric current. A number of methods are summarised in table 1.2.

Table 1.2: A number of transduction mechanisms suitable for power harvesting.

Technique	Physical domains	Working principle
Piezoelectricity	Mechanical, electrical	Charge generation resulting from deformation of a polarised atomic structure
Magnetostriction	Mechanical, magnetic, electrical	Change in magnetic field strength due to mechanical load, electromagnetic induction generates a current in the surrounding coil
Electrostriction	Mechanical, electrical	A change in capacitance with a given electrical charge, resulting in a voltage change
Electromechanical	Magnetic, electrical, mechanical	Electromagnetic induction of a coil passing through a magnetic field
Pyroelectricity	Thermal, electrical	Temperature change causes a shift in the atomic structure, generating an electric charge

Of the various techniques of VBEH, piezoelectrics have garnered the majority of research. Magnetostriction is still squarely within the experimental phase and moreover requires more parts than piezoelectrics. Combined with patents on existing magnetostrictive materials [42] and production, cost and availability are prohibitive as well. Electrostrictive techniques are also well developed but simply lack the power density of piezoelectrics. Combined with the knowledge present at the University of Twente with respect to piezoelectric materials it is sensible to pursue piezoelectric based power harvesting.

(a) Conceptual drawing of the main parts of a magnetostrictive transducer (core, coil, and magnetic enclosure).

(b) A piezoelectric patch encapsulated in epoxy (source: PI Ceramic).

Figure 1.4: Two VBEH methods.

1.4 Piezoelectric energy harvesting

As explained in the previous section, power harvesting using piezoelectrics relies on ambient vibration of structures. Piezoelectric material has the ability to convert mechanical strain to an electrical charge (more exact: electrical displacement), and vice versa. When these materials are affixed to a vibrating structure they will experience the same vibrations, thereby generating an electric charge proportional to the mechanical strain input.

The concept is not as far-fetched as it may sound because low-tech devices have been in use for decades. Consider lighters with an electronic spark device: this is in fact a small block of piezo material which the user depresses via a springloaded hammer. The same goes for gas ovens. More subtle uses are in sensing. For example, properly designed piezoelectric strain sensors generate many volts where resistive gauges rely on millivolt changes in the signal, the signal-to-noise ratio is much better in the former case. Accelerometers use a plate of piezo material sandwiched between a base and a seismic mass. The acceleration on the siesmic mass generates a force on the piezo material according to Newton's second law [43], resulting in an electrical charge. The converse effect of converting voltage to a displacement is also widely used. A few examples are nanopositioning systems, fuel injectors for combustion engines, inkjet printers and ultrasonic cleaning baths. The advantages in these fields are nanometer accuracy, high authority due to the large forces which can be generated and the lack of moving parts. In more creative solutions these can be used as linear motors [44].

When used for sensing the piezo material is connected to a very high resistance which prevents any significant current, meaning that the voltage is a direct measure for the strain of the material. By reducing this resistance a current will flow, delivering power to a load; this is the basis of power harvesting. In the mechanical domain the material is attached to a surface which is strained in any fashion, be it harmonic, cyclical or even random. The material undergoes the strain as well, thereby generating the electrical current irrespective of the voltage it must counteract. From basic electrical theory power equals voltage multiplied by current, indicating that electrical power is being transferred out of the piezoelectric material.

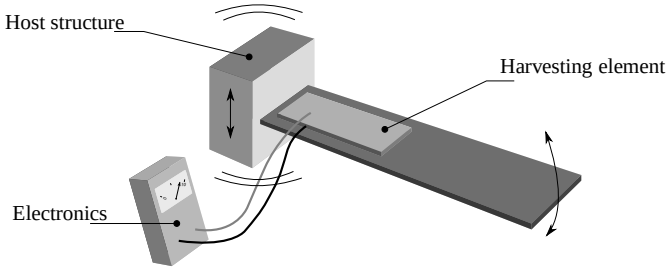

Figure 1.5: Schematic representation of the components of a piezoelectric harvester.

This power can then be used for any number of applications. The scope of this thesis dealswith the mechanical parts and the electronics directly concerned with maximising the output of the system. Here a qualitative description is given of each of the components which will be elaborated on in the modelling chapter.

1.4.1 System components

The difficulty of power harvesting is that different domains –mechanical and electrical– are coupled and influence each other. When the circuitry used also imposes nonlinearities the analysis becomes even more difficult. The components, however, are very distinct and they will first be discussed separately in order to show the influence of each. Figure 1.5 schematically shows the components of a harvester.

Host structure

First is the mechanical structure or vibration source. For the sake of argument we will generally consider a harmonic source. It is possible to use pulsed sources, random excitations indirect sources such as wind [45, 46], and so on. It can be in the form of motors, structures such as bridges or roads [47], rotating shafts, helicopter blades, etc. The host structure is represented by the block on the upper left.

Piezoelectric element

The mechanical portion of the power harvester is affixed to this host structure. Two basic methods can be distinguished and are demonstrated in figure 1.6. First is the direct method where the vibrations from the source are fed directly to the material. In the case of a large motor this would imply installing a stack of material in the base of the motor, bearing the full weight and force of the vibration. This method is difficult to implement because it requires large forces to generate an acceptable current. This method is the most efficient only when the ambient conditions are just right [15, 48].

The second method is indirect and is accomplished by attaching a tuned harvester beam to the host. Its natural frequency is tuned to the dominant or operating frequency of the host structure causing the beam to resonate. The piezo material is attached as an additional layer at the base of the beam and is stressed as the beam flexes. From traditional beam theory,

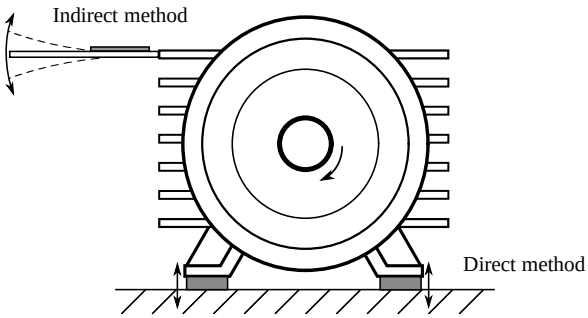

Figure 1.6: The direct and indirect methods demonstrated on an electric motor, piezo elements in grey.

it is known that the harvester beam can generate high stresses in the piezo material using a modest external force or displacement. This makes the latter method more efficient for the vast majority of applications.

Electronics

The next component of a harvester system is the electrical circuitry. In figure 1.5 this is simply represented as a voltage meter. In chapter 3 a number of circuits will be explored, here only a qualitative discussion is given.

Although it would suffice to simply use a resistor to dissipate energy, this is only done in an experimental phase to characterise the harvester as this represents the only possible linear system. In the interest of optimising the harvested power, advanced electrical circuitry must be used. Depending on the scale of the harvester, one may use passive circuits for microscale systems. As the output increases to the order of milliwatts and beyond, there is enough power available for active circuits that require some power to function. The advantage of active circuits is that they artificially increase the electromechanical coupling by modifying the voltage of the piezo material. The goal of the circuitry is to maximise, or optimise, the mechanical damping effect of the piezoelectric material on the rest of the structure. This issue will be addressed and demonstrated in more detail in chapters 2 and 3.

All circuits have one aspect in common, which is a storage element which buffers an amount of harvested energy. The electronics between the piezo element and this storage capacitor are designed to optimise the power flow from the element to the capacitor. On the other side, more electronics are used after this element to condition the voltage for the sensor node; however, this is beyond the scope of this research. In this thesis the conditioning electronics are replaced by a resistor where the harvested energy is dissipated. This simplified electrical load is the end point of this thesis. Figure 1.7 schematically shows the scope of this work.

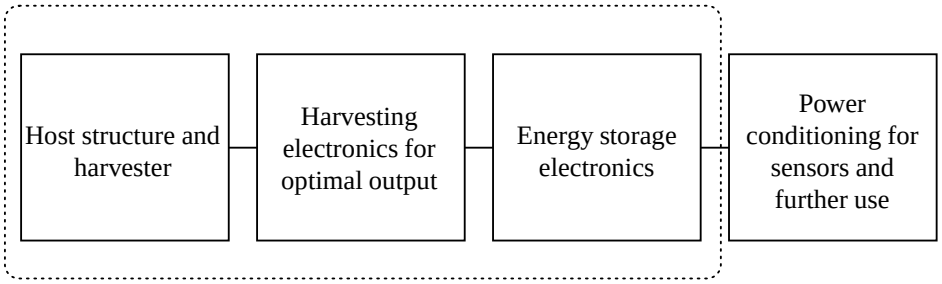

Figure 1.7: Schematic of power harvesting components and scope of this thesis.

1.4.2 Usage criteria

Piezoelectric power harvesting is a technique which in itself does not yield an amount of energy which is useful for consumer use. The specific output –the power per unit weight or unit volume– of these systems is quite low. It will not provide lighting, entertainment or the power to drive machines. Typically, the indirect savings or the increased sensing capability is what makes these systems worthwhile. The following criteria sum up scenarios where power harvesting is a viable option:

1. Crossing boundaries. Consider the presence of rotating joints such as axles in trains and rotors in generators or aircraft where physical connections are difficult, sensitive or expensive. Local generation and wireless transmission of data is a good alternative.

2. Difficult to reach spaces such as the internals of small equipment. Consider components which require significant disassembly to reach.

3. Systems where other techniques are excessive. A windmill or solar cell scaled to generate milliwatts is possible but inefficient, requires maintenance and may vary significantly in output. Power harvesting is virtually maintenance free and an eternal source in the case of large structures.

4. Environments where it may be possible to install wiring but which are sufficiently remote to drive up the costs to make power harvesting an economical alternative. Consider remote un-powered structures such as bridges, small dams in rural areas, etc.

5. Remote locations where a service call imposes significant cost in man-hours, fuel or funds. Rural areas, the tops of bridge support towers, and so on.

Generally, a combination of these criteria may be possible. Note that some form of sensing is always assumed, otherwise power harvesting would be useless. The following section gives some examples and demonstrates the various criteria.

1.4.3 Examples

The value of power harvesting can easily be demonstrated based on a few examples. One use could be in bridges. Bridges are very flexible structures and are excited by the wind, water, and traffic. Even the myth of soldiers having to break step while crossing bridges has some technical basis. One need only look at the Millennium Bridge and Tacoma Narrows Bridge mentioned previously to understand this. These vibrations can be used to generate electricity to power sensors. One could imagine that it may be just as simple to install a power line on the bridge to supply sensors with power. This may be true to some extent for new bridges but in the Netherlands, for instance, many bridges are aging or are located in a rural area with no immediate access to the electrical grid. Providing this connection is far more costly than engineering a power harvesting solution. Relevant criteria are 3, 4 and 5.

A second example would be vehicle tyre pressure monitoring systems, or TPMS. In the case of direct pressure sensing –as opposed to frequency or speed based deduction, which is less reliable– a power source is required to power the pressure sensor within the wheel. It is far too costly and/or unreliable to install a hard connection to the vehicle power supply, making battery power the next best option. These batteries must be replaced occasionally, which requires the tyre to be removed from the rim in order to access the sensor. The use of a self-sufficient sensor will make for a more reliable system. The first production vehicle to include a direct TPMS was the Porsche 959 in 1986, but today TPMS is being required by law around the world in more and more countries. The cost disadvantage of a harvester solution could, for the most part, be offset by a standardised and mass-produced system. Relevant criteria are 1, 2 and 5.

For this thesis the most important example is that of helicopters. The rotor blades of helicopters are critical components which cannot be permitted to fail. The current practice is to replace these based on a very conservative lifetime calculation. As indicated previously the blades are designed for, for example, 10,000 hours but they are replaced within only two or three thousand hours of operation [5, 6]. Employing sensors to monitor the loads and condition of the blades could greatly improve the lifetime prediction through fatigue analysis. The cost savings over the lifespan of one helicopter can be significant for medium to large craft. These may have the blades replaced a number of times in their life at a cost of millions of euros on each occasion. Similar to the tyre monitoring system, the prospect of a rotating joint is an issue but larger helicopters do have slip rings to transmit power to the blades for de-icing systems. However, this power is too unstable for sensing and to return the data, again, some hard connection accommodating rotation is required. Only criteria 1 is truly relevant here, in this case the cost savings are the benefit.

1.5 Industrial partners

The University of Twente is a partner of the JTI Clean Sky project, funded by the 7^{th} Framework Program. The goal of the project is to improve air transport through various Integrated Technology Development (ITD) programs. The programs cover various fields such as: more efficient design, advanced materials, fixed wing aircraft and rotorcraft. UTwente is also involved in a number of ITDs, among others Green RotorCraft (GRC) and Ecodesign. The power harvesting research falls within the GRC ITD program.

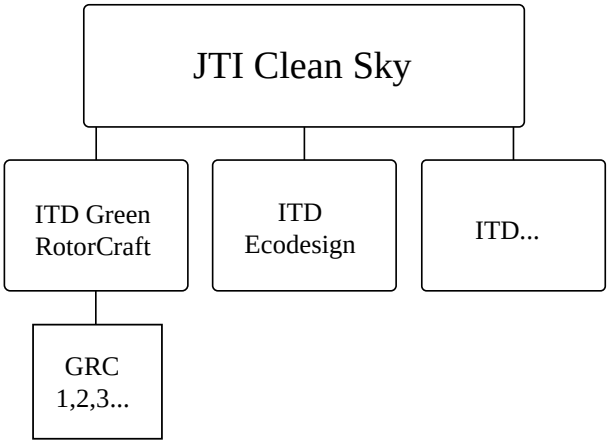

Figure 1.8: Clean Sky project structure.

The research presented in this thesis falls within GRC1. The university, in cooperation with a number of companies and institutions from the Benelux have formed the IGOR consortium to research various rotor blade systems. Power harvesting is one of the selected techniques.

1.6 Research goals

The University of Twente, in the form of the Applied Mechanics group, also wishes to expand its expertise to the field of piezo materials for sensing, actuation and power harvesting. Some initial studies were performed in 2008 [49]. A position dedicated to power harvesting was created and the group has subsequently participated in two projects in cooperation with other parties.

The University of Twente is a partner within the GRC project, in conjuction with *Agusta Westland* and other companies. Given the expertise within UTwente, power harvesting was considered as a viable method to generate power in AW's helicopter rotor blades for health monitoring equipment.

To this end the following research goals are established in this thesis:

- Develop a fundamental understanding of power harvesting. This is done through basic analytical modelling, literature review and analysis of power harvesting circuitry.
- Explore the potential for power harvesting in the rotor of a helicopter. Establish the most promising concept with respect to reliability, safety and aerodynamic stability.
- Modelling, simulation and optimisation of a power harvesting device for use in a helicopter rotor. See previous goal.
- Validation: Experimental validation of the proposed concept and performed simulations.

- Application development: design and realisation of an experimental setup for harvesting energy. Establish guidelines for the design of harvester systems. Explore the potential for a basic rule of thumb to estimate power output of a concept.

1.7 Thesis outline

This thesis covers certain aspects of the topic of power harvesting and selected applications. First, the concept of piezoelectricity and the mechanical background of power harvesting is elucidated in chapter 2. Various actuation modes and material properties will be discussed as well as the basic linear equations. Finally, a number of fundamental parameters such as electromechanical coupling and normalised output will be introduced. This relates mostly to research goal 1.

Due to the substantial content of electrical circuitry, a basic introduction is given in chapter 3. The topics cover basic linear components, AC / DC power and a functional description of a few basic semiconductors. Following this introduction the relevant circuits are addressed; basic functioning and the first design considerations towards implementing these in real designs are discussed.

In chapter 4 the GRC project is properly introduced. Research is performed on the main rotor blades of a helicopter. The application under investigation involves placing piezo patches on the blade surface. Dynamic data from a rotor dynamic model is provided as an input as opposed to performing a full coupled aerodynamic/structural/piezoelectric analysis. This assumption is validated. The work is on a conceptual level and this concept was decided not to pursue this concept further due to the aerodynamic properties and related stability issues that the concept would interfere with. This chapter is relevant to the second research goal.

Chapter 5 presents the second concept developed within the GRC project. The design involves modifying a viscous damper which is present in most helicopters. The purpose of this component is to suppress certain resonance modes which are unavoidable in rotorcraft. The damper is adapted to include a piezoelectric stack. A complete concept is presented, spanning the mechanical and electrical domains, as well as considering the various electrical circuits presented in chapter 3. The influence of the different parameters is investigated as well as some potential non-linear variables pertaining to the piezo material. Equations and design rules are formulated to maximise the output of the concept. This chapter relates to the second and third research goals.

The extensive simulation of chapter 5 is validated with a laboratory scale setup, presented in chapter 6. A setup is built consisting of a viscous damper, piezoelectric stack and a large shaker providing the excitation. A number of circuits from chapter 3 are investigated and compared with simulations of the setup. Two circuits are succesfully validated with this setup and a third requires additional work with respect to the electronics. The circuit is studied, modified and improved for use within the lag damper concept. Design guidelines are formulated. This chapter relates to the second, third and fourth research goals.

Conclusions and recommendations are finally presented in chapter 7.

Chapter 2

Power harvesting theory

2.1 The piezoelectric effect

The piezoelectric effect was discovered in 1880 by Pierre and Jacques Curie [50]. They found that certain materials had the ability to convert mechanical stress to electrical charge. The converse effect was predicted one year later and subsequently confirmed by the Curie brothers. In 30 years the discovery was put into practice with the development of a piezoelectric based sonar or hydrophone. The cause of this phenomenon was found to lie in the atomic structure.

For ease of discussion only ceramic materials are considered, unless otherwise mentioned. Ceramic materials are defined as 'inorganic non-metallic solids prepared by heating and subsequent cooling'. Ceramics exist as non-crystalline materials such as glass, crystalline and polycrystalline materials. The mechanical properties typically include excellent compression capabilities and an inability to handle tensile and shear stresses. Ceramics withstand strong chemical corrosion and high temperatures. Although ceramics are typically associated with cookery, it also has highly technical uses in tooling, thermal engineering and precision mechanics. Components are produced by means of a forming process, followed by firing at temperatures up to 1400°C. Piezoceramics are classified as a composite ceramic. They are usually formed by pressing the powdered consituent materials in a form, followed by sintering. This process leads to a polycrystalline structure.

Modern ceramic piezoelectric materials are predominantly lead zirconate titanates, or PZTs. The constituent atoms are ordered in a *perovskite* structure. Figure 2.1 shows the basic unit element at elevated temperature. This is a cubic structure with large metallic atoms on the corners (in this case lead), face centred oxygen atoms and a zirconium or titanium atom in the centre. In most PZTs both Zr and Ti are used simultaneously and the ratio can be used to fine-tune the material for specific purposes.

Each element has a different electrical charge in the structure: lead takes a 2+ charge, zirconium/titanium a 4+ charge, and each oxygen atom assumes a 2- charge. Positively charged atoms are known as cations, and negatively charged elements are anions. This leads to the following chemical designation: $Pb(Zr_xTi_{(1-x)})O_3$, with x between 0 and 1. Note that this ratio is not obvious from the figure, but for a real material structure consisting of countless unit cells this is the case.

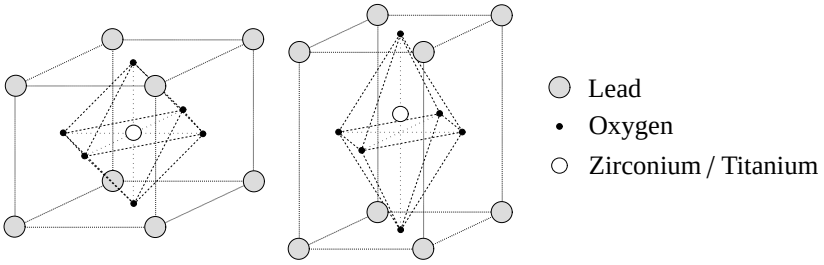

Figure 2.1: Atomic structure for $T > T_c$ (left) and $T < T_c$ (right).

The piezoelectric effect arises due to asymmetry created by the central zirconium/titanium atom. Above a certain temperature, known as the *Curie temperature*, the atom is in the centre. This leads to a uniform distribution of the positive and negative charges within the structure. When the material is cooled to below the Curie temperature, the central atom moves away randomly towards one of the oxygen anions because the central position is an unstable position. Within one crystal all atoms move in the same direction. This has two effects. First, it distorts the atomic structure resulting in the perovskite structure which is anisotropic. Secondly, because the central atom is not located exactly in the centre, the centres of positive and negative charge no longer coincide, leading to a dipole moment. Due to the resulting asymmetry a polarisation of the material occurs which is defined positive in the direction of the displacement of the central atom.

In nature the crystal orientations within bulk material are random, nearly neutralising the charge imbalances over the entire specimen. Figure 2.2 shows the grain structure (meso scale) and domain structure (micro scale) of Barium Titanate, another type of piezo ceramic. The larger structures in the figure represent the material grains and the smaller parallel structures are the individual domains. Within each domain a uniform polarisation exists. The macro scale polarisation, however, is zero.

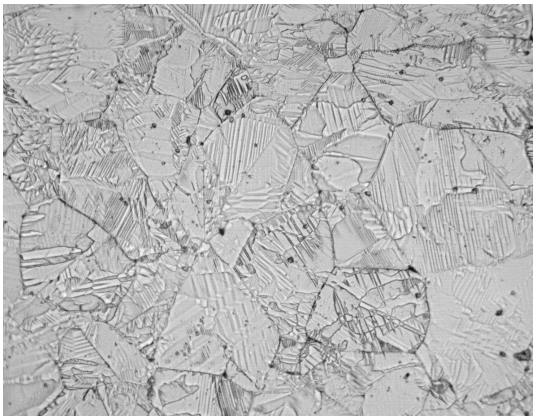

Figure 2.2: Microscope image of the structure of Barium Titanate. [51]

For a useful piezoelectric effect, all the crystal domains must be oriented in roughly the same direction. To accomplish this, the material is typically put under a voltage at elevated temperatures. The voltage is then maintained as the temperature is decreased to ambient values. This locks the orientation of the piezoelectric domains in the direction of the applied voltage. This random and oriented polarisation is demonstrated in figure 2.3.

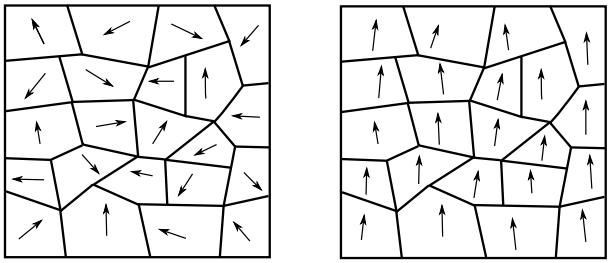

Figure 2.3: Schematic representation of the crystalline structure and polarisation domains before (left) and after (right) polarisation.

This polarisation is not permanent regardless of the ambient conditions. The Curie temperature immediately implies that, as the temperature is increased, the material has a less profound piezoelectric effect. More specifically: it becomes less tolerant of voltages which are applied in the opposite direction. If too high a voltage is applied the Ti/Zi atoms can be displaced to another equilibrium state, changing the polarisation of the affected domain. The negative voltage below which a spontaneous change in polarisation occurs is the *coercive field strength*. By applying a voltage lower than this voltage the polarisation is forcefully reversed. This value reaches zero when the temperature approaches the Curie temperature.

The polarisation direction also implies that the effect is anisotropic. Toward this end a standard local coordinate system is introduced in the material. The 3 axis is always positive in the polarisation direction. The 1 and 2 axes can then be chosen arbitrarily, but perpendicular to the 3 axis, assuming a right-handed coordinate system. For simplicity a block of material is considered, making it useful to orient the 1 and 2 axes along the edges. The standard axis notation is given in figure 2.4. Note that for clarity the deformed shape under a positively applied voltage along the 3 direction is given.

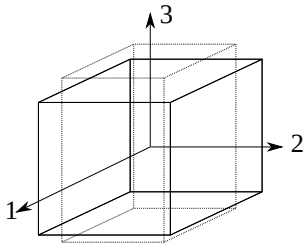

Figure 2.4: Standard axis notation for piezoelectric material. Polarisation in 3 direction.

In order to make use of the piezoelectric effect, a voltage must be applied along the 3 axis. This is done by applying electrodes on the surfaces perpendicular to the 3 axis. An added effect is that of electrical capacitance. This is a property which results from two parallel electrodes with a *dielectric* in between. Capacitance is the electrical equivalent to a mechanical compliance and is denoted in Farad [F]. The capacitance relates how much current or charge is required to generate a desired voltage between the electrodes.

Piezo material can be used in 3 ways: the 33 mode, 31 mode and 15 mode. The first digit denotes the axis along which a voltage is applied, and the second digit signifies the resulting strain. The first two modes are of interest in this research. In the 33 mode the voltage along the polarisation axis leads to a deformation along that axis. This mode typically exhibits the largest piezoelectric effect of the various operation modes. The maximum achievable strain is typically in the order of one to two thousandths extension. The 31 mode utilises the lateral contraction resulting from the strain along the third axis and the effect is appromately half as strong for the same voltage field. Due to symmetry of the unit cell, the 32 mode is identical to the 31 mode and is not explicitly mentioned or calculated.

The 15 mode also exists but, as the indices indicate, it requires the electrodes to be perpendicular to the 1 axis. This mode utilises shear deformation in the 31 plane. The shorthand notation is 15. As with the 31 mode of operation, symmetry conditions imply that the 24 mode demonstrates similar behaviour. A voltage field along the 2-axis induces a shear in the 23 plane. This mode is not addressed any further in this thesis.

Utilising these modes requires different types of geometries for the respective actuator. The 31 mode is generally used in the form of a patch. The third axis is the thickness direction and the other two dimensions are comparatively large. Electrodes are applied over the large top and bottom surface. The patch is then bonded to a plate or beam structure. Applying a voltage will then deform the material in between the electrodes.

The 33 mode could, for a long time, only be used by making stacks. Chips of material are stacked, along the 3 axis, with electrodes in between which alternate polarity. The length, along the 3 direction, is typically larger than the cross section of the stack. These two basic geometries are shown in figure 2.5. Modern manufacturing techniques have allowed for patches to be manufactured which utilise the 33 mode. These are, among others, known under the terms AFC, MFC, and DuraAct.

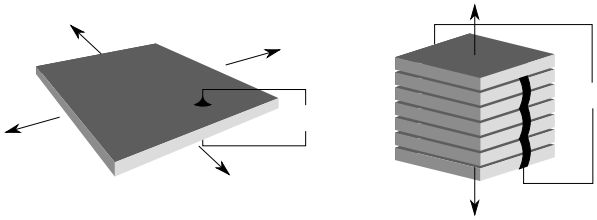

Figure 2.5: Impression of a patch (left) and stack actuator (right).

With this basic knowledge of the phenomenon of piezoelectricity, a standard coordinate system and actuation modes, equations can be derived in order to accurately describe the behaviour of this material.

2.2 Constitutive equations

Consider an infinitesimal piece of piezoelectric material such as in figure 2.4 with a given uniform polarisation, quantified by the matrix **e**. The following constitutive equations – converted from tensor to matrix notation– then define the force and charge equilibrium of the element [52]:

$$\boldsymbol{\sigma} = \mathbf{C}^E \boldsymbol{\varepsilon} - \mathbf{e}^T \mathbf{E}_v \tag{2.1a}$$

$$\mathbf{D} = \mathbf{e}\boldsymbol{\varepsilon} + \boldsymbol{\epsilon}^{\varepsilon} \mathbf{E}_v \tag{2.1b}$$

Variables σ, $\mathbf{C}^E$, $\boldsymbol{\varepsilon}$, $\mathbf{E}_v$ $\mathbf{D}$ and $\boldsymbol{\epsilon}^{\varepsilon}$, represent the stress vector, elasticity matrix, strain vector, voltage field vector [V/m], electric displacement field [C/m^2] and permittivity matrix [F/m] at constant mechanical strain. Refer to chapter 3 for a detailed discussion of the electrical domain and its variables. There are three other variations of the piezoelectric equations, these are summarised in appendix A. For the majority of this thesis, the *e*-formulation is used, as presented here.

Upon close inspection, the first equation reveals Hooke's law describing the mechanical domain. The stress and strain vectors are therefore:

$$\boldsymbol{\sigma} = \begin{pmatrix} \sigma_{11} \\ \sigma_{22} \\ \sigma_{33} \\ \sigma_{23} \\ \sigma_{31} \\ \sigma_{12} \end{pmatrix}, \qquad \boldsymbol{\varepsilon} = \begin{pmatrix} \varepsilon_{11} \\ \varepsilon_{22} \\ \varepsilon_{33} \\ 2\varepsilon_{23} \\ 2\varepsilon_{31} \\ 2\varepsilon_{12} \end{pmatrix} \tag{2.2}$$

The elasticity matrix $\mathbf{C}^E$ is a 6 by 6 matrix. It contains the elasticity constants at a constant electrical field. Due to symmetries present in the structure of the unit cell, this simplifies to the following matrix with 6 independent elasticity values:

$$\mathbf{C}^E = \begin{bmatrix} C_{11}^E & C_{12}^E & C_{13}^E & 0 & 0 & 0 \\ C_{12}^E & C_{11}^E & C_{13}^E & 0 & 0 & 0 \\ C_{13}^E & C_{13}^E & C_{33}^E & 0 & 0 & 0 \\ 0 & 0 & 0 & C_{44}^E & 0 & 0 \\ 0 & 0 & 0 & 0 & C_{44}^E & 0 \\ 0 & 0 & 0 & 0 & 0 & C_{66}^E \end{bmatrix} \tag{2.3}$$

The second part of the first equation is the stress generated by the piezoelectric effect. It is dependent on the voltage field within the material. Again, considering the atomic structure, simplifications in the number of material parameters are already included. These matrices are then defined as follows:

$$\mathbf{e} = \begin{bmatrix} 0 & 0 & 0 & 0 & e_{15} & 0 \\ 0 & 0 & 0 & e_{15} & 0 & 0 \\ e_{13} & e_{13} & e_{33} & 0 & 0 & 0 \end{bmatrix}, \qquad \mathbf{E}_v = \begin{pmatrix} E_{v1} \\ E_{v2} \\ E_{v3} \end{pmatrix} \tag{2.4}$$

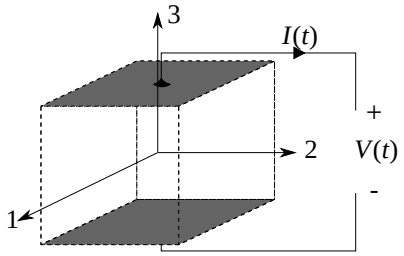

Figure 2.6: Model for the 1D piezoelectric element.

The identical performance of e_{13} and e_{23} becomes clear when inspecting the unit cell of figure 2.1, as there is no difference between the structure along the 1 and 2 axis. The same goes for e_{15} and e_{24} which represent shear in the 31 and 23 plane.

The 3 values for the electrical field denote an electrical field oriented along the individual axes of the local coordinate system of the material. From the **e** matrix it becomes clear that it is also possible to impose a shear deformation in the material by applying a voltage along the 1 or 2 axes. However, this aspect will not be addressed further in this work.

The second equation represents an electrical charge balance. In solid mechanics there is a force equilibrium when statics are concerned. This equation represents the electrical equivalent, with **D** and $\mathbf{E}_v$ the equivalencies to the strain and stress, respectively. The electrical permittivity of the material $\boldsymbol{\epsilon}^{\varepsilon}$ is the electrical equivalent of mechanical elasticity. When the material is compressed, the charge displaced by the piezoelectric effect builds up on the electrodes perpendicular to the 3 axis, resulting in an increase in the voltage. The mechanical equivalent is compressing a spring which requires a force to maintain the displacement. The electric flux density, permittivity and voltage field have no coupled terms and are then defined as:

$$\mathbf{D} = \begin{pmatrix} D_1 \\ D_2 \\ D_3 \end{pmatrix}, \qquad \boldsymbol{\epsilon}^{\varepsilon} = \begin{pmatrix} \epsilon_1 & 0 & 0 \\ 0 & \epsilon_2 & 0 \\ 0 & 0 & \epsilon_3 \end{pmatrix} \tag{2.5}$$

These equations fully describe the behaviour of linear piezoelectric material. In the next section more useful equations for actual applications will be investigated.

2.3 Equations for piezo elements

A piezo element will have finite dimensions and only 2 electrodes, leading to a single capacitance value. To make the equations of the previous section applicable to a patch or stack actuator, the dimensions of the component must be taken into account. The full derivation is given for the 33 mode of operation assuming a monolithic element. The equation for 31 mode operation can be derived in a similar fashion. The results for additional modes of operation and stacks are listed in appendix B. The element under consideration is shown in figure 2.6.

The 1D stiffness is denoted using the Young's modulus E_{33}^{E}. Because of the application of 2 electrodes perpendicular to the 3 axis, only one charge equilibrium equation is relevant:

D_3. The others are equal to zero. Additionally, shear does not lead to a charge displacement along the 3 axis, so for the constitutive equations all shear terms can be neglected. With the **e** matrix then only containing terms in the third row, only one electrical equation remains.

Instead of a voltage field, a voltage V_p is applied. From electrostatics the voltage at a point within a uniform electric field between parallel plates is given by $E_v = -Vd$, with d the distance from the grounded plate. Since the voltage across the entire material is desired, d is substituted with the thickness of the material t_l. The dimensionless strain is replaced by the deformation divided by the original length. Lastly, consider an element with a loaded surface area A perpendicular to the 3 axis and thickness t_l, along the 3 axis. With all these substitutions the following equations are found:

$$\frac{F}{A} = E_{33}^E \frac{\Delta t_l}{t_l} + e_{33} \frac{V_p}{t_l} \tag{2.6a}$$

$$\frac{Q_3}{A} = e_{33} \frac{\Delta t_l}{t_l} - \epsilon^\varepsilon \frac{V_p}{t_l} \tag{2.6b}$$

The variable Q_3 represents the charge displacement and is defined as $Q_3 = D_3 A$. The elasticity term C_{33}^E is replaced by the 1D elasticity E^E. In engineering applications, the interesting parameters are the piezo displacement Δt_l, force F, applied voltage V_p and for power harvesting purposes also the current I. From electrical engineering it is known that $I = dQ/dt$ [53], requiring that the electrical equation be derived to the time. These are chosen as the element variables resulting in:

$$F = \frac{E_{33}^E A}{t_l} \Delta t_l + \frac{e_{33} A}{t_l} V_p \tag{2.7a}$$

$$I = \frac{e_{33} A}{t_l} \Delta \dot{t}_l - \frac{\epsilon_3^\varepsilon A}{t_l} \dot{V}_p \tag{2.7b}$$

Equations 2.7 reveal a number of physical quantities of the piezo element. First is the mechanical stiffness $k_p = E_{33}^E A/t_l$ of the element. Second is the capacitance $C_p = \epsilon_3^\varepsilon A/t_l$ of the element. The last parameter is the piezoelectric constant $\theta = e_{33} A/t_l$, unit [N/V]. It directly links the applied voltage to a piezoelectrically generated force. The following basic equation can be written for a piezoelectric element:

$$F = k_p u + \theta V_p \tag{2.8a}$$

$$I = \theta \dot{u} - C_p \dot{V}_p \tag{2.8b}$$

where the elongation Δt_l is substituted by the displacement u. Based on these basic equations it is now possible to investigate the various modes of operation.

2.4 Modes of operation

In chapter 1 various uses of piezo material are mentioned, as sensors, actuators or harvesters. The consequences of each mode of operation on the constitutive equations are presented in this section.

2.4.1 Actuators and sensors

When used as actuators the piezo element is driven by a set voltage. The electrical equation of 2.8b becomes obsolete, leaving only the mechanical domain to be evaluated. The electrical domain is, of course, still there but the driver supplies the necessary current to achieve the set voltage. Thus remains:

$$F = k_p u + \theta V_p \tag{2.9}$$

When used as a sensor a very high resistance is connected to the electrodes of the piezo element. This resistance is sufficiently large such that the current flow is negligible, creating what is called an *open circuit* condition. When the material is stressed mechanically the resulting current cannot flow from the element. All displaced charge must be stored on the electrodes of the material leading to a voltage increase across the electrodes. This leads to the following equations:

$$F = k_p u + \theta V_p \tag{2.10a}$$
$$0 = \theta u - C_p V_p \tag{2.10b}$$

Note that with the current being zero, it is possible to integrate the function describing the electrical domain, rewriting it in terms of voltage and displacement. The electrical equation is now written in terms of a charge balance.

2.4.2 Harvesting mode

From basic electronics, the electrical power is dissipated in a resistor because there is current through as well as voltage across it: $P = VI$. Just as in the mechanical domain, power is transmitted only when a force as well as a velocity are present. To this end a resistor with finite value R, (unit Ohm, symbol [Ω]) is connected across the electrodes of the piezo element. From Ohm's law [54] this relation is $V = IR$. The piezo electric equations are then as follows:

$$F = k_p u + \theta V_p \tag{2.11a}$$
$$V_p/R = \theta u - C_p V_p \tag{2.11b}$$

These last equations represent the most basic form of power harvesting using only a resistor in alternating current (AC) mode. In the next two sections the concept of coupling and its influence on harvested power in a 1D dynamic model are investigated.

2.5 Electromechanical coupling

The constitutive equations 2.1 and element equations (2.8) of the previous sections show that there is a two-way coupling between the mechanical and electrical domains. An applied force will generate a voltage, and a voltage will result in a force. This effect can be minimal or profound depending on the performance of the material and the electrical operation, open or closed circuit, or something in between using a finite resistance value.

First, this effect is quantified using a dimensionless parameter and assuming open circuit operation, such as in equations 2.10b. Contrary to previous research at the University of Twente [55], here a linear displacement field within the element is considered, instead of solving the internal wave equation. To determine the coupling parameter the equations must be condensed to a single one. A homogeneous bar of piezoelectric material under a 1D loading along the 3 axis and 33 mode operation is presumed. First the electrical equation of equations 2.8 is written as a function of E_{v3}:

$$E_{v3} = \frac{e_{33}\varepsilon_{33}}{\epsilon_3^{\varepsilon}} \tag{2.12}$$

This is substituted back in to the mechanical domain resulting in:

$$\sigma_{33} = E_{33}^{E}\varepsilon_{33} + e_{33}\frac{e_{33}\varepsilon_{33}}{\epsilon_3^{\varepsilon}} \tag{2.13}$$

Recall that, this being a 1D equation, the equivalent elasticity E^E is used. Rearranging then yields:

$$\sigma_{33} = E_{33}^{E}\varepsilon_{33}\left(1 + \frac{e_{33}^2}{E_{33}^{E}\epsilon_3^{\varepsilon}}\right) \tag{2.14}$$

The dimensionless value $e_{33}^2/\left(E^E\epsilon_3^{\varepsilon}\right)$ is of special importance and is defined as the electromechanical coupling. Here it can be substitued by k_{33}^2, with the subscript again indicating the mode of operation. The coupling is a measure for the influence of the electrical domain. A high piezoelectric coefficient, low permittivity and elasticity lead to a pronounced influence, ie. when applying a force to the material a larger portion of the reaction force is due to the piezoelectric effect, when an open circuit is considered. In this case it leads to an apparent increase in material stiffness.

A similar derivation can be done for a lumped 1D model such as equation 2.8, leading to the following description of electromechanical coupling for a lumped parameter model:

$$k_e^2 = \theta^2/\left(k_p C_p\right) \tag{2.15}$$

For lumped cases and experimental characterisation, k_e^2 is generally used to indicate the electromechanical coupling. Although the operation mode may be known, the setup will result in a value different than that resulting from the material parameters.

The equation of the electromechanical coupling can be reproduced using the definitions for θ, k_p and C_p from section 2.3. This is only valid when the element under consideration is homogeneous and fully active piezo material. With the definition of the dimensionless

coupling in mind it is now possible to describe the behaviour of a simple 1D AC power harvester.

2.6 Power harvested in AC mode

Consider a 1D mass-spring model incorporating a piezo element in parallel with a mechanical stiffness, as in figure 2.7. A harmonic force excitation is assumed. The influence of the electromechanical coupling on dynamic systems will be investigated using this model.

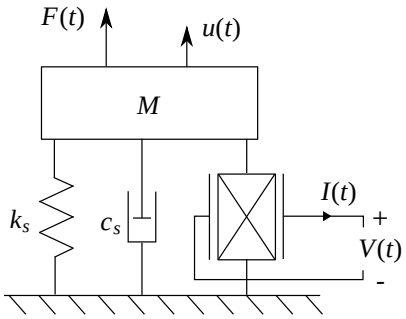

Figure 2.7: Ideal Physical Model of a 1D dynamic system with a piezo element.

The variables k_s, c_s and M represent the mechanical stiffness, viscous damping of the system, and mass. The piezo element is on the right. Only the lumped piezoelectric parameter θ is considered for this evaluation. Also a resistor R is immediately included across the electrodes of the piezo element. The equations of motion for this system are:

$$M\ddot{u} + c_s\dot{u} + k_p u + \theta V_p = F(t) \tag{2.16a}$$

$$\theta\dot{u} - C_p\dot{V}_p = V_p/R \tag{2.16b}$$

First the second equation is written as to solve the voltage V_p in terms of u. A complex harmonic excitation and response is substituted:

$$F(t) = F_0 e^{i\omega t}, \quad V_p(t) = V_{p0} e^{i\omega t}, \qquad u(t) = u_0 e^{i\omega t} \tag{2.17}$$

with F_0, V_{p0} and u_0 being complex amplitudes in the form of $a + ib$. Substituting these responses in the electrical domain and cancelling the exponential terms, V_{p0} is then written as:

$$V_{p0} = u_0 \frac{\theta\omega R\left(C_p\omega R + i\right)}{\left(C_p\omega R\right)^2 + 1} \tag{2.18}$$

The voltage is again substituted in the equation for the mechanical domain along with the assumption for the displacement function and is rewritten to group the real and imaginary terms:

$$-M\omega^2 + k_s + \frac{(\theta\omega R)^2 C_p}{\left(C_p\omega R\right)^2 + 1} + i\omega\left(c_s + \frac{\theta^2\omega R}{\left(C_p\omega R\right)^2 + 1}\right) = \frac{F_0}{u_0} \tag{2.19}$$

In this format it is easy to recognise the mass, stiffness and damping terms. Note that the real piezoelectric term is dependent on the frequency, so initially only 2 extremes for the resistance will be investigated, namely $R = 0$ and $R = \infty$. For the first, all coupling terms with θ vanish leaving us with the well-known second order equation for a mass-spring system. The limit of R to infinity is taken for the open circuit equation. The damping term vanishes and the stiffness term reduces to θ^2/C_p. The short and open circuit conditions yield the following natural frequencies:

$$\omega_{n,sc} = \sqrt{\frac{k_s}{M}}, \qquad \omega_{n,oc} = \sqrt{\frac{k_s + \frac{\theta^2}{C_p}}{M}} \tag{2.20}$$

Note that the subscript *sc* is often omitted, in which case the short circuit resonance frequency is implied. The effect of piezoelectric coupling on dynamic systems becomes clear from these two equations. The change in stiffness found earlier also leads to a shift in the natural frequency of a 1D system. This also implies that a change in all natural frequencies can be expected for continuous systems. For this 1D system, the open circuit natural frequency is normalised with the closed circuit (purely mechanical domain related) frequency using k_{33}^2:

$$\frac{\omega_{n,oc}}{\omega_{n,sc}} = \sqrt{1 + k_e^2} \tag{2.21}$$

In equation 2.16b however, R is used as a variable. Its influence as it varies between 0 and infinity is investigated next. First, to make the conclusions more general the following substitutions are made [56]:

$$\omega_n = \sqrt{\frac{k_s}{M}}, \quad \zeta = \frac{c_s}{2M\omega_n}, \quad \Omega = \frac{\omega}{\omega_n}, \quad r = C_p\omega_n R \tag{2.22}$$

which represent the short circuit natural frequency, the dimensionless damping ratio, the normalized excitation frequency and normalized resistance. This yields a normalized equation of motion:

$$\left(1 - \Omega^2 + \frac{k_e^2 r^2\Omega^2}{(r\Omega)^2 + 1}\right) + i\Omega\left(2\zeta + \frac{k_e^2 r}{(r\Omega)^2 + 1}\right) = \frac{F_0}{u_0} \tag{2.23}$$

First, only the real part is equated to zero to evaluate the undamped natural frequency. To this end a fourth order equation in Ω with only even powers must be solved. In figure 2.8 the result is given against $\log_{10}(r)$ and k_e^2. The maximum coupling coefficient used here is $k_e = 0.7$, which is currently approximately the highest value known for 33-mode ceramic operation. From it, the conclusions can be drawn that for increasing coupling the natural frequency increases only when the resistance differs at most an order of magnitude from $r = 1$. This is the normalized optimal resistance at short circuit resonance.

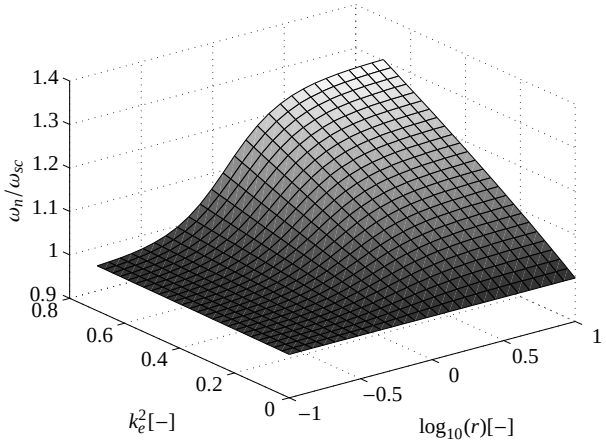

Figure 2.8: Open circuit to short circuit natural frequency ratio for various k_e^2 and r.

The second question is how the displacement, voltage and power develop for varying excitation frequency, and high or low coupling. By combining equations 2.18 and 2.19 the voltage is found as a function of the excitation, and to calculate the power the voltage is multiplied by the complex conjugate of the current, and integrated over time one cycle. However, specifically for a sinusoidal voltage signal, the average delivered power dissipated in a resistive load is the RMS of the voltage divided by the resistance. For the sinusoidal signal this yields $P = V_0\bar{V}_0/(2R)$. The overline indicates the complex conjugate of the respective variable. The following equations are found for the normalized displacement, normalized voltage and average normalized power:

$$u_0' = \frac{u_0}{F_0/k_s} = \frac{1}{\left(1-\Omega^2+\frac{k_e^2 r^2\Omega^2}{(r\Omega)^2+1}\right)+i\Omega\left(2\zeta+\frac{k_e^2 r}{(r\Omega)^2+1}\right)} \tag{2.24a}$$

$$V_0' = \frac{V_0}{F_0/\theta} = \frac{k_e^2 r\Omega\,(r\Omega+i)}{(r\Omega)^2+1}u_0' \tag{2.24b}$$

$$P_{avg}' = \frac{P_{avg}M\omega_{sc}}{F_0^2} = \frac{1}{k_e^2}\frac{\left|V_0'\right|^2}{2r} = \frac{r\Omega^2 k_e^2}{2\left((r\Omega)^2+1\right)}\left|u_0'\right|^2 \tag{2.24c}$$

For low coupling, the influence of the coupling on the mechanical domain is negligible. This implies two constraints: the harvested energy is only a fraction of that dissipated by all other forms of damping, and that the electromechanical coupling itself is low $k_e^2 < 0.01$ [56]. The requirement for the coupling is somewhat arbitrary as it simply means that there is no appreciable change in natural frequency. In figures 2.9 it shows that the mechanical behaviour is rather insensitive to the load resistance and shows a resonance peak at $\Omega = 1$. This is consistent with the low coupling presumption. Looking at the electrical domain the

influence of the resistance becomes clear. For low resistance ($r \ll 1$) no voltage is built up. For a high resistance ($r \gg 1$) a clear voltage peak at $\Omega = 1$ is shown, similar to the mechanical domain. Lastly, the power shows a single peak at $\Omega = 1$ and $r = 1$. This can be deduced by taking the derivative of the power function to r and Ω. This analysis is performed in [56] and shows that for the low coupled case the optimal resistance is:

$$r_{opt} = \frac{1}{\Omega} \quad R_{opt} = \frac{1}{C_p \omega} \tag{2.25}$$

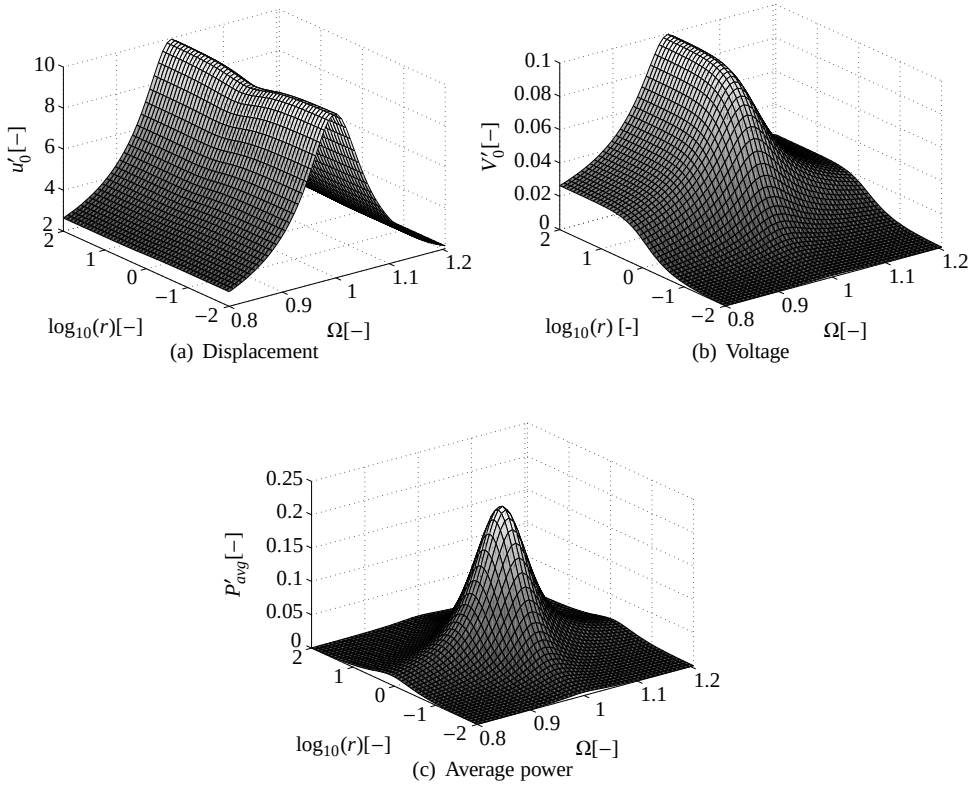

Figure 2.9: Normalised response plots for $k_e^2 = 0.01$ and $\zeta = 0.05$.

A critical solution step can be derived from this consideration of low coupled systems. Due to the negligible change in natural frequency and dynamic stiffness of the system, such systems can be solved sequentially. First, the mechanical domain can be solved in the traditional manner. One important consideration is that the viscous damping is always significantly higher than the power harvested. This requirement can be quantified as [56]: $k_e^2/\zeta \ll 1$. For fully undamped systems a small amount of harvested power will obviously greatly reduce the amplitude at resonance. The displacement which results from

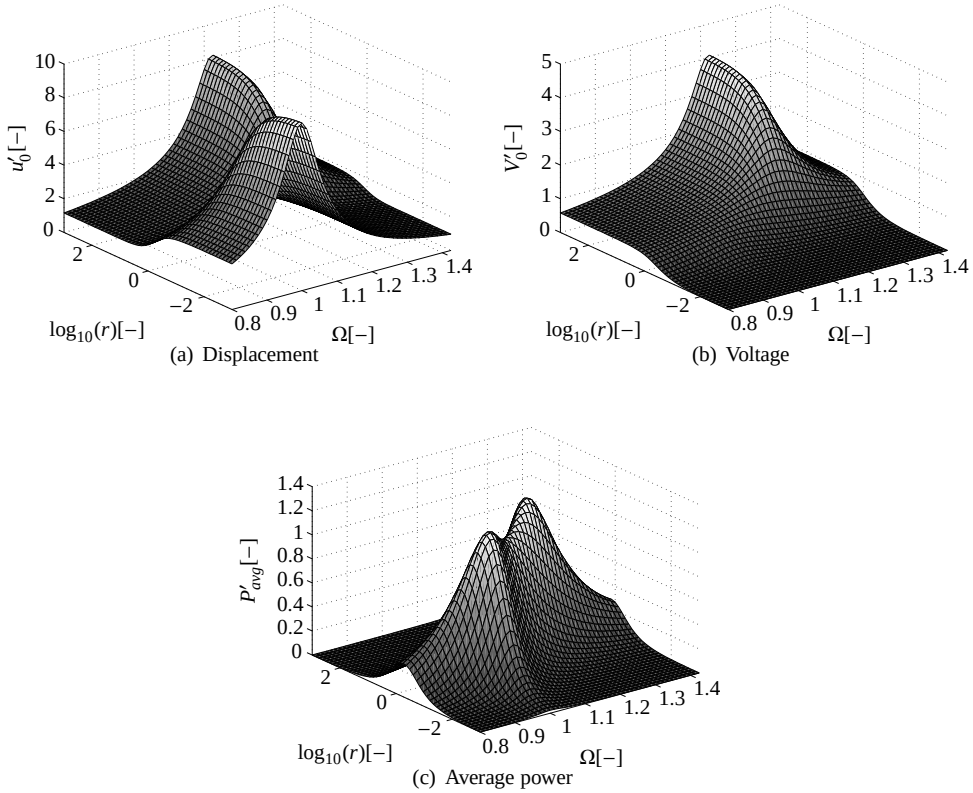

Figure 2.10: Normalised response plots for $k_e^2 = 0.5$ and $\zeta = 0.05$.

the mechanical analysis can then be plugged into the electrical domain to calculate the power (equation 2.24). The relevant equation for the mechanical domain is presented here for clarity:

$$u_0' = \frac{u_0}{F_0/k_s} = \frac{1}{1 - \Omega^2 + i2\Omega\zeta} \tag{2.26}$$

Second is the case of high coupling where $k_e^2 \gg 0.01$. The results are shown in figure 2.10. The displacement shows the purely mechanical response for $r \ll 1$, but as r approaches unity the coupling becomes significant. As r further increases beyond unity the amplitude and natural frequency shift noticeably. The voltage shows similar behaviour to the low coupling case but the peak is shifted towards the open circuit natural frequency. Both the peak voltage and power are significantly higher due to the high coupling. The power plot is most interesting as the single peak has now split into two. This is a characteristic of *impedance matching* circuits and the split is determined in [17] and addressed in detail in [20].

For the low coupling it is also relatively simple to calculate the maximum harvested power in the case of a harmonic excitation force. With the mechanical domain insensitive to the amount of induced electrical damping, the dimensionless harvested power is calculated by taking the derivative of the power equation to r, assuming u'_o constant. Equating to zero yields the optimal resistance $r = 1$. Inserting this into the power equation then yields:

$$P'_{max} = \frac{k_e^2 \Omega}{4} u_0'^2 \tag{2.27}$$

2.7 Conclusions

In this chapter the groundwork has been laid for a basic understanding of power harvesting. The consitutive equations for a piezoelectric element have been presented and discussed and relevant simplifications for ceramic materials have been included.

Coupling the theory to practice, the equations for real elements have been derived. This revealed a single parameter, the force coefficient, which determines the coupling of the piezoelectric element. Normalising this variable with the stiffness and capacitance yields the dimensionless electromechanical coupling. This is a critical value which is a measure for the mutual influence of the electrical domain on the mechanical domain. It is the driving factor behind the coupled behaviour of electromechanical systems.

Finally, the equations governing a 1 dimensional element directly coupled to a resistor – known as Alternating Current Impedance Matching (ACIM) – have been explored. Expanding on the implications of electromechanical coupling, first a low value situation was presented. In this case solution methods can be performed sequentially: first solving only the mechanical domain and then the electrical. For high coupling a coupled solution is necessary, greatly complicating the analysis. More importantly, as will be shown towards the end of the next chapter, these are all impossible to solve exactly, except for the ACIM circuit.

Chapter 3

Electronics basics and circuits

The field of electronics cannot be ignored when power harvesting is considered. Although it is possible to harvest power by simply attaching a resistor to the piezo element, as demonstrated in section 2.6, this power is not suitable for electronics. Moreover, in some cases power output can be increased significantly by utilisng advanced electronic circuits which manipulate the piezo voltage.

This chapter addresses the electronics knowledge needed to further understand power harvesting. First the familiar concepts of current and voltage will be addressed, followed by directly related phenomena such as charge, linear components, etc. It will be shown that, as far as linear electrical systems are concerned, there is little difference between mass-spring systems in the mechanical domain: both are governed by second order differential equations.

The discussion of selected semiconductor components is more difficult. These have no simple mechanical equivalent and will take place strictly on an electronic basis. Only the aspects which are relevant to the operation of the circuits are discussed.

The chapter concludes with a study of three electrical circuits. The Direct Current Impedance Matching is a passive circuit which only rectifies the power from the piezo element. Second is the active Synchronous Electric Charge Extraction circuit which is used in a numerical analysis of a rotor blade mounted harvester. Third is the Synchronized Switch Harvesting on Inductor circuit, which is studied most extensively of all throughout this research.

3.1 Fundamental concepts

In each and every domain, one can distinguish a ‘through’ and ‘across’ variable. In the mechanical domain these are the force and velocity of a body. *Voltage* is the driving force across an electrical load, generating a *current* through it [39].

Current is the flow of electrons (charge carriers). Physically the electrons, being negatively charged, flow from the negative to the positive side. However, in electrical engineering the convention is to consider the direction of flow from higher to lower voltage, which is more intuitive and has no consequences for calculations concerning circuitry. If current is equivalent to velocity, then the integral of current is the amount of accumulated

electrons, $Q = \int Idt$, known as *charge*, unit [C], coulomb. In piezoelectrics it is, in fact, a charge displacement which occurs within the material. Note the fundamental equation 2.1b where the electric displacement field is used. To calculate a current this must be multiplied with the electrode area giving the amount of charge and then derived to time: $I = DAdt$. The constitutive piezoelectric equation and the current equilibrium equation for a piezoelectric element are repeated here for reference.

$$\mathbf{D} = \mathbf{e}\boldsymbol{\varepsilon} + \boldsymbol{\epsilon}^{\varepsilon}\mathbf{E}_v \tag{3.1a}$$

$$I = \theta\dot{u} + C_p\dot{V} \tag{3.1b}$$

Two 'types' of current can be distinguished. First is *direct current* or DC. This implies a flow of electrons in only one direction. DC is typical of battery powered circuits and equipment. The analysis of DC circuits is much like finding a static solution to a mechanical problem. The other is *alternating current*, AC. Here current alternately flows in opposite directions. This is the case for electrical outlets, for example, and is characterized by an amplitude, frequency and phase. Analysing such circuits is similar to dynamic mechanical systems and involves differential equations.

Returning to piezoelectric material, the constitutive equations 2.1 imply that applying a static displacement will displace only a fixed amount of charge. To continuously generate power it must therefore be cycled regularly, resulting in AC power. This power must be conditioned for further use as electronic circuits and measuring systems require DC power. This is done through the use of some electronics that are discussed in the next two sections.

3.2 Basic equations

This section will describe the fundamental electronic components and equations. First the components are discussed and described mathematically. Then one combination of these components is presented which displays equivalence with a mass-spring system, in order to emphasize the mathematical similarity between both domains. A number of conclusions are drawn based on the developed equations.

In electronics two basic laws generally hold: the Kirchhoff circuit laws [57]. One is that the sum of all currents through a node in a circuit equals zero; this is a conservation law. Second is that the sum of all voltages around a closed network equals zero, representing equilibrium. This is demonstrated in figure 3.1. For the current this leads to $I_1 - I_2 - I_3 = 0$. Current towards the central node is positive. For the voltage a direction must be specified. The voltage law dictates that, when going clockwise around the network of figure 3.1(b), the voltage equation is $V(t) - V_1 + V_2 - V_3 = 0$.

The electrical and mechanical domain possess a number of similarities. A mechanical force on a damper results in a certain velocity. In the electric domain, Ohm's law [54] states that a voltage V in volts and the current I in amps across a resistor are linked by $V = IR$, with R being the *resistance* [V/A] or [Ω], Ohms. Compared with the mechanical domain this is analoguous to a viscous damper where force equals the damping multiplied by the velocity: $F = cv$.

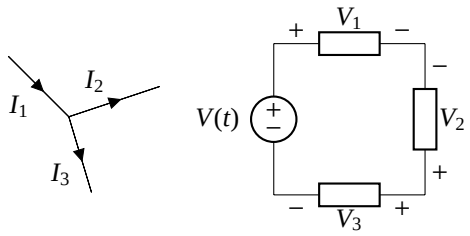

(a) Current law (b) Voltage law

Figure 3.1: Visualisation of the Kirchhoff current and voltage law.

There are two further equivalent components between these two domains. The first is the inductor L in Henries, [H]. The physical appearance of an inductance is that of a coil of wire. A linear inductor is governed by the following equation: $V = L\dot{I}$ [41]. This is equivalent to a mass in the mechanical domain: recall how Newton's second law [43] was initially formulated as $F = m\dot{v}$ which further clarifies the equivalence.

Last is the capacitance C in Farad [F]. This is governed by the equation $V = \int I\mathrm{d}t/C$. A capacitor is formed by two parallel plates separated by a non-conductive medium, or *dielectric*. The capacitor accumulates charge as the voltage across it increases. The mechanical equivalence is a compliance. The symbols for an inductor, resistor and capacitor are shown in figure 3.2.

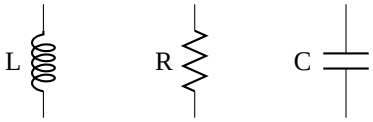

Figure 3.2: Symbols of an inductor, resistor, and capacitor.

This equivalence of the electrical and mechanical domains is summarised in table 3.1 and is known as the force-voltage equivalency, or the impedance analogue. The other method is the force-current equivalency, or mobility analogue, but the analogues with mechanical phenomena are not as straightforward.

Table 3.1: Equivalent parameters in the mechanical and electrical domain.

Electrical quantity	Mechanical equivalent
Voltage V	Force F
Current I	Velocity $\dot{u}$
Resistance R	Viscous damping c
Capacitance C	Compliance $1/K$
Inductance L	Mass M

Comparing a mass-spring system to a series RLC circuit will emphasise the similarity

between both domains. In an RLC circuit a resistor, inductor and capacitor are joined in series with a voltage source providing excitation, see figure 3.3. Applying the voltage law implies summing the 3 voltages using their respective equations and equating them to the source voltage. Because the components are connected in series, yielding a single closed network, the current law indicates that all components are passing the same current $I(t)$. The differential equations governing both systems are:

$$F = M\ddot{u} + c\dot{u} + ku \qquad V = L\dot{I} + RI + \frac{1}{C}\int Idt \tag{3.2}$$

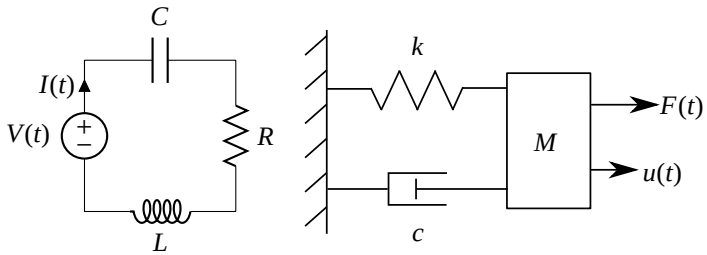

Figure 3.3: A voltage driven RLC circuit and a 1DOF mass-spring system.

Both equations are second order differential equations and can be solved analytically when a harmonic solution is assumed. In the mechanical domain this gives rise to a natural frequency which is calculated as $\omega_m = \sqrt{k/M}$. The same can be said for an electrical system. The associated natural frequency of the RLC circuit is $\omega_{el} = 1/\sqrt{CL}$.

Another case which will return a number of times is the RC circuit. Here a capacitor is charged through a resistor, or a charged capacitor discharges through a resistor. The circuit is shown in figure 3.4.

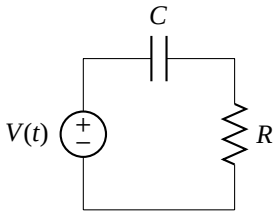

Figure 3.4: RC circuit layout.

The differential equation governing this circuit is:

$$C\dot{V}_c + \frac{V_c}{R} = V(t) \tag{3.3}$$

A step of the voltage source with amplitude V_0 is applied at $t = 0$ s. Solving this differential equation using an exponential function for V_c yields the following asymptotic response functions, left for charging ($V(t)$ from 0 to V_0 volts) and right for discharging ($V(t)$ from V_0 to 0 volts):

$$V_c(t) = V_0\left(1 - e^{-t/(RC)}\right), \qquad V_c(t) = V_0 e^{-t/(RC)} \tag{3.4}$$

The quantity RC is a measure for how quickly the capacitor responds to a voltage change. For example, when given a step input, at $t = RC$ the voltage has reached 63% of the applied voltage, or has decreased 63% when it is discharging. This quantity is used regularly in this thesis and is referred to as the *RC time* of an RC loop. In the remainder of this thesis, the subscripts will indicate which components are under consideration (e.g. in figure 3.10 it is written as RC_s).

With this knowledge it is possible to describe the electrical model of a piezo element. Since equation 2.8b is written as a balance of currents, the piezo material is considered a current source of which the generated current is $\theta\dot{u}$. The internal capacitance must also be accounted for by coupling a capacitance parallel to the current source. The resulting circuit diagram is shown in figure 3.5. Here one closed network is present between the current source and capacitance. A second one is implied between the capacitor and the open contacts on the right. Additional circuitry can only be connected to these contacts and not between the current source and the capacitance.

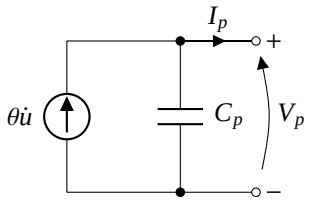

Figure 3.5: Electrical representation of a piezoelectric element.

The current I_p is the outgoing piezo current and is referred to as such throughout this thesis. Likewise, when V_p is used, it is the piezo voltage. To maintain compact equations the postfix (t) is often omitted as these values are implied to vary in time. Because the current I_p is shown here through the contacts of the piezo element, it is dependent on what is connected to it. Connecting a resistor results in $I_p = V_p/R$, similar to the AC calculation performed in section 2.6. Other components or an entire network of circuitry can also be connected in order to assist in optimizing the power output, complicating the equation for I_p. Active circuitry introduces switching behaviour which can no longer be analysed linearly. Therefore, these active components must be understood prior to introducing these more complex circuits.

3.3 Semiconductor components

To complete the study of electronics required for power harvesting a number of semiconductor components must also be introduced. These behave differently than the linear components

discussed previously, making analysis more difficult. These parts act as electronically controlled switches and are useful to control and switch currents and to rectify the power from AC to DC for use in measurement electronics.

For the DC impedance matching circuit (section 3.4) only diodes are necessary. For the SECE circuit (section 3.5) and the SSHI circuit (section 3.6) diodes are also required. Switches are necessary as well, therefore two types of transistors (the BJT and FET) are discussed.

3.3.1 Diodes and rectifiers

Diodes are components which only pass current in one direction. If the applied voltage bias coincides with the 'through' direction of the diode it allows a nearly unimpeded passage of current, save for a small drop in voltage V_d. This means the diode will only conduct when the voltage rises above V_d. This is a result of the working principle of diodes and is unavoidable. The voltage drop changes depending on the type and material of diodes, such as silicon (0.6 V), germanium (0.2-0.3 V) or Shottky type diodes (0.2 V).

When biased in the opposite direction the diode will block all current, effectively behaving as an infinitely large resistor. Below a certain negative voltage a normal diode will fail. Figure 3.6 shows the schematic symbol and the characteristic *IV* curve, assuming the Schockley diode equation [53]. In the symbol the diode only conducts current in the direction indicated from the positive to negative contact.

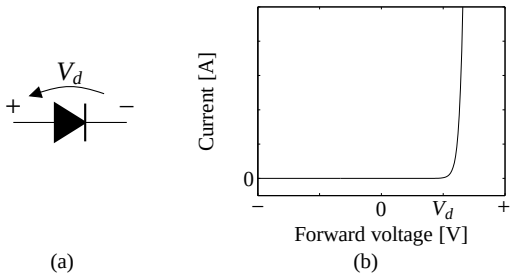

Figure 3.6: Diode symbol and typical *IV* curve.

A combination of diodes allows for transforming AC to DC. This arrangement, called a *full bridge rectifier*, along with a graph of the input and output voltage curves is shown symbolically in figure 3.7. Note that there are now 2 diode losses between the AC and DC signal: $V_{dc} = |V_{ac}| - 2V_d$. The rectifier rectifies the AC voltage, incurs a $2V_d$ voltage loss and cannot go below 0 V.

3.3.2 Bipolar junction transistor

For more advanced circuits, *bipolar junction transistors* (BJTs) are used to switch signals and amplify power. It is a 3-port with contacts called the collector C, emitter E and base B. There are also two different flavours of transistor: the *NPN*, and *PNP* version. Both need to

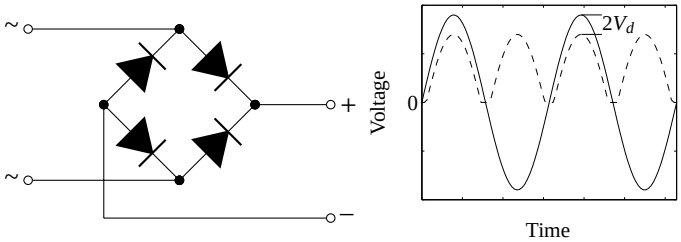

(a) AC contacts left, DC contacts right (b) V_{ac} (——) and V_{dc} (– – –)

Figure 3.7: A diode rectifier schematic (left) and typical voltage curve including diode losses (right).

be addressed to understand the operation of the advanced harvesting circuits. These types of switches are capable of using a small control current to pass a larger current. The ratio of these currents is denoted h_{FE} and is called the *common-emitter current gain*.

The difference between the types of BJT relates to the current direction. For an NPN type a small current is passed from the base to the emitter allowing a larger current to pass from the collector to the emitter. Aside from the current requirement a small voltage drop is incurred, similar to a diode. The first is the base-emitter drop V_{BE} and second the base-collector drop V_{BC}. The latter is not very relevant because there is typically no current from B to C. More important is the collector emitter voltage V_{CE}, since this is the main current. A simple diode model, as shown in figure 3.8 (a) and (b), is sufficient to understand the basic functioning of the NPN BJT [53].

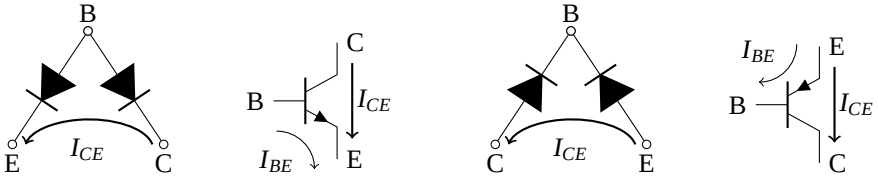

(a) NPN Diode model (b) NPN symbol and currents (c) PNP Diode model (d) PNP symbol and currents

Figure 3.8: NPN and PNP transistor models and symbols [53].

The NPN transistor possesses a number of operating regions: cut-off, active, saturation and reverse-active. The operating region depends on the values of V_{BE} and V_{CE}. A current I_{BE} allows a certain current to pass from the collector to the emitter. Any attempt to pass a higher collector emitter current I_{CE} will be met by a strong increase in the collector emitter voltage drop. The larger I_{BE}, the larger I_{CE} can be.

Cut-off is the region where the transistor behaves like an open switch, i.e. I_{BE} is so low that there is no current can pass between the collector and emitter. The active region is where $I_{CE} \approx h_{FE} I_{BE}$. Simply put, any attempt to increase I_{CE} beyond this ratio will be met with a strong increase in apparent resistance by the transistor. The saturation region is the one that is

of interest for the active harvesting circuits. Here $V_{BE} > V_{CE}$ and any current can pass from the collector to the emitter, up to $h_{FE}I_{BE}$. The collector emitter shows only a very minimal equivalent resistance. In this region the transistor behaves nearly as a short circuit, providing that the current is limited by other components in the circuit or h_{FE}, effectively going back to the active region. In the saturation region, the ratio of currents is then determined by the other components. The reverse-active region is where a current is going from the base to the collector. This region is irrelevant to this discussion and is rarely used at all.

The PNP type functions very similarly to the NPN version. The difference is in the direction of the currents. It requires a small emitter-base current to pass a large emitter-collector current. The currents are denoted the same as the NPN transistor but always have a negative value. In essence it steals a small amount of a main current, in order to allow the majority of the main current to pass unimpeded. The PNP version has the same operation regions: active, cut-off, saturation and reverse-active. The saturation region is the only one that is of interest for the operation of the active circuits. In this case $V_{BE} < V_{CE}$ and the ratio of currents is $I_{CE} \leqq h_{FE}I_{BE}$. The diode model and PNP symbol are given in figure 3.8 (c) and (d).

3.3.3 Field Effect Transistor

A *field effect transistor*, or FET, is another three port like the BJT. The main difference is that where a transistor is a switch which uses a current to control the switch, a FET uses a voltage to control the switching characteristics. A voltage field in the FET creates a conductive channel and the larger the voltage the larger the conductive channel. In a sense the channel acts like a variable resistor of which the resistance is controlled by the control voltage.

In essence the FET has four ports of which two are typically permanently connected, making a three-port. The drain (D), source (S), gate (G) and body (B). This is shown in figure 3.9, the body is not marked but is the centre where the arrow points towards, and it is connected to the source. The operating regions of the MOSFET are: off, sub-threshold, linear and saturation. The off region is where the gate-source voltage is insufficient and there is no channel from drain to source. The sub-threshold region is where there is insufficient V_{GS} which permits only a leakage current (nA to mA when approaching V_{GS}). The linear region is where the current and gate-source and drain-source voltage are linearly proportional, much like a controlled resistor. In the saturation region the maximum drain-source current is limited, an increase in drain-source voltage will not lead to a higher current. For use in the active circuits discussed in this thesis the linear region is of interest.

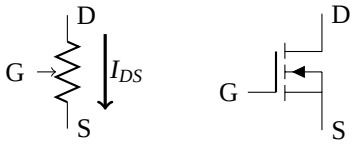

(a) Variable resistor model (b) MOSFET symbol

Figure 3.9: MOSFET variable resistor model and symbol.

There are many variants of the FET. These vary from the working principle ('depletion' and 'enhancement' mode) and polarity (positive or negative V_{GS}). Only one will be discussed here: the n-channel *MOSFET* (Metal-Oxide Semiconductor FET). In this version, a positive voltage from gate to source opens the channel between the drain and source, and the channel is completely blocked when $V_{GS} = 0$ V. The fully open conduction mode must be achieved as quickly as possible for efficient operation within the active circuits.

Using these semiconductors, the functioning of passive and active harvesting circuits can be discussed, which is the topic of the remainder of this chapter.

3.4 Direct Current Impedance Matching

The first circuit is the passive *Direct Current Impedance Matching* (DCIM) circuit. Appendix C gives a more detailed description of the circuit, operation, components, operating phases and the various waveforms. Here the main points are addressed, being the circuit operation, governing equations and the general performance.

3.4.1 Circuit design and operation

The circuit consists of a rectifier, storage capacitor C_s and load resistor R, as shown in figure 3.10. The AC signal from the piezo is rectified and the energy is stored in the capacitor C_s. It is chosen sufficiently large as to maintain a nearly constant DC voltage. In other words, the storage circuit has a comparatively high RC time relative to the cycle time of the piezo element. This is different from what is shown in figure 3.7 which shows the rectified voltage following the AC voltage. Here C_s is acting as a buffer, smoothing the voltage ripple after the recitifier.

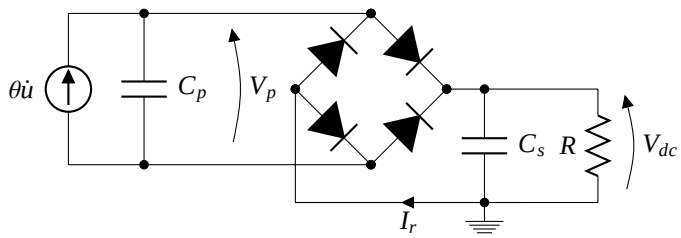

Figure 3.10: DC Impedance Matching circuit schematic.

Figure 3.11 provides an example of the voltage and current waveforms of the circuit at the optimal resistance. The applied displacement is shown (a), currents (b) and voltages (c). A sinusoidal displacement is applied, resulting in a sinusoidal current from the piezoelectric effect, but with 90 degrees phase difference.

There are two phases of operation: one is where the AC voltage signal of the piezo element alternates between $\pm V_0$. This can be seen in subfigure (c) where the piezo voltage alternates between the extrema but also in (b) where the rectifier current is zero. The other is when it conducts at near constant voltage when it has reached the threshold voltage of the

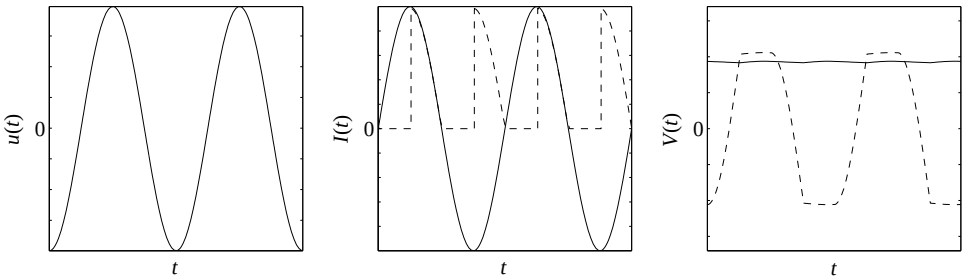

(a) Displacement input u (b) $\theta\dot{u}$ (——) and I_r (– – –) (c) V_{dc} (——) and V_p (– – –)

Figure 3.11: DCIM waveforms at the optimal resistance. Displacement (a), currents (b) and voltages (c).

rectifier. The threshold is determined by the DC voltage and the diode drop of the rectifier. In figure 3.11(b) the conductive phase is active when the rectifier current is non-zero and in (c) this is around the extrema of V_p. In (c) it can be seen that the DC voltage remains nearly constant due to the large capacitor C_s.

3

3.4.2 Governing equations

Due to the discontinuous conduction of the rectifier, an exact analytical solution is impossible. Another way to state it is that –under the assumption of a constant DC voltage– the transition from the non-conducting to the conducting recitifer implies an instantaneous change from open to short circuit operation. This in turn changes the apparent stiffness of piezo element within one cycle.

A detailed analysis of the circuit is given in [20, 56]. An approximate analytical solution is found by considering one half cycle, while assuming a sinusoidal motion and using an energy balance and current conservation approach. The main findings which are relevant to understanding the circuit are given here. Using the same non-dimensional parameters from equation 2.22 and neglecting the diode drop, the equations for displacement amplitude, voltage and harvested power are:

$$u_0' = \frac{u_0}{F_0/k_s} = \frac{1}{\left[\left(1-\Omega^2+\frac{k_e^2 r\Omega}{r\Omega+\pi/2}\right)^2+\Omega^2\left(2\zeta+\frac{2k_e^2 r}{(r\Omega+\pi/2)^2}\right)^2\right]^{\frac{1}{2}}} \tag{3.5a}$$

$$V_0' = \frac{V_0}{F_0/\theta} = \frac{r\Omega}{r\Omega+\pi/2}k_e^2 u_0' \tag{3.5b}$$

$$P_{avg}' = \frac{P_{avg}M\omega_{sc}}{F_0^2} = \frac{1}{k_e^2}\frac{V_0'^2}{r} = \frac{k_e^2\Omega^2 r}{(r\Omega+\pi/2)^2}u_0'^2 \tag{3.5c}$$

The calculation uses only the voltage and displacement at $t = 0$ s and $t = T/2$ s, with T being the period of excitation. The exact waveform of the voltage and displacement is not

expected to influence the power output for low coupled systems. Small deviations from a sinusoidal excitation should not strongly influence the output. This is investigated later in the thesis.

Recall the non-dimensional substitutions of equation 2.22. Mathematically these solutions differ only slightly from the ACIM results of equation 2.24. The difference is only a few values in two quotients. First is the denominator in the piezoelectric stiffness term of u_0' where 1 is replaced by $\pi/2$. The same holds for the denominator in the piezoelectric damping term. Consequently, processing this change throughout the calculation of the voltage and power leads to similar changes in both equations.

3.4.3 Low and high coupling

By evaluating the governing equations, plots for the normalised displacement, voltage and power can be generated as shown in figure 3.12. First is the low coupling case with identical coupling and damping parameters as the ACIM discussion of section 2.6. Restating from section 2.5, low coupling implies that the piezo material and electrical portion do not significantly influence the mechanical domain. When compared to figures 2.9 the differences are mostly subtle. This is due to the fact that, for closed and open circuit conditions, the results are identical since no power is harvested.

The most striking point is again the presence of an optimal load. It is similar to the ACIM case discussed in section 2.6, but with a different value for the normalised resistance r. For low coupling the dimensional and non-dimensional optimal electrical loads are:

$$R_{opt} = \frac{\pi}{2C_p\omega} \qquad r_{opt} = \frac{\pi}{2\Omega} \tag{3.6}$$

The difference is in the region which is useful for power harvesting, near the optimal resistance and the natural frequency ($\Omega = 1$), where the harvested power is maximised. The displacement shows no discernible difference. The voltage is also very similar but is marginally lower for all loads and frequencies. This has consequences for the power as well since the maximum normalised power is lower for the same excitation when compared to figure 2.9(c). The value for the optimal load is also different. The ACIM circuit maximises output at a normalised resistance of $r = 1$, and here the optimum is at $r = \pi/2$.

Second is the high coupling case, with the results shown in figure 3.13. The shift in natural frequency can be seen in the displacement plot. As the normalised resistance increases, the peak in the frequency Ω shifts from 1 to $\sqrt{1 + k_e^2}$. For the rest it appears very similar to the ACIM case. The voltage plot (b) shows a high value for open circuit resonance and the power (c) now shows two optimal points with equal magnitude. The optimal power is again lower than the ACIM case.

For high coupling the optimal resistance becomes more complex, and there are also numerous cases. The number of optimal loads and the magnitude thereof varies with coupling and damping. Optimal loads can be calculated, but this is overly complex and moreover superfluous to this discussion. These cases are not encountered in this thesis, although [20] provides an overview.

In [20] a rule of thumb is also given to determine whether or not a system is highly coupled. The ratio k_e^2/ζ and the coupling coefficient k_e^2 itself are used. When both are far

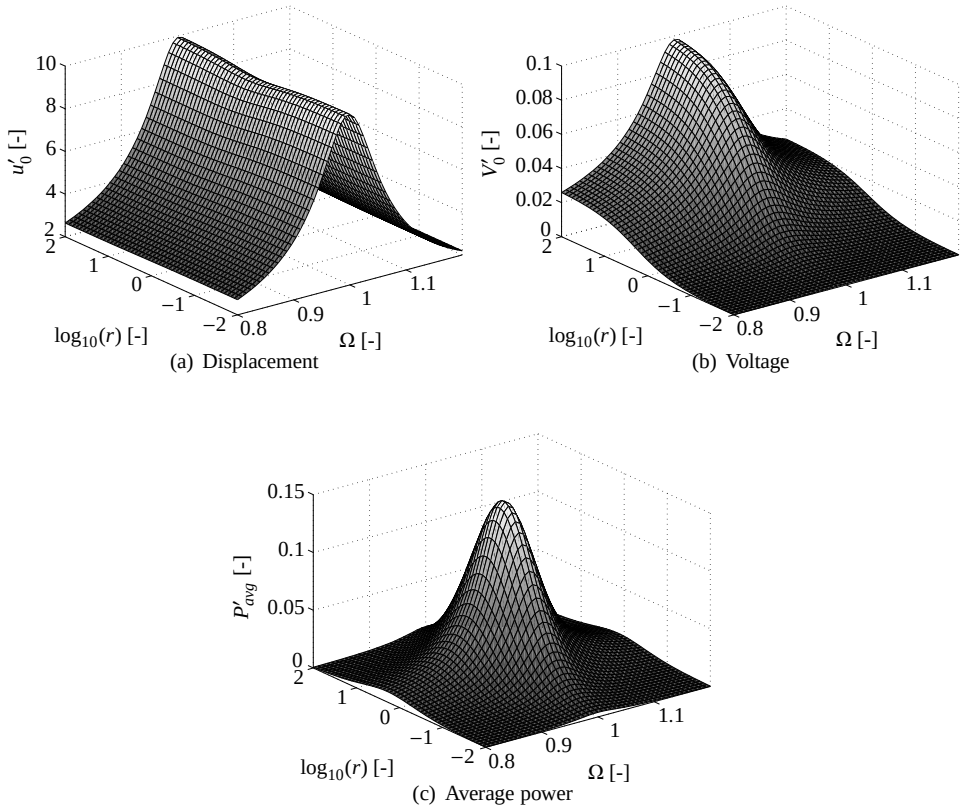

Figure 3.12: Normalised DCIM response plots for low coupling: $k_e^2 = 0.01$ and $\zeta = 0.05$.

smaller than unity, there is a negligible shift in natural frequency and most energy is still damped through mechanical effects rather than through power harvesting. Calculation of the optimal load is relatively straightforward as equation 3.6 is a valid approximation. When the first parameter increases beyond unity the two distinct optimum points arise. As k_e^2 increases these points separate more in optimal load and natural frequency.

3.4.4 Maximum harvested power

Lastly the maximum amount of power which can be harvested from a harmonic force excitation is of interest. As with the optimal resistance there are many cases. They cover a range of excitation frequencies, high and low coupling and short or open resonance conditions. For low coupling the maximum harvested power as a function of the normalised excitation frequency is:

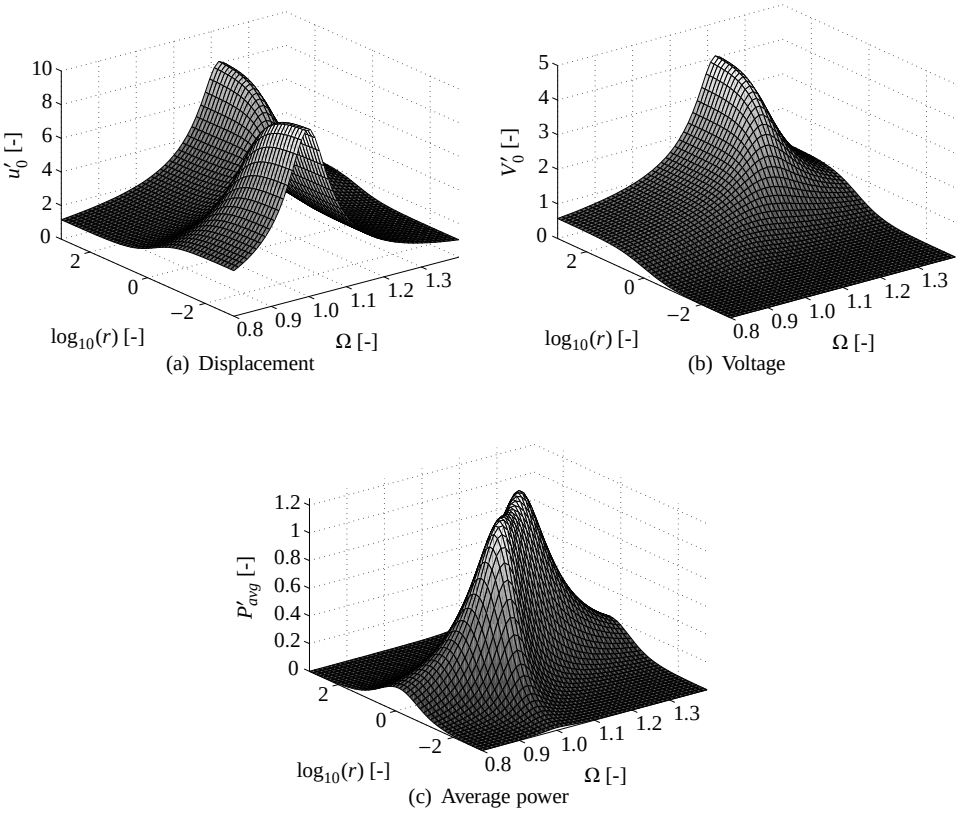

Figure 3.13: Normalised DCIM response plots for high coupling: $k_e^2 = 0.5$ and $\zeta = 0.05$.

$$P'_{opt} = \frac{k_e^2 \Omega u_0'^2}{2\pi} = \frac{k_e^2 \Omega}{2\pi \left(2\zeta\Omega + k_e^2/\pi\right)^2} \tag{3.7}$$

This shows that for low ratio of k_e^2/ζ, increasing the coupling will increase power. This can be understood in the sense that when coupling is insignificant the sequential solution of the equations of motion is justified. A relatively small increase in coupling will still not influence the global mechanical behaviour, yet more energy will be harvested per cycle.

For high coupling the maximum power, at the optimal resistive load and excitation frequency, is found to be [20]:

$$P'_{max} = \frac{1}{8 + 2\sqrt{16 + \pi^2}} \frac{1}{\zeta} \tag{3.8}$$

This value is identical for the short circuit and open circuit resonance peak. The output for the highly coupled situation shows that there is a limit to how much energy can be harvested from a given force excitation. Consider that, if the electromechanical coupling is too strong, the displacement will be supressed too much, limiting the energy input from the excitation.

3.5 Synchronous Electric Charge Extraction circuit

The *Synchronous Electric Charge Extraction* circuit (SECE) [17] is an active circuit for power harvesting. This circuit will be only discussed conceptually because it was not built during experimentation. An elaborate analytical discussion such as with the DCIM [20] and SSHI [22] is also not available.

It will be shown that this circuit possesses a certain analytical advantage because it has no optimal electrical load R and, when given a strain function in time, is very straightforward in terms of calculating the power output of a system undergoing more complex –but still cyclic– strain signals (chapter 4). More detailed information concerning the circuit is given in appendix D.

3.5.1 Circuit design and operation

The SECE circuit schematic is given in figure 3.14. In comparison with the DCIM circuit, a switch and coupled inductor is added. The dots indicate the positive contacts of the coils, here they indicate that the coils are connected in an opposing fashion. This is relevant to ensure that the generated current flows in the desired direction.

The main phase is the open phase in which the piezo element is in an open circuit condition. Only if the voltage is maximised does the circuit enter the next phase in which the switch closes, allowing the element to conduct through the rectifier and primary inductor winding. This is the primary discharge. When the current through the primary winding is maximised the voltage on the piezo element is zero. Next, the switch opens again and the secondary discharge phase starts. The coupled inductor then has a maximum magnetic field in the core. With the switch open the inductor must find an alternative to discharge its energy to, and does this by generating a current in the secondary winding. This secondary current passes through the diode, charging C_s. Again C_s is chosen sufficiently large as to maintain a nearly constant voltage. Upon completion of the primary discharge phase the piezo element again returns to the open phase and can begin charging.

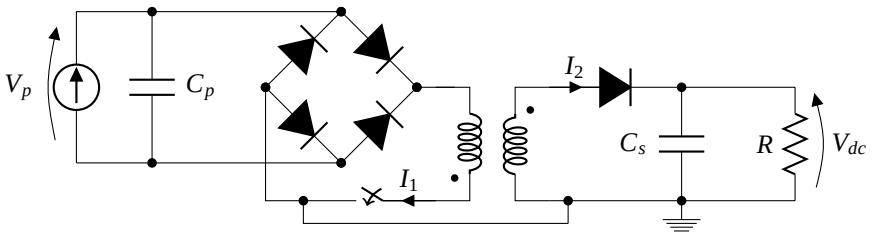

Figure 3.14: SECE circuit schematic.

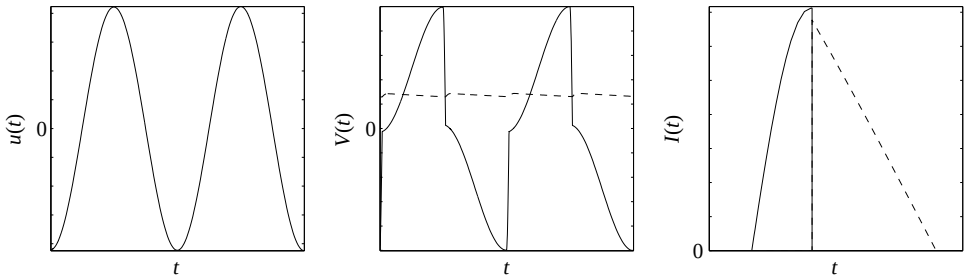

(a) Displacement (b) V_p (——) and V_{dc} (– – –) (c) I_1 (——) and I_2 (– – –)

Figure 3.15: SECE displacement input (a) voltage (b) and inductor current (c) waveforms.

3.5.2 Maximum harvested power

With the circuit operating mostly in open circuit mode, it is easy to calculate the power available for low coupled systems by using the equation of the energy stored in a capacitor:

$$E_c = \frac{1}{2} C_p V_{p,0}^2 \tag{3.9}$$

Assuming a harmonic displacement amplitude u_0, the maximum piezo voltage $V_{p,0}$ results from the open circuit equation of the piezoelectric equations 2.8 yielding:

$$V_{p,0} = \frac{2\theta u_0}{C_p} \tag{3.10}$$

With two discharge events per oscillation the maximum normalised power becomes [19]:

$$P'_{max} = \frac{2k_e^2 \Omega u_0'^2}{\pi} \tag{3.11}$$

This value is four times larger than equation 3.7, meaning the SECE circuit achieves four times higher effective coupling than the DCIM. For low coupled systems the value for the displacement amplitude can be inserted into this equation. For systems with high coupling the value for the maximum normalised power is [17]:

$$P'_{max} = \frac{1}{16\zeta} \tag{3.12}$$

This value is very similar to the result in equation 3.8, meaning that the maximum harvested power is nearly the same for both circuits.

3.5.3 Additional remarks

Note that equation 3.11 does not contain any details of the storage circuit (C_s or R): the displacement u_0 is linked only to the piezo voltage through the open circuit piezoelectrical

equations. Theoretically, the power harvested by this circuit is entirely independent of the storage circuit. In practice, the parameters of the storage circuit must be chosen such that current and voltage remain within the bounds of other components. The DC voltage follows from the choice of the load R: $V_{dc} = \sqrt{PR}$. Note that the coupled inductor transmission efficiency η_L is also not included but can be included simply by multiplying P_{avg} by it.

With the power being dependent only on the input strain, this circuit requires no optimisation with respect to the storage circuit electronics. This makes it very simple to calculate the power output of a low coupled system with a more complex strain history, where there is no dominant frequency. The choice of inductance values requires more work and is elaborated on in appendix D.

3.6 Synchronised Switch Harvesting on Inductor

The second active circuit is the *Synchronised Switch Harvesting on Inductor* (SSHI) circuit. The SSHI circuit functions very similarly to the DCIM circuit but differs in the fact that, where the DCIM circuit must change the piezo voltage through mechanical deformation of the patch, the SSHI circuit achieves this through electronic means.

3.6.1 Circuit design and operation

Switching the voltage of the piezoelectric element is achieved by a switched electrical oscillator. As mentioned in section 3.2 this requires a capacitor and inductor. Therefore a switched inductor is added on the AC side, in parallel with the piezo capacitance, as indicated in figure 3.16. This process boosts the piezo voltage, increasing power output.

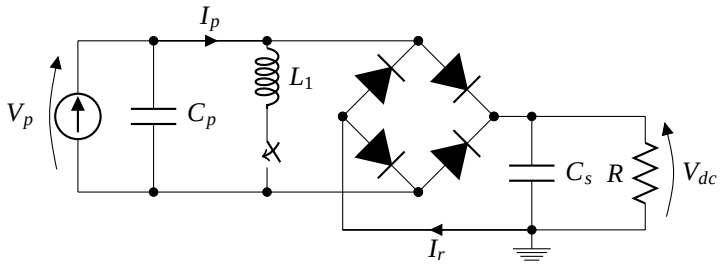

Figure 3.16: SSHI circuit schematic.

There are three phases to this circuit. Figure 3.17 shows the associated voltage and current waveforms. First is the conductive phase, similar to DCIM, where the rectifier passes current from the piezo to the storage circuit, and the piezo voltage remains nearly unchanged at a maximum value. When the piezo voltage V_p starts to drop the next phase begins. The switch detects the voltage drop and closes, connecting the inductor to the piezo element and creating an oscillator. The piezo voltage transitions from positive to negative or vice versa at a frequency of ω_{el}. It is stopped after only half a cycle due to the switch opening again. The switching phase duration is determined by the choice of the inductor through $t_{inv} = \pi\sqrt{C_p L_1}$.

It must be of relatively short duration compared to the mechanical excitation period. The switching phase is represented by the brief current spikes and swift voltage changes in figures 3.17 (b) and (c). In the next phase the piezo element operates in open circuit mode. The voltage will be lower than before the inversion due to the finite resistance of the RLC loop, due to the intrinsic resistance R_L of the coil. The piezo element must recover this voltage loss after which the opposite conductive phase begins.

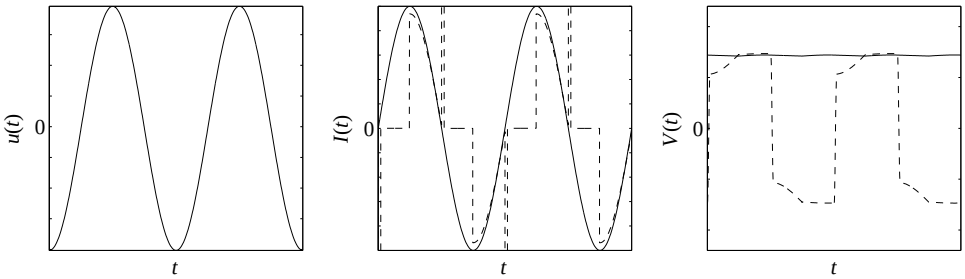

(a) Displacement (b) $\theta\dot{u}$ (——) and I_p (– – –) (c) V_{dc} (——) and V_p (– – –)

Figure 3.17: SSHI waveforms at R_{opt} for a given displacement (a), current (b) and voltage (c).

In the current plot the spikes from voltage inversion extend far beyond the limits of the plot. The sinusoidal portions occur during the conductive phase. The conduction current is similar in form to those of the DCIM circuit (figure 3.11). Compared to the DCIM circuit for a mechanically identical setup, either less time is lost alternating V_p between $\pm V_{dc}$, or a higher DC voltage can be achieved at a lower resistance. Both situations increase output over the standard DCIM method.

3.6.2 Governing equations

Similar to the DCIM circuit, an exact analytical solution is impossible. Not only is the rectifier non-linear but now the switching action of the circuit further complicates the solution. The required circuitry for the switch itself is too complex to solve analytically. However, ignoring the inner workings of the switch, a method similar to solving the DCIM circuit is applicable provided that terms concerning the voltage inversion are included as well. The solution is presented in [22] and again considers an energy balance, current balance and a half cycle of the motion.

The addition of the inductor L_1 requires some attention. As shown in section 3.2 an electrical oscillator has a natural frequency $\omega_{el} = 1/\sqrt{C_p L_1}$. The finite resistance of the coil induces damping and leads to an exponential decay of the peak amplitude during oscillation, just as viscous damping in a mechanical system. In the mechanical domain the damping value ζ is used. In the electrical domain the convention is the quality factor Q_i, where a higher value indicates less damping[1]. Assuming a constant coil resistance R_L, the voltage after inversion

[1] In the mechanical domain the damping ζ can also be related to a quality factor by $Q = 1/(2\zeta)$ [58].

V^- can be expressed as a function of the voltage prior to inversion. The quality factor and final voltage are:

$$Q_i = \omega_{el} L_1 / R_L \tag{3.13a}$$

$$V^- = -V^+ e^{-\pi/(2Q_i)} \tag{3.13b}$$

Again, the normalised displacement, voltage and power equations are presented here [22]. The exponential term of 3.13b is substituted with a more compact notation to improve legibility.

$$q_I = e^{-\pi/(2Q_i)} \tag{3.14a}$$

$$u_0' = \frac{u_0}{F_0/k_s} = \frac{1}{\left[\left(1 - \Omega^2 + \frac{\frac{1-q_I}{2} k_e^2 r\Omega}{\frac{1-q_I}{2} r\Omega + \pi/2}\right)^2 + \Omega^2 \left(2\zeta + \frac{2\left[1+\frac{r\Omega}{2\pi}\left(1-q_I^2\right)\right]k_e^2 r}{\left(\frac{1-q_I}{2} r\Omega + \pi/2\right)^2}\right)^2\right]^{\frac{1}{2}}} \tag{3.14b}$$

$$V_0' = \frac{V_0}{F_0/\theta} = \frac{r\Omega}{\frac{1-q_I}{2} r\Omega + \pi/2} k_e^2 u_0' \tag{3.14c}$$

$$P_{avg}' = \frac{P_{avg} M \omega_{sc}}{F_0^2} = \frac{1}{k_e^2} \frac{V_0'^2}{r} = \frac{k_e^2 \Omega^2 r}{\left(\frac{1-q_I}{2} r\Omega + \pi/2\right)^2} u_0'^2 \tag{3.14d}$$

The damping and stiffness terms are more complex when compared to the ACIM and DCIM equations (2.24 and 3.5), but the changes remain within the electromechanical damping and stiffness terms. The inclusion of the inductor variables makes it more difficult to explore the performance of the circuit and is beyond the scope of this study. In [22] an infinite quality inductor is assumed for simplicity in the qualitative description. The infinite inductor quality essentially makes the harvester highly coupled, regardless of how little piezo material is used. The following is then found for the dimensionless optimal resistance in the case of low coupling and an infinite quality factor:

$$r_{opt} = \frac{\pi^2 \zeta}{4 k_e^2} \tag{3.15a}$$

3.6.3 Low and high coupling

Equations 3.14 can be used to plot the normalised displacement, voltage and power. The results are calculated with an inductor quality $Q_i = 10$. The low coupling case is given in figure 3.18. The most striking difference for the displacement is the apparent absence of an open circuit resonance peak at $r \gg 1$ in the displacement plot. There is a maximum, but for the ACIM and DCIM circuits it is of nearly equal magnitude as the closed circuit resonance. When considering the functioning of the circuit the reason is easy to discover: although no

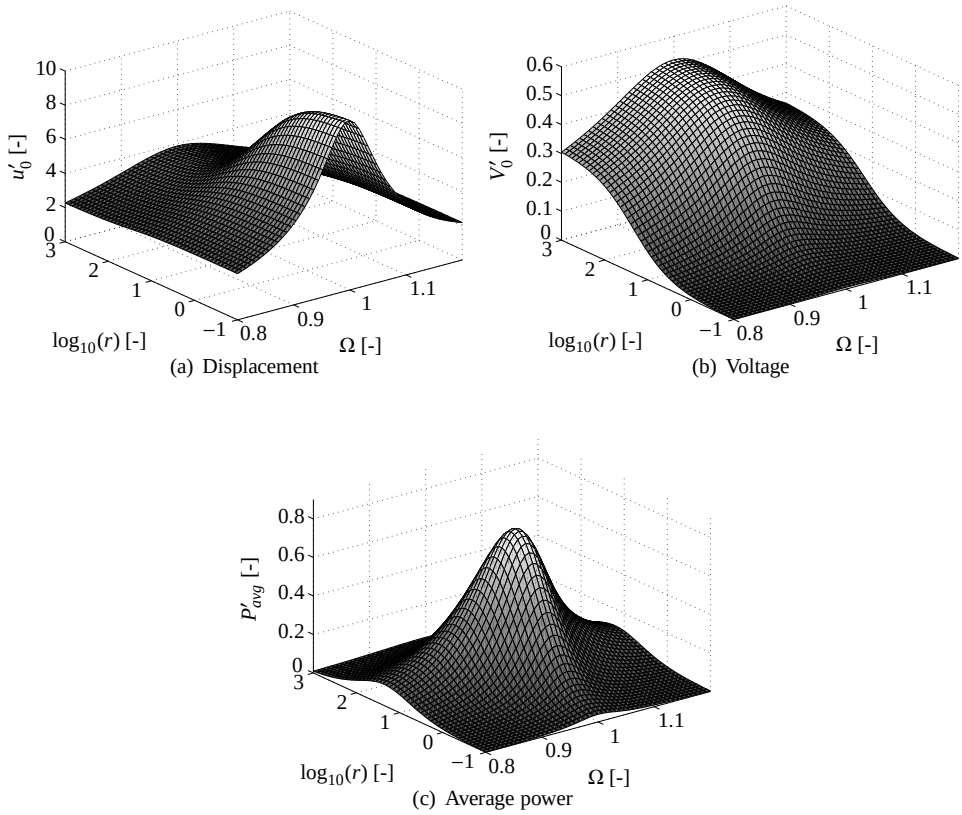

Figure 3.18: Normalised SSHI response plots for low coupling: $k_e^2 = 0.01$ and $\zeta = 0.05$.

power is harvested, the circuit dissipates the energy internally in the form of resistive losses in the inductor, supressing the motion of the mechanical domain.

The voltage plot shows a five-fold increase in open circuit voltage. Here a smooth maximum is visible as well as with the displacement. Despite the moderate displacement magnitude, it is the switching circuit that boosts the voltage to the value attained here, emphasising the advantage of the SSHI circuit. Due to the finite inductor quality, most of the energy extracted from the piezo element is lost during voltage inversion when a resistance $r \gg 1$ is used. Combined with very high load resistance (recall the logarithmic r scale) only a minimal amount of energy is harvested.

The power plot lastly shows one optimal operating point, at short circuit resonance. Its location is in resonable agreement with the optimal resistance calculated from 3.15, which was determined assuming an infinite Q_i. As Q_i increases towards infinity this agreement improves. The power output is also significantly higher than for the low coupled DCIM case of figure 3.12. The second optimum power point vanishes due to the action of the circuit.

As previously mentioned, efficient inversion will quickly lead to a high coupled system. The optimal resistance for a truly low coupled system can be calculated in the case of a finite inductor quality and is [18]:

$$r_{opt} = \frac{\pi}{\Omega\left(1 - e^{-\pi/(2Q_i)}\right)} \quad R_{opt} = \frac{\pi}{C_p\left(1 - e^{-\pi/(2Q_i)}\right)} \tag{3.16}$$

Second is the high coupling case, with the results in figure 3.19. The high coupling case shows tremendous damping for all $r \gg 1$, implying that nearly all energy is lost in the voltage inversion. Also, the voltage amplitude is quite small compared to the open circuit DCIM case. This is due to the lack of an open circuit resonance.

Interesting is the absence of a second power optimum, when compared to DCIM. This can be accounted for by considering that for the DCIM case, the optimum with the lower resistance shows a high current, and the high resistance optimum shows a high voltage. The latter implies more losses for the SSHI circuit due to the switching. The open circuit resonance peak involves high voltage, which suffers losses during inversion. The associated losses are so significant that this second peak vanishes completely.

3.6.4 Maximum harvested power

For low coupling the optimal resistance is inserted in equation 3.14 without substituting the displacement. The maximum power for low coupled systems is then:

$$P'_{max} = \frac{k_e^2 \Omega u_0'^2}{(1 - q_I)\pi} \tag{3.17}$$

Compare this to the DCIM low coupled power equation 3.7. For an inductor quality Q_i of 10, the SSHI circuit achieves nearly seven times higher power output for the same displacement input. When looking at the maximum power for varying Ω, the SSHI circuit harvests much more power than, for example, DCIM when excited at a non-resonant frequency. This is consistent with the conclusion of [19] that the SSHI circuit, when operated in a displacement driven fashion, provides a significant increase in output over other circuits.

In [22] it is stated that an advanced circuit increases the *effective coupling*. Equation 2.15 is the coupling which results from the mechanical design of the harvester, the effective coupling can be many times higher. The effective coupling of the SSHI circuit is as follows:

$$\bar{k}_e^2 = \frac{2}{1 - q_I} k_e^2 \tag{3.18}$$

Because $0 < q_I < 1$, this shows that even a poorly performing SSHI circuit improves the output over the passive DCIM under displacement driven conditions. In the case of a harvester which is only minimally coupled and which utilises a high quality inductor, the effective coupling may become so great that the system as a whole can be said to be highly coupled.

In [22] only a value for the maximum power is given for an infinite quality factor. With the previous equation in mind this means that even a mechanically low coupled system is then effectively highly coupled. For a force driven system the maximum normalised power at the optimal load and the optimal frequency is:

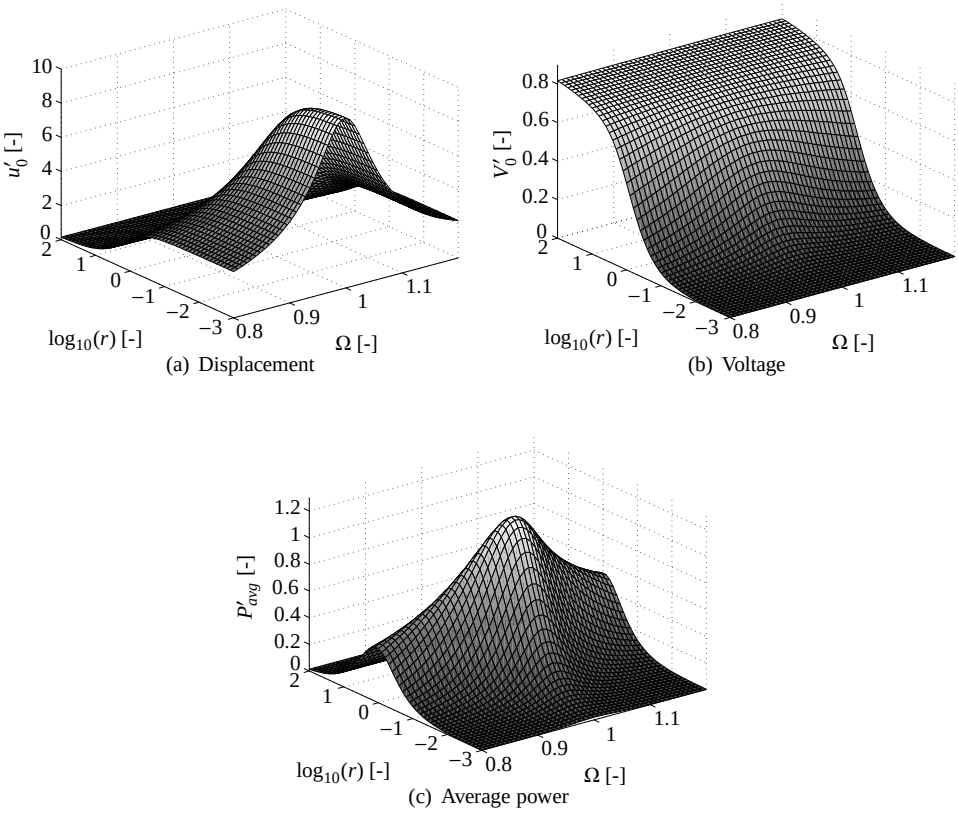

Figure 3.19: Normalised response plots for $k_e^2 = 0.5$ and $\zeta = 0.05$.

$$P'_{max} = \frac{1}{16\zeta} \tag{3.19}$$

This value bears close resemblance to the maximum power for a high coupled DCIM circuit (equation 3.8), the difference being 12%.

3.6.5 Closing remarks

A few last remarks concerning the SSHI circuit. This circuit is active, it requires a small amount of power to function. This power must be drawn from the piezoelectric element. Therefore, this circuit only functions well if it is designed correctly. This also implies that this circuit is not always applicable: some applications may be too small to be able to provide the energy needed to run the active circuit. In resonant cases this means that the power stated in equation 3.19 cannot be achieved as some power is lost to the circuitry. The lower limit to using this circuit is in the order of magnitude of milliwatts.

Also, the switching action of the circuit may induce vibrations in the mechanical system. This aspect is irrelevant for systems driven at resonance but may induce oscillations when the system is driven below resonance and the coupling is sufficiently high. This will be demonstrated in sections 5.2 and 6.5.

3.7 Discussion and conclusions

In this chapter some basic electronics have been discussed. This knowledge is essential in developing a good power harvesting system because it helps to boost the power output and utilise the material more efficiently.

Although only three circuits are discussed, it is sufficient to demonstrate some basic points. First is the subdivision between passive and active circuits. Passive circuits contain no electronics which manipulate the power flow via switching. Active circuits do do this and are designed to optimise the flow of power from the piezo element. Depending on the operating principle, different values of effective coupling can be achieved over the intrinsic electromechanical coupling of the harvester.

Depending on the type of excitation the various circuits each have their merits. When a system is force-driven at resonance, each circuit generates roughly the same maximum power, equations 3.8, 3.12 and 3.19. This is a matter of an energy balance between force input and harvested output as the mass and stiffness terms cancel out: attemping to harvest too much energy will supress the displacement so much that less power is put in to the system by the excitation. The coupling parameter is a powerful parameter in this evaluation.

One word of caution is that the derivation of the DCIM power (eqn. 3.8) is done using fewer assumptions than the SECE [17] and SSHI [22] equations. See [20] for the DCIM analysis. Earlier papers [17] discussing the DCIM circuit state the same maximum normalised power of $1/(16\zeta)$. It may be that a more detailed analysis of the SECE and SSHI circuits may reveal the same, revised, power maximum.

Since the maximum potential harvested power is known from the outset, it is wise to consider whether active circuits are the best choice for resonant systems. Their intrinsic power consumption reduces the maximum achievable output. If the coupling is sufficiently high through material use alone, active circuits have no benefit in resonant systems. If the intrinsic coupling of the system is relatively low, the active circuits can boost the effective coupling and consequently the resulting power.

For non-resonant conditions on the other hand, the active circuits present a remarkable increase in performance. This is demonstrated through equations 3.7 for DCIM, equation 3.11 for SECE and equation 3.17 for SSHI. These can be either force-driven at a frequency far below resonance, or displacement driven at any frequency. Here the effective coupling of the active circuits greatly reduces the amount of material necessary, or increases the output up to tenfold over DCIM for the same volume of material when the SSHI circuit is designed properly [19].

Figure 3.20 visualises the performance advantage of the active circuits for a displacement driven or low coupled system. It is a combination of the force and voltage curves of each circuit. The enclosed area is a measure for the harvested power. The diagonal lines are all parallel, reflecting the open circuit force-voltage relation.

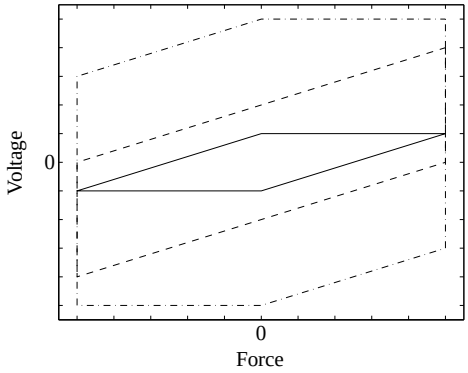

Figure 3.20: Force - voltage paths for the DCIM (——), SECE (– – –) and SSHI (– · – ·) circuits.

The discussion in this chapter is on a fundamental level. Depending on the application, more issues may arise and this is especially true for the SSHI circuit. These will be addressed where necessary in the following chapters.

Chapter 4

A helicopter rotor blade augmented with piezoelectric patches

The work presented in this chapter is part of the GRC project and is summarised in [59]. The main work is part of an internal GRC study [60].

4.1 Introduction

Currently, the technical lifespan of helicopter rotor blades is based on a very conservative lifetime calculation. After reaching this amount of flight hours, they are discarded. Blades may be produced with an intended life of around ten thousand hours [5], but are sometimes already replaced after only three thousand flight hours [6] based on a lifetime calculation. The calculation assumes an absolute worst-case usage scenario as failure of a rotor is unacceptable. This results in blades being discarded while they are still capable of numerous flight hours. Health monitoring systems within the blade can help to determine the lifespan of the blades more accurately. However, this requires electrical power for these systems.

Currently, electrical devices in helicopter rotors generally only consist of de-icing systems powered from the body of the aircraft via slip rings. Slip rings are maintenance intensive and sensitive to damage. Small rotorcraft may not have any electrical systems in the rotor, and due to the potential for a less stringent maintenance schedule for privately owned craft, the possibility of blade failure is larger. Structural health monitoring in the blades and methods of powering these systems are investigated within the European Clean Sky - Green Rotorcraft (GRC) project. Power harvesting in the rotor is considered as a method to power the health monitoring systems, negating the need for additional chassis-rotor electrical interfaces.

This chapter discusses one concept for powering in-blade equipment using power harvesting as a means to provide energy. Rotor blades are flexible components and exhibit large strain variations. Affixing piezoelectric patches to the blades will generate energy from these oscillations.

A few basics of helicopter dynamics must be discussed to provide sufficient background information. The rotor of a helicopter consists of a number of components, shown in figure 4.1. Major structural components are the rotor hub, swashplate (for blade pitch control)

and the blades. To allow for control of the craft, the control setting from the body of the helicopter is transmitted through the non-rotating swashplate to the rotating swashplate. This then transmits the control to the blades through pitch links to the individual blades. In this way the blade pitch can be changed once per revolution in a sinusoidal fashion. The blades are hinged on the rotor and are free to rotate in the vertical and horizontal direction. Because of this freedom two types of vibration modes arise. First is the *lead/lag* motion which is an oscillation in the plane of the rotor. It leads or lags the rotation of the hub. Flapping is a vertical motion of the blade, out of the rotor plane. The hinges which allow for this motion are therefore called the lagging and flapping hinge.

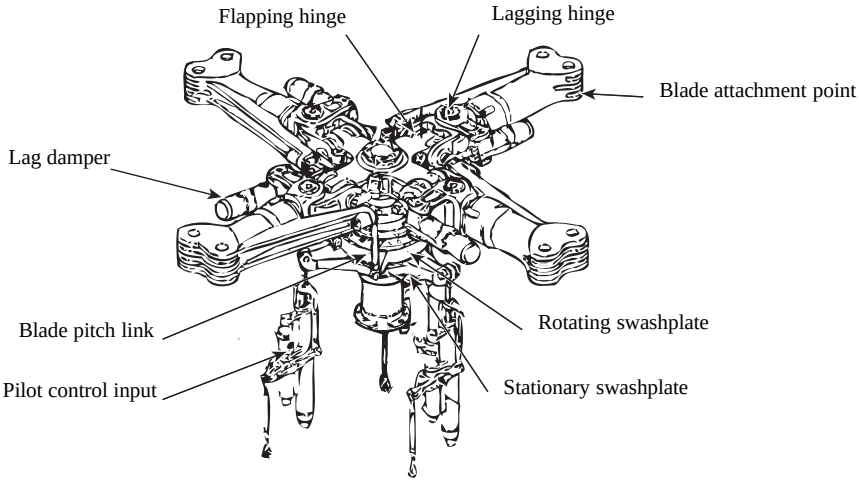

Figure 4.1: Drawing of a rotor hub and major parts.

During forward flight a phenomenon called dissymmetry of lift arises. This results from the fact that blades moving forward relative to the rotorcraft see a higher relative airspeed compared to those moving backward. To ensure that the net lift is roughly above the centre of gravity (CG) of the aircraft, the forward moving blades have a lower effective angle of attack than the backward moving blades. This lower angle of attack as achieved by changing the blade pitch, and is also a result of the flapping motion. The upward flapping motion occurs on the advancing side, reducing the effective angle of attack. Along with a variation in lift, this dissymmetry of lift also leads to a once per revolution variation in drag as well. The velocity distribution over the blade is shown schematically in figure 4.2.

A simple example of a linearly calculated lift distribution is shown in figure 4.3. Here, blade flexibility and flapping and lagging motions are neglected as well as the complex aerodynamics resulting from blade to blade interaction. It is calculated using the lift and drag tables for a blade profile from the GRC project [61] and a forward flight velocity of 130 knots (66.9 m/s). The lift per metre of blade span [62] and relative velocity are calculated as follows:

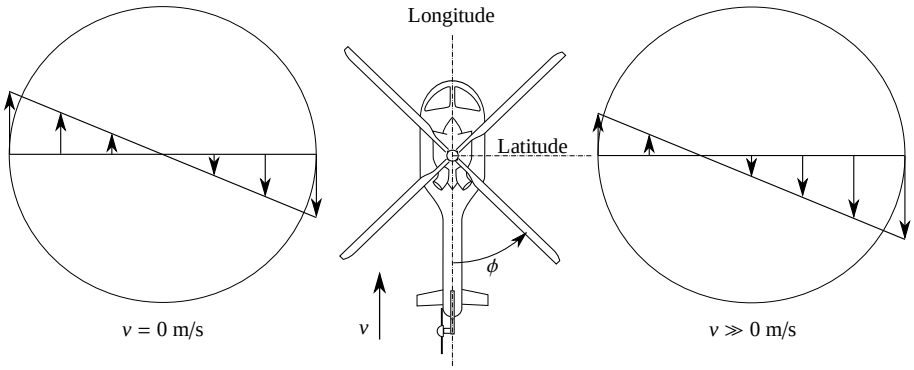

Figure 4.2: Helicopter nomenclature and the blade relative airspeed v_{rel} distribution for hovering (left) and forward flight (right). ϕ is the azimuthal angle relative to the tail of the rotorcraft.

$$L' = \frac{1}{2} c_l c \rho v_{rel}^2 \tag{4.1a}$$

$$v_{rel} = v \sin\phi + \Omega_R r R \tag{4.1b}$$

where L' is the lift per metre, c_l the lift coefficient , c the chord length (leading edge to trailing edge distance), ρ the density of the medium, ϕ the azimuthal angle (see figure 4.2), r the normalised spanwise position and R the rotor blade radius. [1]

The blade pitch that is used in the calculation is the result of a numerical simulation from AW, the same data used in section 4.3. Although the net moment about the centre of the blade disc is not exactly zero due to the simplified approach, it is sufficient to demonstrate the large variation in lift around the disc during forward flight. A similar picture holds for the drag forces which are approximately one order of magnitude lower and also unevenly distributed.

As will be explained in the next section, the large variation in forces leads to strong vibrations in the rotor blade. By affixing piezoelectric patches to the blade the patch deforms along with the blade, recovering energy in the form of electricity. This concept is developed and discussed in the remainder of this chapter.

4.2 Blade dynamics

In [61] mass and stiffness data is given for a rotor blade with a radius of R =8.15 m. These data and relevant natural frequencies are also listed in appendix F. Further blade dynamic data concerning forward flight was provided by Agusta Westland from which the deformed shape can be calculated as a function of the azimuth angle. A global impression of the blade and rotor properties is given in table 4.1.

[1] Typically R and r are used for the (normalised) electrical resistance. Due to convention and the lack of any potential conflict in this work, they are used here for the (normalised) rotor radius.

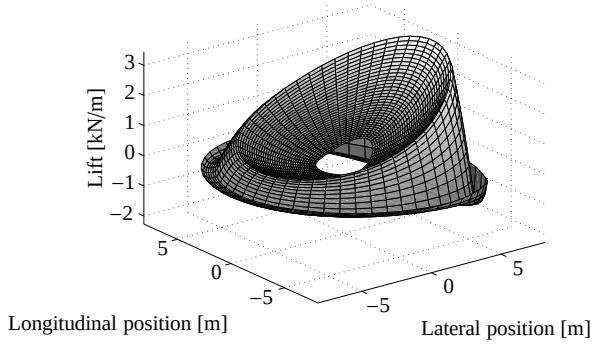

Figure 4.3: Lift distribution per metre blade span for 130kts forward flight. Blade root pitch setting: $\alpha = .1874 - .091\sin(\phi) - .1332\cos(\phi)$.

Table 4.1: General blade properties.

Property	Symbol	Value	Unit
Disc radius	R	8.15	m
Aerofoil section from/to		$(0.2 \ldots 1.0)R$	-
Chord length	c	0.65	m
Mass	m_{blade}	186.6	kg
Moment of inertia	J_{blade}	2812	kgm^2
Rotor frequency	Ω_R	26.26	rad/s

Using the mass and stiffness data the natural frequencies and mode shapes $\Phi_i(r)$ of the blade are determined with ANSYS. A modal analysis, including geometric stiffening due to the blade rotation, is performed. The resulting frequencies are listed in table 4.2, along with the normalised frequency (using Ω_R). The first flap and lag modes are rigid motions involving blade rotation around the hinge, and are a result of the rotor speed Ω_R.

Figure 4.4 gives the relevant nomenclature for the global and blade axes, which is taken from [61]. The x-axis is along the blade. The radial coordinate is written as rR. In the global system, flapping can be considered as an oscillatory motion in the xz plane, and lead/lag is a motion in the xy plane. Positive rotor rotation is from x to y and the nominal angle (without lead/lag) of the blade relative to the tail is the azimuth angle ϕ, see figure 4.2.

Moving to the local $\eta\zeta$ coordinate system, this one is aligned to the geometry of the airfoil. It makes an angle τ with the yz axes of the global coordinate system. The η axis intersects the leading and trailing edge of the aerofoil. The ζ axis is perpendicular to the η axis and passes through the quarter chord point of the aerofoil, i.e.: the leading edge is at $\eta = 0.25c$ and the trailing edge at $\eta = -0.75c$. This point is chosen because it coincides with the aerodynamic centre of the aerofoil, and also the neutral axis of the mass and stiffness properties. This only does not hold for the blade tip but, as will be shown in the results, no material will be placed here. Angle τ is the rotation of the $\eta\zeta$ axis relative to the xy system. It is the sum of

Table 4.2: Blade natural frequencies and normalised natural frequencies for $\Omega_R = 26.26$ rad/s.

Mode	Frequency	Ω
Lag 1	7.76	0.3
Flap 1	27.37	1.04
Flap 2	70.44	2.68
Lag 2	119.6	4.56
Flap 3	140.4	5.35
Torsion 1	153.0	5.82
Flap 4	253.5	9.65
Lag 3	313.1	11.9

the geometrical twist of the blade at the relevant span-wise position (appendix F), the pitch setting at the root, and any torsional deformation along the blade.

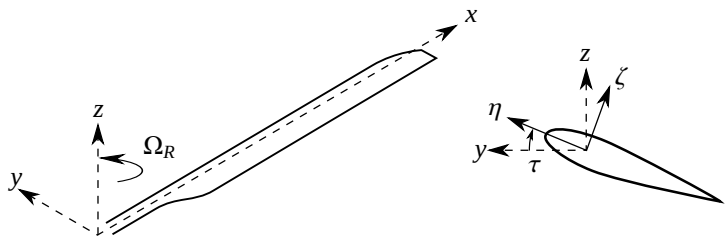

Figure 4.4: Global and local (blade) axes definition.

The dynamic data provided by Agusta Westland concerns the complete blade motion during one revolution, resulting from a simulation including flexible blade dynamics and aerodynamics. It is given in the form of coefficients $a_{n,i}$ and $b_{n,i}$ of a Fourier series $f_i(t)$, describing the blade tip displacement of each mode shape i. This data describes the motion of the blade tip for each of the vibrations and $a_{0,i}$ indicates how much each mode shape contributes to the overall motion. The blade shape is reconstructed through modal superposition. Consider the general form of a Fourier series [63]:

$$f_i(t) = \frac{a_{0,i}}{2} \sum_n \left[a_{n,i} \cos(n_i t) + b_{n,i} \sin(n_i t) \right] \tag{4.2}$$

If $\Phi_i(r)$ are the mode shapes then the shape of the blade is given by scaling the mode shape with the respective Fourier series divided by the tip response for that mode shape. The deformed shape of the blade $u(r,t)$ is then found by summing the scaled mode shapes:

$$u(r,t) = \sum_i \left(\Phi_i(r) \frac{f_i(t)}{\Phi_i(R)} \right) \tag{4.3}$$

This calculation is then performed for a number of steps of t to $2\pi/\Omega_R$, completing one revolution of the blade.

From linear beam theory, the curvature is the derivative of the angular displacement to the longitudinal coordinate: $\kappa = d\theta/dx$. Due to the blade twist and torsional response of the blade during flight, the global strain and curvature resulting from the Fourier series must be transformed to the local coordinate system aligned with the aerofoil geometry. This is done using the root pitch setting $\alpha(t)$, the geometrical twist of the blade $\tau_G(r)$ and the torsional response $\theta_x(r,t)$ of the blade. For each span-wise position r and time a transformation matrix $\mathbf{T}(r,t)$ is generated with which the curvatures $\left[\kappa_y, \kappa_z\right]$ are converted to the local coordinate system:

$$\mathbf{T}(r,t) = \begin{bmatrix} \cos\left(\alpha(t) + \tau_G(r) + \theta_z(r,t)\right) & \sin\left(\alpha(t) + \tau_G(r) + \theta_z(r,t)\right) \\ -\sin\left(\alpha(t) + \tau_G(r) + \theta_z(r,t)\right) & \cos\left(\alpha(t) + \tau_G(r) + \theta_z(r,t)\right) \end{bmatrix} \tag{4.4a}$$

$$\kappa_T(r,t) = \mathbf{T}\kappa(r,t) \tag{4.4b}$$

Using only the curvature and the transformation matrix a new curvature $\kappa_T(r,t)$ is calculated. This is then used to calculate the strain in radial direction (ε_{11}) around the circumference of the aerofoil. The latter is written in coordinates $\eta(s)$ and $\zeta(s)$, both as a function of the curvilinear coordinate s around the circumference of the aerofoil shape (see figure 4.6).

$$\varepsilon(r,t,s) = \kappa_{T,\eta}(r,t)\zeta(s) + \kappa_{T,\zeta}(r,t)\eta(s) \tag{4.5}$$

With this the mechanical domain and in particular the blade strains have been tackled. In the following sections the analysis of the rotor blade harvester patches will be continued and concluded with a discussion.

4.3 SECE output of the rotor blade

The SECE circuit described in section 3.5 is used to estimate the power output of the piezoelectric patches in the blade. It is chosen over the impedance matching circuits because the SECE circuit requires no optimisation of the electrical load. Determining the strain history of each patch is sufficient to calculate the SECE output. A number of steps are taken to calculate the output of each patch. First, the global deformation of the neutral axis of the blade and the axial strain around the circumference of the blade is approximated. Second, an assumption of the stress state of the patch must be made. These two are then combined to determine an output.

4.3.1 Mechanical and electrical constraints

A number of constraints are taken into consideration in the calculation of the power output of the blade. The first relates to the mechanical strain that a patch is submitted to. For ceramic material the maximum strain value is typically in the order of 10^{-3} , this value is chosen as the limit. Ceramic materials cope well under compression but cannot handle any appreciable tensile strains. Therefore, in this calculation only the minimum-to-maximum

strain is compared to the material strain limit. In reality this implies applying the piezoelectric patches under maximum compressive prestress during manufacture because ceramic cannot handle tension. Although applying patches under prestress is difficult from a manufacturing standpoint, patch elements are available which possess some level of prestress. In the conceptual phase this is an acceptable choice.

The second constraint concerns the power output of each patch. Of the patches that remain within the strain criterion, only those that develop enough specific energy (J/m^3) are allowed. This will yield only those locations that are comparatively efficient.

The final constraint relates to aerodynamic properties of the rotor blade. Rotorcraft are designed such that in case of engine failure the main rotor will autorotate. This means the rotor will rotate simply due to the airflow through it, given a minimal forward velocity [64]. The imposed rotor rotation is sufficent to allow for a relatively safe unpowered landing and is vital for helicopter safety. Autorotation requires certain dynamic requirements from the blade, and one in particular relates to the CG along the η axis of figure 4.4. The CG must be positioned forward of the aerodynamic centre to ensure favourable blade dynamics with respect to autorotation. As the aerodynamic centre is typically located at $c/4$, patches behind $c/2$ are not allowed. This value is chosen because a patch at $c/2$ can be balanced by one located at the leading edge. However, two results will be presented, one with this requirement, and one without.

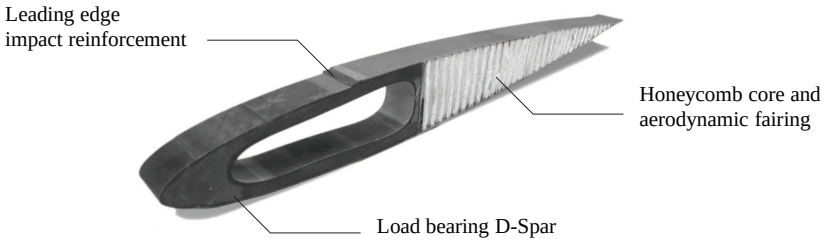

Figure 4.5: Section of a NACA0012 rotor blade [65].

4.3.2 Deformation of the neutral axis and axial strains

The blade surface is subdivided into a mesh with radial and surface coordinates *r* and *s*, as in figure 4.6. Coordinate *s* is zero at the leading edge, follows the upper surface to the trailing edge (s=0.67 m) and along the bottom surface back to the leading edge (s=1.32 m).

In radial direction there are p elements and in surface direction q elements. Figure 4.7 shows two examples of the strain for one patch i, j for one revolution, resulting from equation 4.5. The patches show only positive strain due to the centrifugal loads on the blade. Strain extrema are marked.

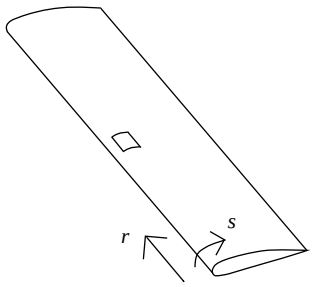

Figure 4.6: Definition of radial and surface coordinates r and s.

4.3.3 Strain approximations

Determining the entire strain vector $\boldsymbol{\varepsilon}$ on the patch is a complex task and is strongly dependent on the substrate material. Calculating the strain requires the complete blade design, from geometry to full elasticity matrices. Within the GRC project blade definition [61] the blade is considered to be made up of composite material. This further complicates the investigation as the properties can be tailored to meet specific requirements, even locally. These are not defined, making the possibilities nearly endless. Only the bulk blade properties are given in the baseline definition.

Therefore, in order to generate an approximation of the output, assumptions must be made concerning the stress/strain state of the patch. Confirmation of the assumptions is only possible with the aforementioned complete blade design, however, sound judgement can provide reasonable assumptions. The following discussion is in terms of the element axes (figure 2.6), assuming the 1 axis being parallel to the blade axis, and the 3 axis perpendicular to the surface of the blade. A 1D state can be used assuming $\varepsilon(r, s, t) = \varepsilon_{11}$ as the input for the patch. This will overestimate the output as the stresses along the 2 and 3 axis will be constrained to zero. This is clearly an incorrect assumption as the blade and piezo element will have a three-dimensional stress state with shear terms.

The stress along the 3 axis of the patch can be considered zero due to the patch being affixed to the profile: the opposite surface is always free. Second is the influence of shear stresses, which introduce variations in the tensile stresses. In [66] it is stated that strain variations along the 3-axis do not influence the developed voltage, provided that the strain used in the piezoelectric equation is taken at mid-thickness of the patch. Also, with the piezoelectric coupling coefficients e_{12} being zero, insensitivity of the charge generation of the material due to the other shear terms is implied. Combined with the lack of shear-extension coupling terms in the stiffness matrices of piezo ceramics this effect can be ignored.

Last is the transverse stress σ_{22}. This is strongly dependent on the relative difference in Poisson ratio ν [67] of the piezoelectric and composite materials. For thin-walled beams this stress is zero but this assumption may not hold for the blade which is comparatively thick-walled, particularly toward the leading edge (see figure 4.5). The transverse stress σ_{22} is simply taken to be zero.

The remaining strain components are calculated from the radial strain using the g formulation (appendix A) of the piezoelectric equations, rewritten to acquire $\boldsymbol{\varepsilon}$ as a function

of the single input strain ε_{11}. In the g formulation the elasticity terms are of the open circuit condition, negating the need for explicit calculation of the voltage field. For the strain $\boldsymbol{\varepsilon}$ this yields:

$$\boldsymbol{\varepsilon} = \frac{\varepsilon_{11}}{S^D_{11}} \mathbf{S}^D_{m,1} \tag{4.6}$$

The strain state is then inserted into the e formulation of the piezoelectric equations and rewritten to acquire the voltage field $\mathbf{E}_v$:

$$\mathbf{E}_v = -\boldsymbol{\beta}^{\varepsilon} \mathbf{e} \boldsymbol{\varepsilon} \tag{4.7}$$

The voltage field can then be used to calculate the energy of a single discharge of a patch using the energy content of a capacitor. This is done in a later step.

4.3.4 Calculation method for SECE output

With respect to how the total energy output is calculated, consider figure 4.7 again. Figure (a) is an example where an absolute maximum-minimum approach will yield the most energy. The 2 discharges near $t = 0$ s reduce the energy which can be recovered by a factor of 2 compared to the patch discharging only at the global minimum and maximum. The energy recovered by the extra discharge is negligible because of the minimal change in strain between the first two extrema. Considering the fact that the energy of one discharge depends on the square of the accumulated voltage (and therefore strain), it is advantageous to forego a large number of small discharges to achieve a few large ones. Figure 4.7(b), on the other hand, is an example where it is advantageous to discharge at each strain peak.

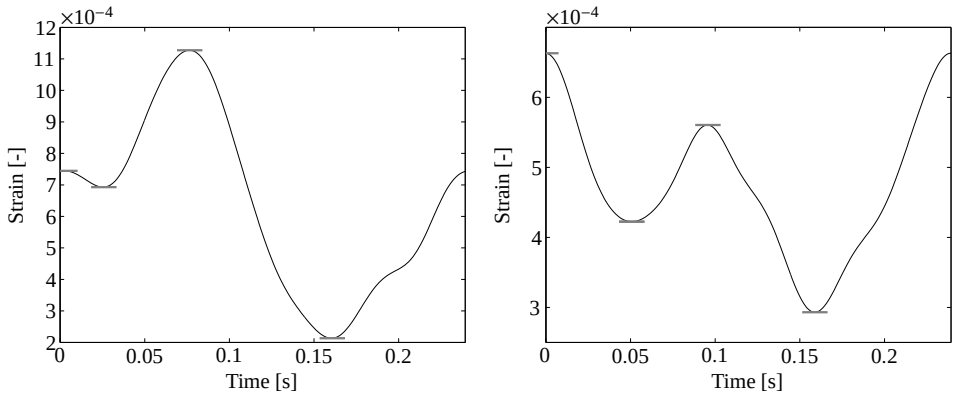

(a) More power using global extrema (b) More power using local extrema

Figure 4.7: The time history of the strain for one element in the blade. The horizontal bars emphasise an extreme value.

The following steps are then taken to calculate the power for all patches i, j and to select only the most efficient sections. Equations describing the actions of each step are given in appendix G.

1 Each directional change is detected by finding zero crossing events of the derivative of the strain. The strain at that point is stored yielding k values for ε_{peak}. For example, in figure 4.7, $k = 4$ for both cases.

2 The maximum to minimum strain variation is determined for each patch. If it is larger than the allowed material strain it is excluded from the remainder of the calculation. It yields the characteristic function $\chi^{\varepsilon}_{i,j}$ for each patch which is unity if the strain remains within bounds and zero if not.

3 The specific energy $U'_{i,j}$ generated by each patch during one revolution is calculated. This is done in two ways: by summing the energies of each discharge and by calculating the energy if the patch would only discharge at the absolute maximum and minimum strain. The higher value of the two is used.

4 The patch with the highest specific energy $\chi^{\varepsilon}_{i,j} U'_{i,j}$ is determined and denoted U'^{max}.

5 Only those patches which achieve at least a predefined minimal output η_p compared to the patch of the previous step are considered. This yields a narrower characteristic function $\chi^{\eta}_{i,j}$ which is unity if the patch meets the efficiency requirement and zero if not.

6 The total energy per revolution per patch $\chi^{\eta}_{i,j} U_{i,j}$ is calculated. The specific output is multiplied by the dimensions of each patch l, w and t.

7 Total power P is calculated by summing over i and j and dividing by the simulation time.

The end result is a single value for the power output of the rotor blade.

4.4 Power output and patch distribution

The results of the calculation method presented in the previous section are discussed here. First are the results concerning the deformations within the blade. Figure 4.8 shows the blade curvature in the local η and ζ directions. These are used as the basis for determining the strain at the circumference of the aerofoil.

Next, the maximum and minimum radial strain for each element is calculated. Figure 4.9 shows these results. The trailing edge clearly shows the largest strains which are significantly higher than the capability of ceramic material. Also notice the sharp drop in strain at $R \approx 7.4$ m, this is due to balance weights in the blade at that location.

Following determination of the strain data, the material data of the piezoelectric material is required. In this study two materials are used. One is a piezo ceramic from Physik Instrumente: PIC255. The second material is polyvinylidene fluoride, or PVDF. This is a piezo polymer which can be used in the areas, such as the majority of the trailing edge, where the strain variation is too large for the ceramic. Although it exhibits a far weaker piezoelectric coefficient, its larger strain capabilities make up for the loss when strains are in the percentage range. The relevant material properties are given in table 4.3.

Note that e_{31} is not given for PVDF as this information was not available from the manufacturer. The voltage is calculated using the g formulation of the piezoelectric equations

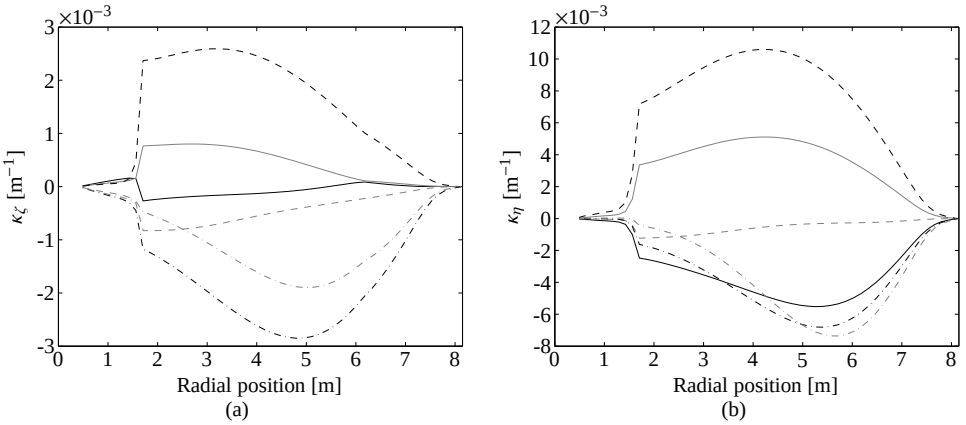

Figure 4.8: Blade curvature given in the local aerofoil coordinates at various azimuth angles, 0° (——), 60° (——), 120° (– – –), 180° (– – –), 240° (– – –), 300° (– · – ·).

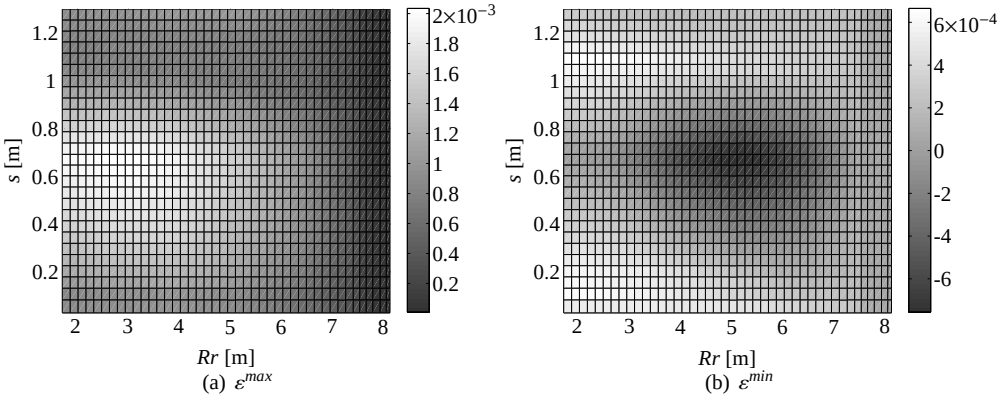

Figure 4.9: Absolute maximum and minimum strains over the blade during one revolution.

[52, 55]. Therefore the g_{31} parameter and the equation $V = g_{31}E\varepsilon t$ is employed. Further calculations remain the same.

Figure 4.10 shows the result of the sum of squared strain changes. This is indicative for the amount of energy available and where most energy can be harvested. The trailing edge shows the most potential and overall the upper surface ($0 < s < 0.67$ m) is more suitable than the bottom surface of the blade.

Last is the patch distribution across the blade, given in figure 4.11. It shows the ceramic location as well as PVDF. The PVDF is concentrated at the trailing edge where strains are the largest. The ceramic is located in a ring defined by the maximum strain variation. The

Table 4.3: Piezoelectric material properties for the in-blade concept.

Material property	Unit	PIC255	PVDF
Modulus of elasticity E	GPa	120	4
Piezoelectric coefficient e_{31}	N/Vm	-7.15	n.a.
Piezoelectric coefficient g_{31}	Vm/N	-0.013	0.26
Relative permittivity ϵ_r	-	1750	11.3
Layer thickness t_l	mm	0.5	0.5
Density ρ	kg/m^3	7800	1850

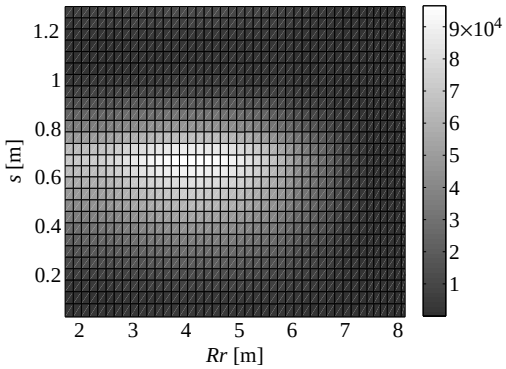

Figure 4.10: Energy density [J/(rev m^3)] over the blade.

efficiency η_p is chosen as 0.5 here.

Table 4.4 finally shows the output of this system. Not only is the power important, but being an aircraft the power to weight ratio is a critical factor. Clearly the PVDF is of no use in this application, the strains in the blade are not large enough to capitalise on the high strain capabilities of the material. Additionally, the significant output of the ceramic patches shows that only a very limited number of patches is required. The 'Full' column represents the performance when the autorotation requirements are not accounted for, and the 'Balanced' does consider this.

4.4.1 Stiffness modification

From the outset the presumption was made that the system coupling would be low. The validity of the presumption is assessed by recalculating the blade stiffness properties with the addition of the patches. The PVDF is not included in this evaluation due to the poor performance of the material. The stiffness is recalculated by using the tensile stiffness of the patch. For the radial value it is simply added to the original value. For the bending stiffness in η and ζ direction the radial stiffness of the patch is multiplied with the distance to the original neutral line of the blade.

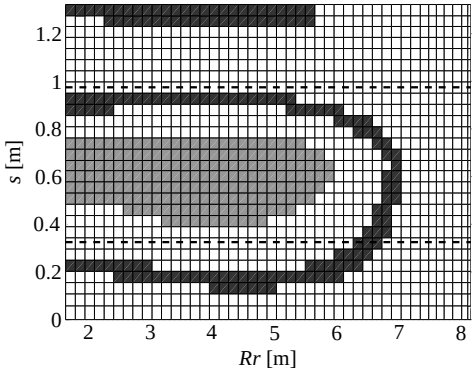

Figure 4.11: Piezoelectric material distribution within the blade. Optimal PIC255 (——) and PVDF (——) areas shown. Central band between (- - -) is forbidden due to blade balancing requirements.

Table 4.4: Result summary of the in-blade power harvesting concept.

	Unit	PIC255 Full	PIC255 Balanced	PVDF
Power	W	40.4	25.6	1.44
Number of patches		789	789	443
Efficient patches		161	104	190
Covered area	m^2	1.78	1.15	2.10
Weight	kg	6.96	4.5	1.94
Power / kg	W/kg	5.8	5.7	0.74

Figure 4.12 shows the relative change in stiffness for two cases. It is calculated as, for example:

$$\delta k_{rel} = \frac{EI_{\zeta}^{new} - EI_{\zeta}^{old}}{EI_{\zeta}^{old}} \tag{4.8}$$

Case (a) is without inclusion of the autorotation requirements, all patches that meet the efficiency requirement are used. Along the majority of the blade the change is below 10%. However, near $R = 7$ m the bending stiffness of the blade in ζ direction is more than doubled. Reviewing figure 4.5 this is not surprising. At that radius the patches are concentrated near the trailing edge. In the original blade, the D-spar provides structural strength. Patches located at the trailing edge have a lever more than three times the leading edge of the D-spar. Using the parallel axis theorem this creates significant leverage of the piezo element.

Figure 4.12(b) shows the relative change in stiffness of only those patches which are located ahead of the mid-chord position. By removing the patches towards the trailing edge the change is limited to approximately 10%.

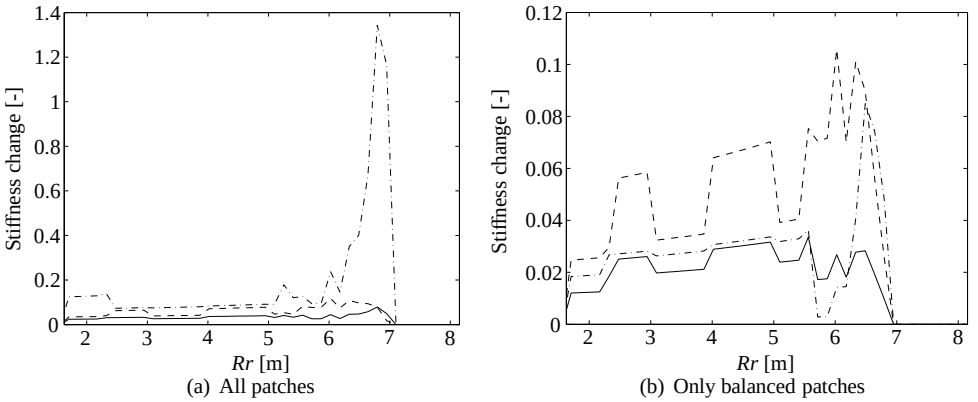

(a) All patches (b) Only balanced patches

Figure 4.12: Change in blade stiffness for EA (——), EI_η (– – –) and EI_ζ (– · – ·).

4.5 Discussion and conclusions

This section discusses a number of aspects concerning the results of this chapter. It is subdivided into three parts: one concerning the application of the in-blade power harvesting system, the second covers the calculation scheme in general and the last one discusses some practical implications of the resulting design.

4.5.1 In-blade harvester discussion

From a power perspective, the in-blade concept appears to be a viable option. Significant power levels can be attained with 10 W available for level flight with 1.4 kilograms of piezoelectric material when the patches are positioned correctly.

This power level will, however, decrease when other flight conditions are considered. Sharp manoeuvers such as banking, steep climbs, turning at speed, and so on will lead to different shaped strain plots such as figure 4.9. Including more flight conditions in the evaluation can only further limit the number of patches that do not exceed the maximum defined strain limitation.

A major drawback of the concept relates to the flight characteristics and dynamics of the rotor blade. First is the added outboard load and associated centrifugal forces. A number of patches are positioned at 7 m radius and the associated acceleration is in the range of 500g. This is a significant added load to an already critical component. One kilogram of material placed in this position increases the centrifugal blade root load by 1%.

From figure 4.11 it is clear that the trailing edge contains some useful zones for patch placement. These locations cannot be used due to the autorotation requirement. Patches placed at the trailing edge require additional balancing weights in order to restore the desired location of the CG. Additional balance weights further increase the total weight, decrease the power to weight performance of the harvesting concept and further increase blade loads. The ‘balanced’ column of table 4.4 is therefore the most realistic configuration.

Using the settings of this chapter also leads to a moderate change in blade stiffness, as demonstrated in figures 4.12. The calculated increase in stiffness of 10% may be sufficient to alter the blade properties in an unfavourable manner. However, this analysis is beyond the scope of this research.

The concept proposed in this chapter, with the calculated patch distribution, is not very suitable for application in rotorcraft. The added weight in the blades is significant and many restrictions apply. Assuming a very limited application of piezo material – implying a total power of at most a few watts – the concept and calculation method is still applicable. Compared to the output presented in this chapter, the power can be reduced by using thinner material and/or fewer locations.

4.5.2 Calculation method

The calculation method proposed in this chapter could be used for any slender beam undergoing cyclical deformation. Although coupling is not included in this case, it can be done by including an iterative loop. Provided that the external loading is known, this loop must recalculate the dynamics of the structure following a derived patch distribution. Using the revised dynamics the optimal distribution may be recalculated and the loop repeated. If not too fine a patch mesh is chosen it should quickly iterate to an optimal configuration.

An additional drawback is the absence of the full material matrices in this calculation. Here, it was assumed that the Poisson ratios of the blade and piezo material are similar and the material is free to expand and contract in the polarization direction. This allows for the use of the 1D piezoelectric equations. A significant difference between the Poission ratio of the materials under consideration will change the stress state of both materials and consequently the charge generated by the piezoelectric material. Also, considering the strong curvature of the blade around the leading edge, out-of-plane deformation will lead to additional internal stresses in the piezoelectric material located there.

4.5.3 Practical implications

The calculation showed that the majority of the patches function in a global peak-to-peak fashion, instead of discharging at every reversal of the strain direction. In [20] an analysis of the DCIM is done while taking only the global extrema of the strain into account. This implies that the DCIM circuit is relatively insensitive to the load path, as long as there is one dominant frequency with the associated strain peaks. The SECE circuit used in this chapter can therefore easily be replaced by an optimised DCIM circuit. Of course, this decreases the power output by approximately a factor of four, but output is not the only consideration. The added electronic infrastructure of the SECE circuit must also be taken into account.

With the phase and amplitude differences between the patches, it is impossible to use one circuit to control all patches in the blade. The SECE circuit requires a dedicated control circuit for each patch. This includes the envelope detector, rectifier, coupled inductor and diode in the DC portion of the circuit. Although typically each patch will also require its own optimised load, most patches only operate with two discharges per rotor revolution. By using patches of similar size, and therefore capacitance, a single storage capacitor and load

resistance could be used. For the DCIM circuit only the rectifier must be duplicated for each patch.

The increase in electrical infrastructure associated with SECE quickly becomes unmanageable when multiple patches are employed. Either the chosen patch size must be larger (decreasing the efficiency due to some charge cancellation [68]) or the number of patches must be limited, imposing a practical limitation on the size and output of this concept. Alternatively, the DCIM circuit can be used with larger patch coverage to achieve the same output.

Lastly, the issue of autorotation limits the output associated with this concept. As discussed, without this limitation many patches are placed toward the trailing edge of the blade. Due to the construction of the blade this also strongly influences the dynamic properties. When taking the autorotation into account, patches toward the trailing edge are not allowed. This greatly reduces the change in dynamic properties of the blade.

4.5.4 GRC decision

Within the GRC project, the in-blade concept is not pursued further. The decision is motivated predominantly by the autorotation properties and the added mass within the blade. The concept presented in the next chapter possesses much more favourable properties with respect to weight, location and output.

Chapter 5

The power harvesting lag damper

The content of this chapter is based on an internal GRC study [69] and was subsequently published as a paper in the Journal of Intelligent Material Structures and Systems [70]. The JIMSS paper resulted from a presentation at IWPMA 2011 [71].

5.1 Introduction

A second concept that is developed within the GRC project concerns the lag damper. As indicated in section 4.1, the blades are flexibly connected to the rotor hub so that they are free to move in flap and lag direction. The flapping modes are damped sufficiently due to the planform area of the blade (the surface area as seen from above) passing through the air, generating significant drag in the vertical direction. On the other hand, the lagging modes are minimally damped since only the frontal area of the blade is passing through the airflow. Excessive lagging motion can lead to unstable dynamic modes.

The unstable modes can be explained using figure 5.1, an exaggerated impression is given of a coupled mode shape between blades. Rotor frequency Ω_R, blade lead angle ξ and whirling frequency ω are shown. In certain cases the blades exhibit a lagging motion at the first natural lagging frequency. As the blades deviate from the equilibrium position, the global centre of gravity (CG) of the rotor system shifts away from the axis of rotation. Due to this, the CG also rotates around the rotor axis at frequency ω when viewed from the fixed reference frame of the rotorcraft chassis. This behaviour of the rotor CG is known as whirling [58]. In the fixed frame the CG rotates at frequency $\Omega_R - \omega$. The heading of the airframe is therefore of no importance and is not shown in the figure, as is the azimuth angle ϕ.

This excentricity generates such a tremendous excentric load that it is destructive to the aircraft. Consider a lagging amplitude of the GRC blade of 10 degrees, the CG of the blade then moves more than 0.5 m. These unstable dynamic modes are called air and ground resonance. The first occurs in the air and the second on the ground. The latter is the most dangerous and drives the lag damper design. Ground resonance is caused by coupling between the aircraft and the stiffness of the landing gear, and the displacement constraint imposed by the landing gear being in contact with the ground [72].

In order to suppress this lagging motion, a hydraulic or elastomeric damper is installed

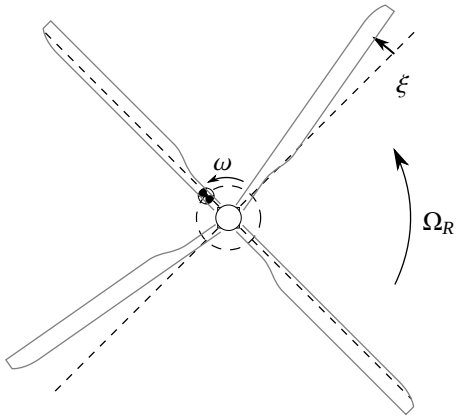

Figure 5.1: Exaggerated drawing of the rotor disc and composite centre of gravity during an unstable air or ground resonance mode.

on each blade. This damper can be connected between the rotor hub and blade, or in between blades. Within the GRC project a hub-to-blade mounted hydraulic damper is used. This damper can be used to regenerate energy.

In road vehicles, utilising dampers to harvest energy is a technology which is under development. Electromechanical [4] and hydraulic [73] damper prototypes have been built which can decrease the fuel consumption of light-duty vehicles by up to 10% [4]. These dampers recover hundreds to thousands of watts. For a health monitoring system, milliwatts to watts are necessary, depending on the scale. The high mechanical complexity also makes these systems more costly, maintenance intensive and heavy. The electromechanical damper is unfeasible due to the low displacement of the lag damper which is in the order of a few millimetres. A piezoelectric lag damper harvester is presented which requires the least mechanical changes and best preserves the intended operation of the lag damper.

Figure 5.2 (a) shows the damper curve and (b) shows the damper velocity for forward flight at 130 knots (66.9 m/s). This result is generated using the same flight data as used in chapter 4. The precise damper profile is given in appendix F.

From the figure it can be seen that the rotor speed (4.18 Hz) is the dominant frequency. Additionally, as can already be deduced from the specified damper curve, the force developed by the damper is limited to approximately 9 kN. It can already be understood from the waveform –which clearly resembles a square wave– that this force is also generated for those flight conditions where there is only a moderate forward velocity. The fact that the damper develops this force very quickly, and then limits the force, makes it quite suitable as a candidate for a piezoelectric energy harvester. The stack can be strained close to its limit during normal operation without the possibility of overloading it. More extreme motion of the blade will lead to only a marginally higher damper force. A safe design is more straightforward than the concept which is discussed in chapter 4. The patches in the blade are directly subjected to larger strains than calculated in the case of extreme manoeuvres, making the in-blade concept more sensitive to unknown blade dynamics.

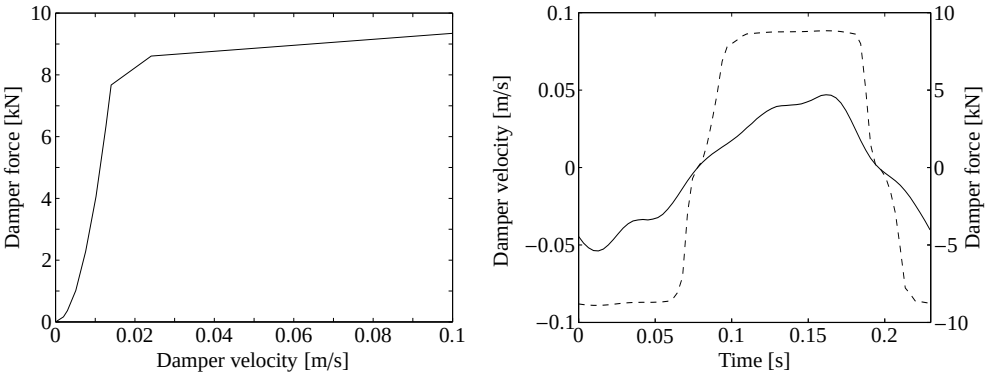

(a) Characteristic curve of the GRC lag damper

(b) Velocity (——) and force (– – –) for one rotor revolution

Figure 5.2: Lag damper data from the GRC project.

In most applications the stack design is far too stiff to be of use for power harvesting [39]. For small loads, even up to hundreds of Newtons, an amplifying device is necessary [74]. However, the high force generated by the damper is well-suited for this mode of actuation, making maximum use of the high coupling factor associated with the 33-mode. By mounting a stack directly in series with the damper, all forces pass through it. Additionally, the minimal displacement associated with the stack will minimise the influence it has on the dynamic properties. Research [15] also shows that, contrary to harvesting beams with patches, piezoelectric stacks exhibit a high electromechanical conversion efficiency at lower frequencies instead of near resonance.

Converting the lag damper to a piezoelectric power harvester can be done very similarly to how piezoelectric stacks are designed. A design concept is presented in figure 5.3. The damper casing and piston are left unchanged. The rod of the piston is made hollow and a stack is inserted. At the end of the rod the mounting lug is redesigned to allow for some axial displacement, in order to accomodate the deformation of the stack. A few tenths of a millimetre is already sufficient. The lug is then also inserted into the rod and a pack of belleville springs is installed to apply a 9 kN prestress on the stack. These springs are characterized by a very high stiffness, regressive characteristic and compact form factor. However, the end of the rod may require a larger diameter to accommodate the spring pack. The new mounting lug and prestress assembly are secured by a cap which is screwed into the rod.

In section 5.2 an electromechanical model is developed in order to describe the dynamics and piezoelectric state of this concept. Additionally, some predictions concerning the power output are made based on a quasi-static approach of the piezo stack and the applied load. In section 5.3 a MATLAB/Simulink model is developed which is used to more accurately predict the power output. The *Simscape* plug-in allows multiple domains within a single model. The electrical circuits can therefore be modelled along with the mechanical domain.

The work presented in this chapter was done parallel to that of chapter 4 where the

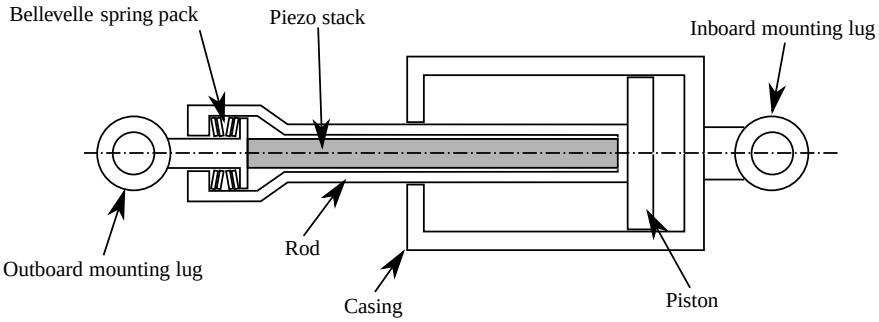

Figure 5.3: Conceptual drawing of the cross section of a piezoelectric lag damper.

switching circuitry was also ignored. Therefore, only the conceptual operation of the switching circuitry is included in this chapter. More detailed switching circuitry such as the SSHI active switch (appendix E) is not yet included. This is considered in chapter 6. Finally, the feasibility of the lag damper concept is discussed in section 5.4.

5.2 Modelling

This section describes the simplifications made in the mechanical domain in order to develop a basic model suitable for evaluating the concept. Additionally, the issue of coupling is addressed; mainly electromechanical and aerodynamic coupling.

5.2.1 Mechanical model

Simplifications must be made in order to reduce the real blade and lag damper system to a manageable number of degrees of freedom. An additional challenge is the aerodynamic loads which constitute the excitation of the rotor blade. Despite significantly simplifying these two aspects, a satisfactory model is presented in this section.

The first simplification is to consider the blade as a rigid body. Although chapter 4 demontrates the contrary, it is a reasonable assumption when only the lag damper is considered. Figure 5.2 supports this claim by showing that the damper excitation is dominated by a once per rotor revolution (1/rev) excitation. The second lagging frequency is visible, but its effect on the damper force is marginalised by the damper curve.

This first assumption already leads to the Ideal Physical Model (IPM) shown in figure 5.4. The blade is lumped into the rotational inertia J, an intermediate mass M between the damper and piezo stack, associated displacement u, an equivalent blade hinge stiffness k_{eq}, blade lead angle ξ and moment excitation M_0. The first lagging frequency is a result of the rotor speed and the associated dynamic stiffness. The equivalent stiffness k_{eq} is determined, based on the first lag frequency and inertia of the blade.

The second simplification is that a sinusoidal once per revolution excitation is assumed. The amplitude of the excitation can be determined in a number of ways. The peak force can be taken to be equal, the lag angle amplitude, or more interesting in this case: the

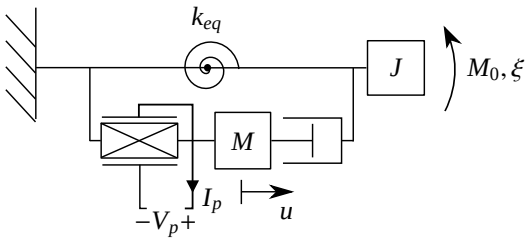

Figure 5.4: Ideal Physical Model of the simplified blade, damper and stack.

power dissipation within the damper. Using a Simulink model of the IPM of the mechanical domain, a sinusoidal load of 10.7 kNm equals the dissipation of the model to the data from Agusta Westland at 245 W. Figures 5.5 show the resulting damper velocity and damper force waveforms for one revolution in comparison with the AW data. Although the damper velocity shows quite some deviation due to the simplification, the insensitivity of the damper to velocities above 2 cm/s (see figure 5.2(a)) leads to excellent agreement of the damper force between the two. It is the latter that forms the prime excitation for the piezoelectric stack, justifying the aforementioned simplifications. The AW model also includes an aerodynamic model and the effects of aerodynamics on the blade dynamics. From figure 5.5(a) it can be concluded that neglecting this effect is acceptable. The resulting mechanical model data are summarised in table 5.2 towards the end of this section.

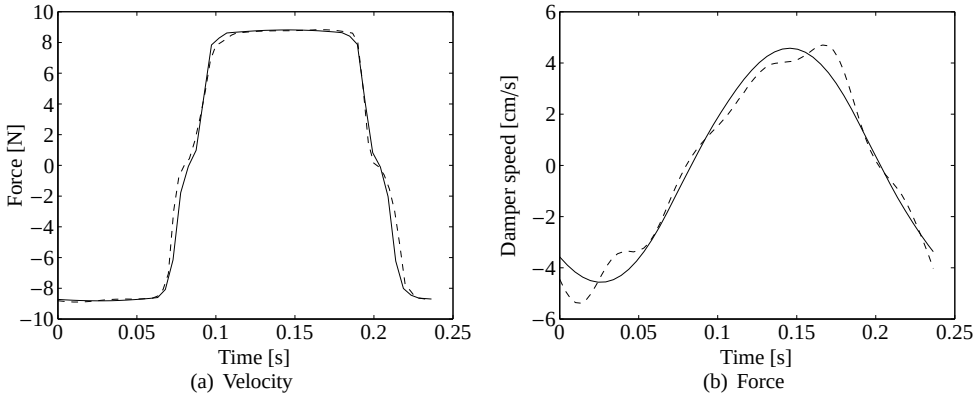

Figure 5.5: Damper force and velocity profile comparisons between simulation (——) and AW data (– – –) (AW data summarised in appendix F).

5.2.2 Piezoelectric stack

In order to maximise the output of the concept the proper piezoelectric material must be chosen. As mentioned in chapter 2, the coupling factor k_{33} of the material is the leading

parameter in the selection process. First and foremost this parameter must be maximised.

Second, piezoelectric materials are categorised into 'hard' and 'soft' materials, giving an indication of the stiffness and durability of the material. Durability in this case is in the electrical sense. A hard material possesses a lower domain mobility and strongly resists re/depolarisation (recall the coercive field strength in section 2.1). This aspect is particularly important for the active circuits which, when designed correctly, can significantly boost the voltage beyond the open circuit value leading to large negative electrical fields.

A third value which also relates to the electrical robustness is the Curie temperature (section 2.1). The higher this value, the better. This and the second criterion both relate to some extent to the coercive field strength of the material. As a rule of thumb, depolarisation begins at a negative voltage field strength of roughly half of the coercive field strength (private communication with *PI*).

From the materials available from *Physik Instrumente*, the choice settles on PIC181 material. Although it does not have the highest coupling factor –some soft materials have a slightly higher k_{33}– the combination of coupling factor and voltage capabilities makes it the best choice. The relevant material properties are summarised in table 5.1. The material choice is not discussed in further detail as it is not relevant to the research goals in chapter 1.

Table 5.1: Relevant material properties for PIC181.

Property	Symbol	Value	Unit
Relative permittivity	ϵ_r^{ε}	1135	-
Piezoelectric voltage constant	e_{33}	14.7	N/Vm
Youngs modulus (plane stress)	E_{33}^{E}	70	GPa
Coupling factor	k_{33}^2	0.38	-
Coercive field strength		2	MV/m
Maximum safe compressive stress	σ_{max}	120	MPa

Additional considerations relate to the geometry of the stack. The rod of the lag damper provides space for at most a 2 cm diameter stack. The maximum length is in the order of 25 cm (both resulting from private communication with AW). The last choice with respect to stack geometry is the layer thickness. This aspect will be shown to be weakly dependent on the choice of the electrical circuit, and will be addressed separately for each. The maximum allowed dimensions of the stack are chosen to be a length 25 cm and an area of 3.14 cm^2.

Following determination of the stack geometry the (undamped) natural frequencies can be calculated. These are also listed in table 5.2. The first relates to the blade lagging motion, with the stack degree of freedom u moving in phase with the blade. The second eigenmode is that of the stack between the two masses, u and ξ show a 180 degree difference in phase. In reality this second frequency is heavily damped but its comparatively high value serves as justification of the decoupled blade/stack approach which is used extensively in the remainder of the chapter.

5.2.3 Coupling considerations

Some investigation into the aeroelastic and electromechanical coupling are also necessary. From a purely piezoelectric standpoint, the coupling of the stack is significant as it is equal to k_{33}. However, when considering the definition of electromechanical coupling by [20] the mechanical damping also plays a role.

In [20] the ratio k_e^2/ζ is used. This ratio is valid when the stack and damper act in parallel. It indicates how much energy the stack dissipates relative to the other damping sources, in the analytical case it is linear viscous damping. When the ratio is low, little power is dissipated electrically and the influence of the harvester on the overall behaviour is minimal. When the ratio approaches and increases beyond unity the harvester is the dominant source of damping and the dynamics are dominated by it.

In this case, the viscous and electromechanical damping act in series and the displacements are not identical. Therefore it is necessary to evaluate the energy dissipated by each. The damper has already been determined to dissipate nearly 250 W, whereas the stack will be shown to generate in the order of watts. The damper still dominates the system and low coupling can be assumed for the lag damper harvester. Considering the orders of magnitude difference between the dissipated energy of the damper and stack, it is reasonable to assume that the overall dynamics will not be influenced by the additional damping introduced by the power harvester. A fully coupled aerodynamic-structural-piezoelectric model is not necessary during this step.

5.2.4 Parameters of the Ideal Physical Model

The mechanical and piezoelectric parameters of the ideal physical model are listed in table 5.2. Dimensionless parameters are listed as well. The natural frequencies are the undamped and short-circuited values.

The stack diameter is calculated based on the maximum permissible stress and hence it represents an absolute minimum value. Ceramic material does not tolerate tensile stresses, so compression must be maintained even as the damper itself generates the maximum negative force. A total compressive stress of 18 kN is therefore used to determine the minimally required cross section. This is combined with a maximum material stress of 120 MPa (PI specification). The stack layer thickness is not listed but does not influence the electromechanical coupling.

5.3 Simulations

With the mechanical model established, it is possible to simulate various circuits to investigate the results. This section is subdivided into parts pertaining to each circuit. The geometry of the stack is determined separately for each circuit as the limitations and possibilities of each circuit may lead to a different cross section.

The simulations are solved using the MATLAB *ode15s* solver [75]. This is a numerical solver for ordinary differential equations which utilises numerical differentiation formulas. Although less accurate than other solvers available within Simulink, this solver is the only one availble that is capable of handling rapidly changing system parameters. Consider the

Table 5.2: Mechanical parameters lag damper IPM.

	Property	Symbol	Value	Unit
Input	Equivalent hinge stiffness	k_{eq}	143	kNm/rad
	Blade inertia (relative to hinge)	J	2387	kgm^2
	Excitation moment	M_0	10.7	kNm
	Lag damper piston mass	m	1	kg
	Stack area	A	1.5	cm^2
	Stack length	L_s	25	cm
	Rotor frequency	Ω_R	26.26	rad/s
Model parameters	Stack stiffness	k_p	42	MN/m
	Stack weight	m_s	0.293	kg
	First lag frequency	ω_{m1}	8.1	rad/s
	Second natural frequency (stack)	ω_{m2}	6527	rad/s
	Damper force amplitude	F_0	8819	N
	Normalised excitation frequency	Ω	0.0040	-
	Stack coupling parameter	k_e^2	0.38	-

switching of active circuits or the on-off characteristics of diodes. It is also capable of handling order of magnitude differences in frequencies. Compare the excitation frequency with the stack frequency and the electrical natural frequency in the case of the SSHI circuit of section 3.6. This is also one of the few available solvers which is able to converge to the exact time at which these changes in parameters may occur, preventing instablities associated with other solvers that do not have this capability.

The maximum allowed time step used in these simulations is one twentieth of the period of the highest eigenfrequency which is present in the system. For the DCIM circuit this is one twentieth of the rotor period and for the active circuits this is one twentieth of the oscillation period associated with the capacitor-inductor resonance frequency. This is determined through trial and represents a balance between stability and computation time.

The desired result is the power delivered at the electrical load. To accomplish this, the DC voltage across the load and storage capacitor must first stabilise, requiring the simulation to be run between ten and fifty oscillations of the blade, depending on various parameters. The power resulting from each simulation is calculated by integrating the instantaneous output over the last cycle of the simulation, once the DC voltage has stabilised:

$$P_{avg} = \frac{1}{T}\int_T \frac{V_{dc}(t)^2}{R}dt \tag{5.1}$$

5.3.1 DCIM

In this case the limitation of the stack geometry is the mechanical stress. Using a quasi-static approximation of equation 3.5 the following is found for the power at the optimal resistance (equation 3.6):

$$P = \frac{F_0^2}{m\omega_{m2}} \frac{k_e^2 \Omega}{\pi (2 + k_e^2)} \tag{5.2}$$

By inserting the non-dimensional values and the physical values for mass, force and natural frequency from table 5.2, the power is found to be 2.5 W.

So far the layer thickness has not been specified. In this case values are chosen in the range of what is commercially available: 100 µm and up. Based on this the stack capacitance can be calculated and consequently the optimal resistance. Lastly, the storage capacitance C_s is calculated by rewriting equation 3.4 to solve for C_s as a function of V/V_c. Additionally, the force coefficient θ is calculated. These values are redetermined for each new layer thickness.

The implementation of the circuit in the *Simscape* model is straightforward since all components are readily available. Only the piezoelectric element must be modelled with a number of components to ensure it functions using the e_{33} value. For each stack geometry the simulation is run until the DC voltage stabilises towards an asymptotic value.

The results of the simulations are shown in figure 5.6. It compares the simulation results, with equation 3.5 in which only a stack is subected to a sinusoidal load with an amplitude identical to the peak damper load. The normalised results of the latter are rewritten to physical values. The agreement is excellent, demonstrating that the claim in section 3.4 is true. The output of the DCIM circuit is insensitive to the load path provided that one dominant frequency with associated amplitude is present.

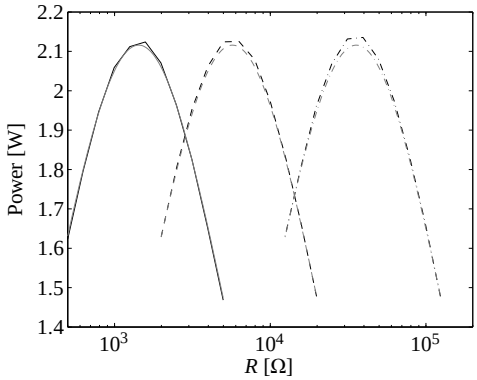

Figure 5.6: DCIM results for $t_l = 0.1$ mm (——), $t_l = 0.2$ mm (– – –) and $t_l = 0.5$ mm (– · – ·). Simulation in black and equation 3.5 in grey.

5.3.2 SECE

The SECE circuit (section 3.5) operates predominantly in open circuit mode, the maximum voltage must be calculated in order to ensure that the maximum reverse bias of the piezo is not exceeded. The lag damper harvester operates quasi-statically, therefore the maximum voltage is calculated using the static piezoelectric equations 2.8 in an open circuit condition. In accordance with [17] the following is found for the maximum voltage and subsequently the minimal cross section A:

$$V_{max} = \frac{2\theta}{C_p} u_0 = \frac{2\theta}{C_p} \frac{F_0}{k_p + \theta^2/C_p} \tag{5.3a}$$

$$A = \frac{2e_{33}F_0}{E_{v3}\left(E_{33}^E \epsilon^\varepsilon + e_{33}^2\right)} \tag{5.3b}$$

The minimal cross section is 3.3 cm^2 for PIC181, significantly larger than the stress-limited value of the DCIM circuit. Moreover, this value exceeds that which is specified by AW as what can fit within the damper. For the sake of analysis the circuit is investigated nonetheless as other methods can be devised in order to reduce the voltage. Consider, for example, coupling an additional capacitor in parallel with the stack.

A first approximation of the power is found using the open circuit voltage equation 3.10 and the analytical power equation for the SECE circuit (equation 3.11). The capacitance and voltage are written out in their constituent variables yielding:

$$P = \frac{1}{2} C_p V_{max}^2 = \frac{1}{2} \epsilon^\varepsilon \mathcal{V} E_{v3}^2 \frac{\omega}{\pi} \tag{5.4}$$

The volume of the piezo stack is represented by $\mathcal{V}$. The displacement is present in this equation through the minimal surface area A, which in turn is driven by the maximum allowed voltage. It indicates 2.85 W of power from the SECE circuit.

The circuit is simulated for various layer thicknesses t_l and load resistances R. The relevant calculations for the various component parameters are given in appendix D. The electrical natural frequency is chosen to be 5 times the rotor frequency Ω_R. This appears low, but the discharge duration is only a quarter cycle of the electrical period, leading to a discharge time of one twentieth of the mechanical period. The stack discharge duration must also be sufficiently long such that the stack does not excite the mechanical domain. This effect is twice as strong for the SSHI circuit, so the main discussion of this aspect can be found in section 5.3.3. The discharge time must at least be in the order of milliseconds to prevent large impulse loads in the damper.

On top of the induced mechanical loads in the case of too rapid a discharge, the SECE circuit has another peculiar result. After the first discharge the mechanical damper must settle to a new equilibrium. In doing so, the stack is deformed further and voltage is again built up from zero. An example of the voltage and resulting primary and secondary currents is shown in figure 5.7. The overlap of currents, although unclear if it is detrimental to performance, can be avoided through careful design. This is far more complex than using a slow discharge and in the end the simulations indicate no power benefit. Note that for the slow case the current associated with these additional discharges is already generated during the discharge phase as the stack is being compressed or stretched further.

The resulting circuit parameter ranges are given in table 5.3. Note that while, for example, the layer thickness is shown in increasing order, other parameters are shown in decreasing order. This coincides with the lower and higher boundary for the layer thickness. The same holds for the storage capacitance and load resistance through the desired minimum RC_s time.

In order to determine the required simulation time, simulations are first run for the extreme values of the thickness and load resistance for 100 cycles, and then again for 25

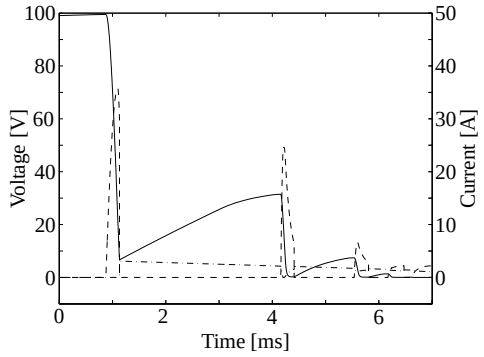

Figure 5.7: The multiple discharge effect demonstrated around one force maximum. Stack voltage (——), primary current (– – –) and secondary current (– · – · –).

Table 5.3: SECE circuit parameters.

	Parameter	Symbol	Value	Unit
Input	Stack area	A	3.3	cm^2
	Layer thickness	t_l	25-500	μm
	Capacitance	C_p	1100-2.17	μF
	Electrical natural frequency	ω_{el}	1313	rad/s
	Primary inductance	L_1	0.055-21.9	H
Model parameters	Secondary inductance	L_2	0.042-4.2	H
	RC time storage circuit	RC_s	2.3	s
	Discharge time L_2	t_{off}	10	ms
	Load resistance	R	0.1-10	kΩ
	Storage capacitance	C_s	23-0.23	μF

cycles. The latter all settled to within 1% of the power value resulting from the longer simulation of the same initial settings. Due to the high damping, the mechanical domain settles into a cyclic motion within 1 second. Therefore, the remainder of the transient simulations are run for 25 cycles, for the whole range of thicknesses and load resistances, yielding the result of figure 5.8. The power begins to decrease for the small layer thickness; this is due to the limited peak voltage which can be attained in combination with voltage drops in the diodes.

The power from the SECE circuit exceeds the value predicted from the analytical approach. The cause may be found in the higher coupling. In [17] low coupling is assumed so the additional displacement following a discharge of the piezo element is neglected. In this case the stack is compressed further (k_e^2 times the displacement amplitude) as it is being discharged. The additional current is immediately transferred to the inductor. The higher output can be accounted for in this manner.

Moving to more detail, a few limitations arise. Rewriting equation D.8 in terms of the piezo material volume and material parameters, the following is found for the currents and

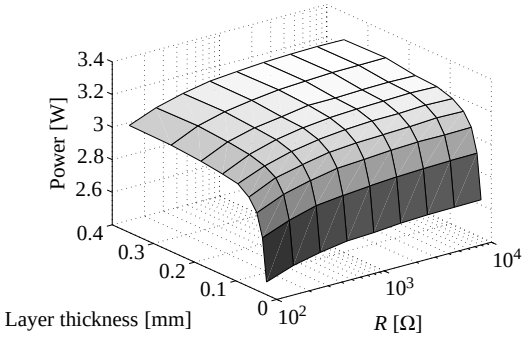

Figure 5.8: Power versus layer thickness and load resistance for the SECE circuit.

inductance values:

$$L_1 = \frac{t_l^2}{\omega_{el}^2 \mathcal{V} \epsilon_3^\varepsilon} \qquad I_1 = \frac{\epsilon_3^\varepsilon \mathcal{V} \omega_{el} E_{v3}}{t_l} \qquad L_2 = \frac{\Omega_R t_{off}^2 R}{2\pi} \qquad I_2 = \sqrt{\frac{\mathcal{V} \epsilon_3^\varepsilon 2\pi}{\Omega_R R}} t_{off} E_{v3} \tag{5.5}$$

Note that the equations are written as a function of the volume ($\mathcal{V}$) of the stack since this parameter is held constant for the simulations under investigation. Moreover, the power harvested is linearly dependent on the piezo volume, due to the presumption that the material achieves the maximum permissible voltage field. The layer thickness is the only variable that can be used to tune the balance between currents and inductance values. Table 5.3 shows the extreme values found for the inductances. An air-core inductor of more than 100 mH is physically large (a volume of hundreds of cubic centimetres) and the values for L_1 quickly attain unfeasible levels. The same considerations hold for the secondary inductor value.

The SECE circuit can be used in conjunction with the lag damper harvester. However, it brings prohibitive limitations concerning the component parameters. First and foremost is the required stack cross section. This is larger due to the open circuit operation of the stack. A smaller stack area is possible by using an additional capacitor in parallel with the stack, but this will reduce electromechanical coupling. Considering equation 3.11, the power will not change significantly.

Appendix H provides a number of additional plots showing more detailed simulation results concerning currents and inductance values. The layer thickness is limited to tens of micrometres. More than approximately 50 μm will lead to an unrealistically large L_1. For the secondary inductance L_2, the load resistance is the driving factor with an upper limit of approximately 300 Ω. The resulting currents are not yet excessive. From figure 5.8 the maximum power is 3.0 W using these values for t_l and R.

The SECE circuit is limited by the voltage in the stack which drives the geometry. Alternatively, a stack of the same dimensions as the DCIM can be used, with an additional capacitor coupled in parallel. Both options are less than optimal and limit the advantage of the SECE circuit over DCIM.

5.3.3 SSHI

As discussed in section 3.6, the SSHI circuit boosts the voltage above that which can be achieved with the DCIM circuit. The voltage developed in the stack is a function of the inversion efficiency of the circuit, and may be increased beyond the maximum reverse bias when a sufficiently large load resistance R is used. To prevent this event an equation for the maximum allowed load resistance is derived first. Using this value the circuit is then analysed further. Next more practical aspects are discussed. Questions relating to how quickly the voltage is inverted and what effects can be expected are answered. Finally, optimal circuit parameters are chosen and simulations are performed.

Analytical output

Taking the information in appendix E into consideration, it can be seen that the force or stress, geometry and load resistance influence the voltage field in the piezo material. Starting with the normalized voltage equation from equation 3.14 and again assuming a quasi-static mechanical domain, the following can be derived for the maximum load resistance:

$$r_{max} = \frac{V'_{max}\pi}{\Omega\left(2k_{33}^2 - V'_{max}\left(1 - e^{-\pi/(2Q_i)}\right)\left(1 + k_{33}^2\right)\right)} \tag{5.6}$$

Rewriting in terms of the physical variables gives:

$$R = \frac{E_{v,max}t_l\theta\pi}{C_p\omega\left(2F_0k_{33}^2 - E_{v,max}t_l\left(1 - e^{-\pi/(2Q_i)}\right)\left(1 + k_{33}^2\right)\right)} \tag{5.7}$$

These equations are then inserted into the power equation of the SSHI circuit (equation 3.14), giving the maximum amount of power as a function of maximum voltage field and (implicitly) the maximum allowed load resistance. The quasi-static approach gives the following for the power:

$$P' = \frac{4k_{33}^2\Omega^2 r}{\pi^2} \qquad P = \frac{4C_pRk_{33}^2}{m}\left(\frac{F_0\omega}{\omega_n\pi}\right)^2 \tag{5.8}$$

To establish an upper bound for the power output, perfect voltage inversion ($Q_i = \infty$) is assumed. The exponent $e^{-\pi/(2Q_i)}$ becomes unity, and the associated terms of equations 5.6 and 5.7 are zero, nullifying the term associated with the exponent. Substituting the resulting equations for r and R in the power equations 3.14, the normalised and absolute power output become:

$$P' = \frac{2\Omega V'}{\pi} \qquad P = \frac{2F_0\omega E_{v,max}e_{33}L_s}{E_{33}^E\pi} \tag{5.9}$$

The above equations are only valid for excitation frequencies far below resonance of the piezoelectric stack. Additionally, they are only of use when the optimal resistance of the SSHI circuit (equation 3.16) actually leads to too high a voltage field in the piezo material. If this is not the case, equation 3.16 holds. The most peculiar fact is that the maximum available power is independent of the volume of piezoelectric material, but is only dependent on the length of

the stack. This is a result of the perfect inversion assumption which is unrealistic. In reality, a large cross section would lead to a larger accumulated charge for a given layer thickness and voltage, and larger currents and associated losses during voltage inversion. There is no strong dependence on the layer thickness, which is consistent with the other circuits.

A maximum power of 7.8 W is found for this concept when using the material data from PIC181, 25 cm stack length and the lag damper data. This value does not take the power consumption of the SSHI circuit itself into account.

Circuit parameter considerations

Being an active circuit, the SSHI circuit may induce rapid voltage changes in the stack. Due to the electromechanical coupling the force equilibrium in the stack changes. Although the stack is in series with the damper this change in equilibrium can occur sufficiently quickly such that large momentary velocities occur following the voltage inversion. Large force variations in the rotor can be generated since the damper force is dependent on the velocity. Minimising these induced impulses means minimising the associated natural frequency, thereby slowing the deformation of the stack during inversion.

In appendix E, the electrical natural frequency ω_{el} associated with the voltage inversion is calculated assuming low coupling. It is therefore independent of the mechanical domain. Due to the high stack coupling this is no longer the case and a coupled approach is needed, in particular when the mechanical and electrical eigenfrequencies are of a similar order of magnitude. During voltage inversion the stack voltage is lower than the DC voltage, meaning the rectifier is blocked. The following system of equations then holds for the coupled stack - SSHI system:

$$\begin{bmatrix} M & 0 \\ 0 & C_p \end{bmatrix} \ddot{q} + \begin{bmatrix} c_s & \theta \\ -\theta & R_L \end{bmatrix} \dot{q} + \begin{bmatrix} k_p & 0 \\ 0 & \frac{1}{L_1} \end{bmatrix} q = 0, \qquad \dot{q} = \begin{pmatrix} \dot{u} \\ V \end{pmatrix} \tag{5.10}$$

Note that the blade degree of freedom is neglected here; it is assumed constant. As indicated in section 5.2 this is justified due to the rigid blade model and the low frequency associated with the blade motion. Inversion occurs at the moment that the force is maximised, implying a high damper velocity. This equation is therefore valid as long as the absolute damper velocity remains above 0.02 m/s (see figure 5.2(a)), preventing variations in the damping coefficient c_s. This approach is valid since minimal disturbance of the damper operation is the goal. It can be concluded that the electrical natural frequency must be lower than the stack frequency, in order to prevent excitation of the eigenmode of the stack. Equation 5.10 is solved in order to determine the inversion time associated with a given setup, which is then used in the simulation to control the switch.

An additional consequence of too rapid a voltage inversion is in the form of energetic losses in the system due to piezoelectrically induced motion of the damper. Figure 5.9 shows the normalised voltage during inversion for two cases. The horizontal axis is normalised with the inversion time of the respective inversion case, which gives unity when the inversion is completed. For the slow inversion, the process is stopped at the optimum point and then remains stable. The fast inversion case initially progresses nearly identically to the slow case. However, upon completion of inversion, the mechanical domain is in a configuration far from equilibrium. Therefore, following inversion the mechanical domain begins to oscillate. Only

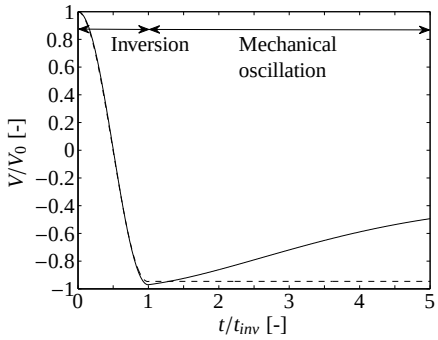

Figure 5.9: Normalised piezo voltage during and after inversion for ω_{inv} = 12500 rad/s (——) and ω_{inv} = 450 rad/s (– – –).

the onset of the vibration is shown in figure 5.9. The voltage oscillates around approximately $V_p = -0.45$ V and is damped out within a few cycles. This effect will be addressed again along with the results.

Ideally, the inversion should take as long as possible to minimise losses. Considering the damper force - time graph of figure 5.5, the maximum inversion time can be in the order of milliseconds. In combination with the large stack the required inductance may become prohibitively large, representing a constraint on the design parameters.

Another consequence of the induced forces due to voltage change is that it may influence helicopter comfort and stability, leading to more vibration and associated fatigue issues. All discussed aspects require as slow an inversion process as possible.

Simulation results for the ideal circuit model

The results presented in this section are from a model that does not include the self-powered switching circuit, but does perform the switching operation. The duration that the switch is closed is determined using equation 5.10. The input data is given in table 5.4. Note that the layer thickness as well as the inversion time is varied, yielding a large range for the inductance.

Figure 5.10 shows the output for varying inversion time and layer thickness. A number of conclusions can be drawn from this result. First, the insensitivity of the output to the layer thickness is clear from the figure. Secondly, the hypothesis of too small an inversion time leading to a lower output is also confirmed. Not shown in the figure is that for $t_{inv} < 0.1$ ms the output asymptotically approaches ~4.8 W. Lastly, the surface plot approaches a maximum output near the 7.8 W predicted by the analytical approach. For a Q_i of 10^3 the simulation gives 7.45 W as the output. The surface plot is not complete for larger layer thicknesses and inversion times. This is done to demonstrate the influence of the inductance value. Similar to the SECE investigation, a limit of 100 mH is imposed on the inductance.

Figure 5.11 shows the resulting waveforms for the piezo and DC voltage for a layer thickness of 50 μm. The piezo voltage in the simulation converges towards approximately 50 V which is the limit given the layer thickness, demonstrating the validity of equation 5.7.

Table 5.4: SSHI circuit parameters.

	Parameter	Symbol	Value	Unit
Input	Stack area	A	1.5	cm^2
	Layer thickness	t_l	50-200	μm
	Inductance	L_1	0.012-480	mH
	Inductor quality	Q_i	100	-
Model parameters	Capacitance	C_p	121-7.5	μF
	Inductor resistance	R_L	3.2-158	mΩ
	Inversion time	t_{inv}	0.12-7	ms
	Load resistance	R	329-5264	Ω
	Storage capacitance	C_s	7.1-0.44	mF

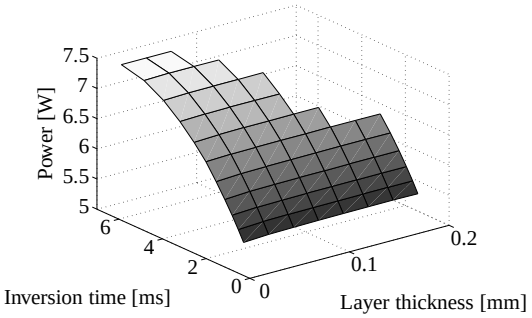

Figure 5.10: SSHI output for varying inversion time and layer thickness.

If the chosen RC_s time of the storage circuit is too small, the sawtooth-like shape of the DC voltage increases in amplitude around the limit voltage, potentially leading to too high a stack voltage.

The resulting damper force for varying inversion time is given in figure 5.12, only the time around the inversion is shown. It shows the large force impulse generated by the lag damper in case of quick inversion. The necessity for as long an inversion duration as possible is again emphasized. The force variation associated with $t_{inv} = 7$ ms is 2.5% of the damper force at the onset of inversion.

A final consideration concerns the inductor used in the circuit. Analysis and simulation reveal that a large inductance in the order of 10-100 mH is necessary to maximise the output and to minimise force variations in the damper. Such an inductor typically utilises a ferrite core to maintain a packaging of a few cubic centimetres. Such a core may suffer from core losses due to eddy currents and electrical or mechanical hysteresis of the material. A ferrite core may therefore not ideal in terms of circuit operation.

The inductance of a coil is dependent on the shape, number of windings and the magnetic permeability of the core material. The relative permeability is defined relative to the

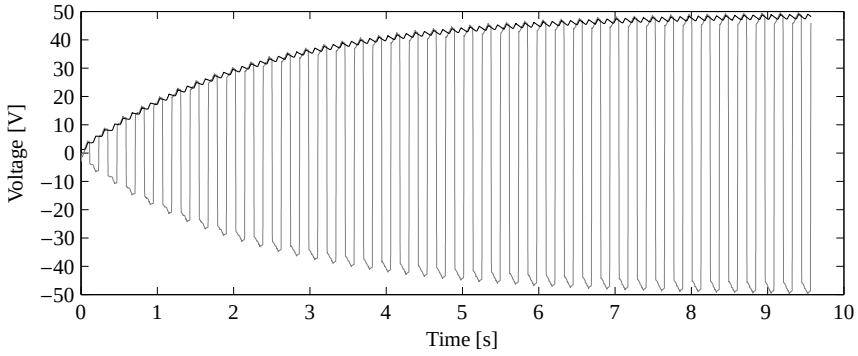

Figure 5.11: Piezo voltage (——) and DC voltage (——) for $t_l = 50\mu m$, $Q_i = 100$ and $t_{inv} = 7ms$.

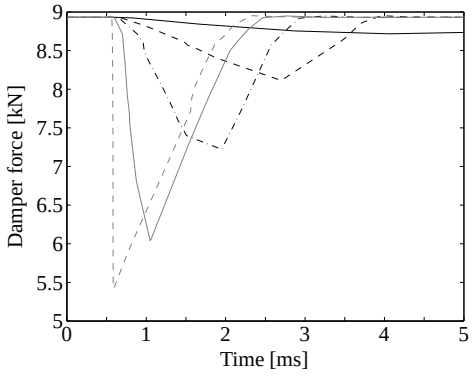

Figure 5.12: Damper force during voltage inversion for $t_{inv} = 0.011$ ms (– – –), 0.50 ms (——), 1.6 ms (– · – –), 3.1 ms (– – –) and 7.0 ms (——).

5

absolute permeability of vacuum. The relative permeability of air is close to unity and the aforementioned ferrite cores have a relative permeability in the hundreds or thousands. A ferrite core inductor of 100 mH can be as small as a cubic centimetre. An air core inductor with the same inductance and dimensions possess a poor quality factor. An air core with similar inductance and a high quality factor will have a major dimension in the order of 10 centimetres and contain hundreds of grams of wire. Core design presents the main limitation for the lag damper with an SSHI circuit.

Considering the challenge presented by the inductor parameters, additional simulations are run with different values for Q_i. Table 5.5 shows the results for a Q_i down to 3, which can be considered an exceptionally poor inductor. The optimal load resistance R is recalculated for each simulation to ensure that the piezo material is used to its full extent. The results show that even for a very poor inductor the SSHI circuit still generates a reasonable amount of power compared to the case with an exceptionally high quality factor.

Table 5.5: Power output for varying Q_i.

Q_i [-]	Inversion efficiency [-]	Power [W]
100	0.98	7.3
20	0.92	7.0
10	0.85	6.7
5	0.73	6.2
3	0.59	5.7

5.4 Discussion

The viability of the lag damper harvester concept is discussed in this section. Each circuit will be addressed as each has its own points of interest and research goals in order to improve overall system performance. Additional work from the literature is also introduced. Lastly, the overall concept of the lag damper harvester is discussed.

5.4.1 DCIM

The DCIM circuit is feasible. It is not the best performing circuit, but it is an application of technologies that all exist and have been researched sufficiently. There are no fundamental question marks in the development chain.

There are also no strict requirements with respect to the stack geometry other than that the cross section should be chosen as small as possible, while taking the maximum stress into account. The only serious consideration is the layer thickness which determines the capacitance, optimal load resistance, and optimal operating voltage of the circuit. The choice of the layer thickness can best be made in conjunction with the requirements of the electronics connected to the harvester.

With a maximum expected output of around 2 W, the DCIM version can already supply more than enough energy to power a health monitoring system within medium scale blades. This also implies that it is sufficient for larger blades than the 8.15 m one which is assessed in the simulation stage. Additional research on smaller blades will aid in assessing the viability for smaller rotorcraft.

5.4.2 SECE

The SECE circuit provides improved output over the DCIM circuit, generating approximately 3 W of power. The main advantage is the absence of an optimal resistance. The result is that the piezo element will always generate the maximum amount of energy, regardless of the electrical load and DC voltage. This makes the circuit more robust with respect to load variations such as intermittent wireless transmission which is a significant power consumer.

An important aspect to consider is that the control electronics for discharging were not modelled. In [17] this additional circuitry consumed 30% of the energy flowing from the piezo element. The details of the used circuitry are not disclosed fully in [17], it is unclear whether this loss is a fixed percentage of the output or if scaling provides any benefit. The

SECE circuit provides only a marginal power benefit over DCIM in the case of a fixed percantage loss.

In [19] the SECE circuit appears to outperform the DCIM circuit by a factor of 4. This result is found using a harvesting beam and 31-mode operation of the piezo. The important fact is that there were no issues with the voltage reaching critical levels. In this research the stack is dimensioned to maximise voltage and power output using 33-mode operation. The high coupling associated with this mode leads to much higher voltages for the same strain, and the voltage limitation is therefore detrimental to the relative performance. The resulting stack area is also too large to fit within the damper rod and other techniques are required to limit the voltage.

As demonstrated, in dimensioning the stack and circuit a trade-off exists between the required inductance values and currents, presenting some design rules for this circuit. As the coupling and stack length decrease, the discussion concerning the discharge duration becomes less relevant. The piezo material then does not deform as much during a discharge, and will not induce such high force variations.

Although not explored in this work, the voltage issue can also be mitigated by using the smaller stack based on the peak stress, and coupling it to a capacitor which is sufficiently large to limit the voltage build-up. This effectively means lowering the coupling coefficient k_e^2. By doing so, the advantage of the narrower stack is immediately and almost completely lost to the reduction in coupling. This option does, however, create more flexibility by tuning the additional capacitance to the mechanical load, in order to maintain the maximum possible output.

Another fail-safe option consists of using a *Zener diode* to limit the voltage in the stack. This diode functions similarly to a normal one, with the added functionality of being able to pass current unimpeded in the opposite direction upon reaching a specific voltage: the Zener voltage. Where normal diodes fail with too large a reverse voltage, the Zener diode is used exactly for this functionality. This functionality should only be used as a fail-safe because it dissipates energy.

Considering the difficulties associated with the SECE circuit, and the marginal power advantage it offers over the DCIM circuit in this case, it does not appear to be a practical circuit for the lag damper.

5.4.3 SSHI

Similar to the SECE circuit, the SSHI circuit is limited by the maximum voltage field within the material. Since it is still continuously coupled to a rectifier and large capacitor, the voltage can be limited through use of the load resistance, and a Zener diode as a fail-safe.

The output which is achieved in the simulations is significantly higher than the DCIM and SECE circuits. Assuming all linear components, approximately 7.5 W per damper appears possible, which is sufficient for health monitoring systems. The SSHI circuit may also extend the concept of power harvesting in the rotor to rotorcraft that are smaller than what is still sensible in the case of the DCIM circuit.

As with the SECE circuit, the SSHI circuit is voltage limited. This leads to interesting effects when compared to section 3.7 and the literature [19]. The active circuits generate significantly more power than the DCIM circuit for non-resonant conditions. Here, the

maximum attained voltage presents a limitation which is detrimental to the power output. Although there is still a factor 3 increase of the SSHI circuit over DCIM, more is not possible. Had the voltage not presented a limitation, the output could increase up to tenfold over DCIM [19].

It has been extensively demonstrated that the voltage inversion process, that is inherent to the SSHI circuit, must take as long as possible. The reasons are twofold: this will minimise load variations in the mechanical domain and also improves the output of the harvester. As with the SECE circuit, the physical dimensions of the inductor once again present a limitation. With fewer parameters to determine, the implementation of the SSHI circuit is simpler than the SECE variant.

Note that the issue of the duration of the voltage inversion or discharge process is irrelevant in the case of low coupled systems. The induced vibrations will be very minimal. It is also not an issue for resonant systems, where large vibrations at the relevant natural frequency are desired. The effects are only relevent for high coupled non-resonant systems.

All the required theory and circuit design which is necessary to build an SSHI harvester damper is available in this chapter and in the literature [25, 56, 76]. The study shows a significant increase over the DCIM voltage output, generating over 7 W of power in the case of linear components. Compared to the SECE circuit, the SSHI performs better and is easier to implement. Challenges associated with the circuit are the inductor size and the influence of the voltage inversion on the helicopter.

5.4.4 Non-linear and temperature effects

The results obtained in this chapter are calculated using fixed component values for, for example, the maximum reverse bias and the permittivity of the piezo material. In [70] additional simulations are presented using varying input parameters.

Research [77] shows that the permittivity of piezo ceramics may vary significantly with changing operating conditions such as mechanical stress and voltage field. A generic capacitance model is used in [70] in order to explore the effects on the various circuits. Summarising the results for the DCIM circuit, the output decreases for increasing permittivity. This is expected, considering the influence of the coupling in equation 3.7. If only the permittivity increases, the coupling coefficient k_e^2 decreases. The SECE circuit benefits from an increasing capacitance because the stack geometry is voltage limited. With increasing capacitance the cross section can decrease, and more charge is displaced for a given force. The SSHI circuit is comparatively insensitive to changes in capacitance, provided the components can handle the higher current. The load resistance can be re-tuned to meet that requirement.

The coercive field strength and maximum reverse bias both reduce with increasing temperature (section 2.1). In [70] the temperature is increased to 70 degrees Celsius, which reduces the coercive field strength by approximately 30%. The DCIM circuit is not influenced, because the developed voltage field at the optimal load resistance is only 50% of the maximum reverse bias at room temperature. The SECE circuit, being voltage limited, shows a reduction in power of more than 30%. The SSHI circuit can again be re-tuned to minimise the effects of the increased temperature. However, being voltage limited as well, the maximum output is still influenced significantly. A reduction in output of approximately 25% is reported.

The SSHI circuit again proves to be the best performing circuit when non-linear behaviour is included. The ability to re-tune the circuit through electronic means is a significant advantage over the SECE circuit. The latter circuit implies that the stack must be designed for a worst-case scenario that reduces the output during normal operation, or extensive electrical safeguards are required to prevent excessive voltage in extreme situations.

5.4.5 Total concept feasibility

It can be concluded from the studies in this chapter that the power harvesting lag damper concept is viable. It adds minimal extra weight to the rotorcraft and, most importantly, it is located inboard. A DCIM version can be implemented without additional research. The SSHI circuit may require additional investigation in to the inversion process and, in particular, the influence on the rotor dynamics, but the results lead to the expectation that this effect is minimal. The SSHI circuit so far does not appear to pose any critical problems.

The most significant aspect is that the power is generated in a centralised location, while the ideal concept of power harvesting is to provide on-the-spot power. While centralised power may not be ideal for most power harvesting systems, in a helicopter blade however, it is not a clear disadvantage. For blade health monitoring devices, centralised power generation will require wiring within the blade in order to power the sensors. It can be debated whether or not the additional outboard weight of a localised harvester (as investigated in chapter 4) gains preference over a limited number of wires per sensor. An independent node not only requires a power source: a self-sufficient node within the blade without external wiring would also require a wireless transmitter, power electronics and storage. The idea of a plug-and-play blade with numerous independent nodes, although technically possible, may very well add too much weight to be sensible. Therefore, centralised generation resulting from the lag damper is an excellent alternative. Most importantly, the initial target of circumventing the necessity for slip rings has been met.

Further strengthening the advantage of centralised power generation is integrated fibre optic sensing in blades. Fibre optic strain sensing is a technology under development [78, 79]. With this technology most of the electronics will be mounted in the rotor hub with the lag dampers close by. Only the optical fibres are mounted in the blade. This would completely negate the need for a power source within the blade. Power consumption of such systems is currently beyond the generating capacity of the lag damper harvester. In the future the power consumption of fibre optic systems may possibly be within range of the generating capability of the medium sized rotorcraft under consideration in this chapter, so that a complete harvesting and sensing system can be realised.

Chapter 6

Validation of the lag damper simulations

The work presented in this chapter has been presented at and published by the European Rotorcraft Forum 2012 [80].

6.1 Introduction

In order to assess the validity of the simulations of chapter 5, experiments are conducted on a lab-scale setup. Simulations similar to those of the lag damper concept are run for the test setup, and the results are compared to experimental data.

Section 6.2 describes the setup used. Non-linear components are characterised in section 6.3. The damper is characterised beforehand. The stack capacitance is measured as well following initial results, revealing some non-linearity of the stack. This reflects upon the agreement between simulation and experimentation. Results of the complete electromechanical setup are discussed in section 6.4 for the ACIM, DCIM and SSHI circuit.

An additional electrical setup, discussed in section 6.5, is built following the complete lag damper setup experimentation. It only relates to the SSHI measurements as this circuit performed significantly poorer than expected in the full setup. Losses in the circuit are determined allowing for more accurate simulation of the SSHI circuit. Lastly, the conclusions are listed in section 6.6.

6.2 Experimental setup

The experimental setup is shown schematically in figure 6.1. Starting from the left, the setup consists of

- a viscous damper by ACE Stossdämpfer, model HBS-28-50, with a 50 mm stroke. It is selected due to its ability to damp in both directions with a negligible free stroke upon reversal. The damper is modified by adding a large aluminium heat sink, manufactured locally, to increase heat dissipation to the surrounding environment;
- the piezo element: a PiezoMechanik PSt150/3.5×3.5/20 stack in an upgraded housing with 400 N preload;

- a Bruël & Kjær 8001 impedance head for load measurement;
- a rod flexure to mitigate alignment errors;
- and a large Bruël & Kjær shaker equipped with a 4819 shaker head for excitation. The moving core has mass M.

Other relevant data are given in table 6.1.

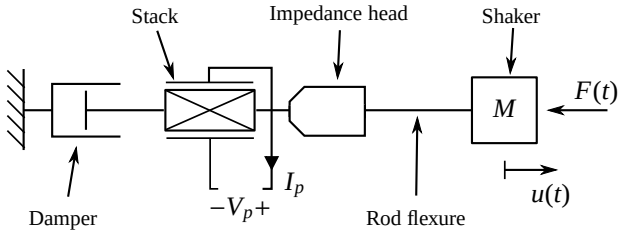

Figure 6.1: Schematic of experimental setup, left to right: damper, piezo stack, force sensor and shaker.

Table 6.1: Mechanical properties of the experimental setup.

	Symbol	Value	Unit
Stack capacitance	C_p	0.96	[μF]
Stack stiffness	k_p	$25{\cdot}10^6$	[N/m]
Force coefficient of stack	θ	1.006	[N/V]
Maximum reverse voltage	V^-	-30	[V]
Mass shaker core	M	0.9	[kg]
Rod flexure axial stiffness	k_r	$13 \cdot 10^6$	[N/m]
Excitation frequency	ω	3	Hz
Axial natural frequency	ω_n	3062	[rad/s]
Electromechanical coupling	k_e^2	0.042	[-]
Normalised excitation frequency	Ω	.0062	[-]

Not shown in figure 6.1 is the thermocouple which is used to monitor the damper temperature. As the damper is cycled, heat is generated. The damper will increase in temperature, affecting the viscosity of the damper fluid. The damping coefficient will decrease as the fluid warms up. To mitigate temperature effects all experiments are conducted at a similar temperature. After setting the excitation of the shaker the setup is allowed to warm up until the temperature is stable, typically around 33 degrees Celsius. All measurements with the damper have been performed in a single setting.

The shaker head velocity is measured using a PolyTec laser vibrometer. Data acquisition is done using a SigLab model 20-42 acquisition system connected to a computer. Force, stack voltage, DC voltage (where relevant) and shaker head velocity are measured. The circuit

voltages are sensed directly using the SigLab unit, although a voltage divider is used to bring the voltages within range of the acquisition box specifications.

The resistance of the measuring branch, totalling 2.8 MΩ, is large enough to be neglected in the measurements regarding any influence on the piezo element (AC) itself. The 1 MΩ internal impedance of the acquisition system implies that the measurement range for the voltages is ±28 V. The resistance of the DC voltage branches can be upwards of 100 kΩ, approaching even 1 MΩ for the SSHI circuit. In order to correctly calculate the electrical load of the DC branch of the circuit, the resistance of the measuring circuit is accounted for. This is also required in order to correctly calculate the dissipated power.

6.3 Component characterisation

In order to simulate the setup as accurately as possible, the components are first investigated separately. The damper curve is determined and fitted with a polynomial for use in the simulations. A number of stack properties are also measured. Initially scalar values are determined for the capacitance and force coefficient θ.

Following the measurements more detailed measurements of the stack were done (section 6.3.3), revealing a significant variation of the capacitance for varying force and voltage. The data is only used in the ensuing discussion. The detailed stack data is not used in the simulations due to the added complexity in the simulation. This would also require detailing the force coefficient under different applied force and voltage for the stack, which is beyond the scope of the research goals. Consider figure 3.20, showing that a broad spectrum of force and voltage must be applied in order to determine the force coefficient for the stack.

6.3.1 Damper properties

The damper curve is determined using the same setup without the piezo stack. The result is shown in figure 6.2, along with a curve fit of the data. A third order polynomial through the origin is fitted to the data in order to acquire a function for use in simulations. The jog in the experimental data (indicated by the arrows) just above and below zero velocity is attributed to the onset of reversal of the damper displacement, leading to stick-slip of the internal seals. For smaller amplitudes this jog maintains a magnitude of 20 N. Smaller force amplitudes are not used since it is unnecessarily difficult to simulate this behaviour. Lastly, the damper appears to function somewhat asymmetrically, note the datapoints given in figure 6.2 which are the highest and lowest points of the measured data. This requires all simulations to be performed using a velocity or position input. This leads to accurate reproduction of the mechanical load extrema, and prevents drift in the damper displacement in case of a symmetrical force excitation.

The excitation frequency is 3 Hz. This makes maximum use of the damper without exceeding the limits of the load cell and piezo stack. It allows for a quasi-static approach of the mechanical system –as with the full scale lag damper– and also maximises efficiency of the stack [15]. From an electrical standpoint, at this frequency the dynamic impedance of the stack is equal to 54 kΩ, significantly smaller than the resistance of the measuring system.

Similar to the full scale damper concept of chapter 5, using a piezoelectric stack could imply that the system possesses high electromechanical coupling. Considering the definition

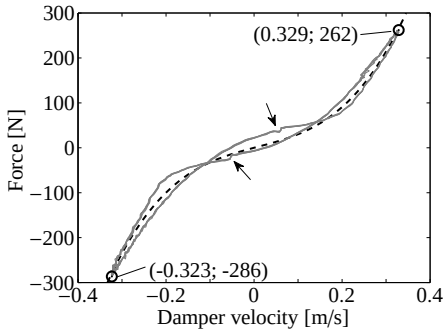

Figure 6.2: Experimental (——) and fitted (▬▬) damper curve.

in [56] once again, the ratio between viscous and piezoelectric damping must be investigated. Stepping ahead to the results, the damper dissipates around 37 W, compared to the mW order of magnitude output of the piezoelectric element the system can be considered to be minimally coupled.

6.3.2 Determination of the force coefficient

The stack is characterised in an open circuit condition in order to determine the piezoelectric force coefficient θ. Figure 6.3 shows the measured waveforms. Then the piezoelectric equations 2.7 are solved for θ yielding a quadratic equation:

$$V_p\theta^2 + F\theta + k_pC_pV_p = 0 \tag{6.1}$$

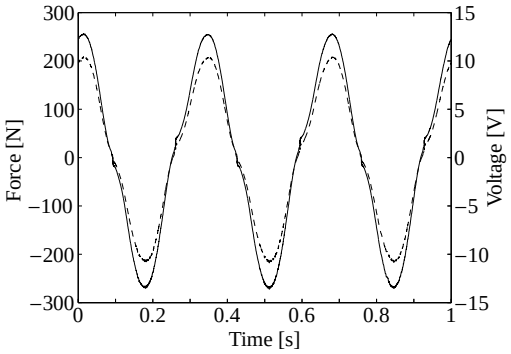

Figure 6.3: Open circuit stack experiment results, force (——) and voltage (– – –) waveforms.

Figure 6.4 shows the solution of interest over time during one cycle. Equation 6.1 yields two solutions. The solution near unity in this case is the correct solution because it is closest to the material specification. The other solution is around 25 N/V which, given the geometry

of the stack, results in e_{33} = 183 Vm/N. The peaks extending beyond the limits of the θ axis are due to the measured voltage approaching zero and therefore have no physical meaning. Equation 6.1 is solved again using the RMS values of the force and voltage, yielding θ = 1.006 N/V and e_{33} = 7.4 Vm/N, which is used in the simulations.

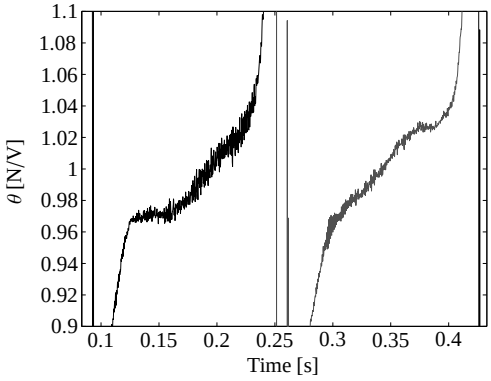

Figure 6.4: Piezoelectric force coefficient θ calculated using constant parameters.

One note concerning the piezoelectric voltage coefficient that is determined from this measurement, is that it appears to be significantly lower than the Piezomechanik specification. The specification gives only a few material parameters and although there is no direct specification for e_{33} its approximate value can be deduced from other similar materials. It should be in the range of 10 to 14 Vm/N, the value found from experiment is rather low.

6.3.3 Determination of the capacitance

Front-running the results of section 6.4, the stack capacitance is investigated following intitial results which show some difference with the simulations. The mechanical part of the setup consists of a lever via which a static load is applied to the stack. The electrical portion is a Keithley 4200 Semiconductor Characterization System (SCS). This device can apply a wide range of voltages, frequencies and currents independently from each other. By monitoring the change of one parameter through the variation of another (e.g. voltage as a function of current) the properties of the attached element can be determined using predefined electrical models.

The SCS applies a constant DC voltage, and superimposes a small AC voltage of 0.1 V. By monitoring the required current, the capacitance at a given DC voltage can be measured. A capacitance in series with a resistor is used as a model of the component. This experiment is repeated for a range of mechanical loads and DC voltages, resulting in figure 6.5. The series resistance is in the order of mW, making it negligible for the remainder of the investigation.

6.4 Lag damper experimentation

The experimental results for the lag damper setup are presented here. Aside from the experimental results, simulation data and a quasi-static analytical approximation for the

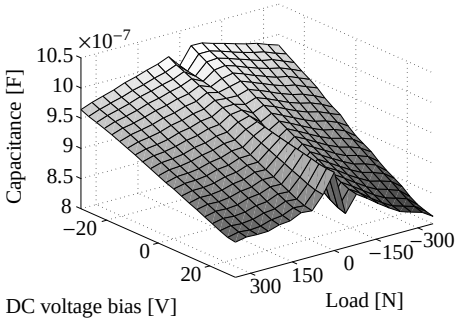

Figure 6.5: Stack capacitance for varying static force (positive value indicates compression) and DC voltage bias (400N pre-load).

setup are presented as well. The force coefficient is taken as a constant 1.006 N/V and the capacitance is also taken constant at 0.96 μF. Three circuits are tested: the ACIM from section 2.6, DCIM from section 3.4 and SSHI from section 3.6. The SECE circuit (section 3.5) is not tested due to a lack of information concerning switch design and also because of the relatively poor results from chapter 5.

Although the previous section shows that the stack capacitance varies, the force coefficient is calculated using a constant capacitance. Moreover, because it is known that the capacitance varies with changing force and voltage, so may the value for θ vary. A similar characterisation of the stack should take place for the force coefficient as has been done for the capacitance in order to maintain excellent accuracy. The associated complexity is too great considering that the scope of this research is to develop a functioning power harvesting concept. This detailed step is therefore left aside.

6.4.1 AC Impedance matching

A low frequency approximation of equations 2.24 is used to give an expected output of the experimental setup. Due to the asymmetrical force on the damper (section 6.3) the mean of the extrema in figure 6.3 is used: 265 N. Using the input data of table 6.1, a maximum output of 0.54 mW is anticipated with an optimal resistance of 53 kΩ. These values are only indicative, because a harmonic load is assumed which is not the case due to the non-linearity of the damper. For the experimental and simulation power output, the value is calculated by averaging the instantaneous power over n cycles with period T:

$$P = \frac{1}{nT} \int_{nT} \frac{V_p^2(t)}{R} dt \tag{6.2}$$

Figure 6.6 shows the ACIM results for varying load. Note the logarithmic R axis. Table 6.2 summarises the results for a few different approaches:

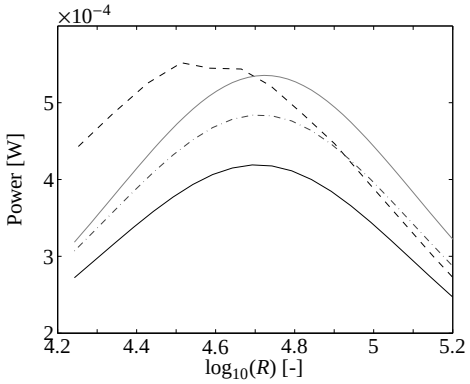

Figure 6.6: Power comparison for the ACIM damper experiment. Analytical (——), Simulation 1 (——), simulation 2 (– · – ·) and experiment (– – –).

- The analytical model uses equations 2.24. This implies a sinusoidal excitation and only the stack is considered.
- The experimental results are from the experimental setup.
- 'Sim 1' gives the results of the simulation using the polynomial approximation for the damper curve (figure 6.2).
- 'Sim 2' is a simulation of only the stack, upon which the experimentally measured force waveform is applied.

Table 6.2: ACIM results.

Parameter	Analytical	Experiment	Sim 1	Sim 2
Damper force profile	Harmonic	Real	Model	Real
RMS of force [N]	187	171	163	171
Min force [N]	-265	-256	-258	-256
Max force [N]	265	274	273	274
Optimal load R [kΩ]	53	40	50.1	50.4
Power P_{avg} [mW]	0.54	0.55	0.42	0.49
Max. V_p at R_{opt} [V]	7.6	6.3	7.1	6.5
Min. V_p at R_{opt} [V]	-7.6	-6.9	-7.3	-7.1

The explanation that the analytical power is significantly higher than that of simulation 1 lies in the RMS value of the force. The higher the RMS of the force, the higher the RMS of the voltage and the more power is dissipated. For simulation 1 the value is lower, clarifying the relatively low output. This also clarifies why simulation 1 shows poorer results than simulation 2.

Simulation 2 shows reasonable agreement with the experiment. The output is 10% lower, although the optimal load is still different. This may in part be attributed to the changing capacitance of the stack, see figure 6.5. Over most of the operating range, the capacitance in the figure is lower than the constant value used in simulation. With the optimal load inversely proportional to the capacitance, a higher optimal load is anticipated. This is reflected in the result of simulation 2 but a 20% increase in optimal load would imply a similar decrease in the capacitance (equation 2.25). The variation in stack capacitance is not so significant. A varying force coefficient θ may also cause deviations of these results, but this hypothesis has not been investigated.

One possibility that is specific to the ACIM case is the manner in which the mechanical load varies over time. In a way this is already included in the RMS value of the force, but an extreme case provides additional clarification. Consider an excitation approaching a square wave, where the force goes from minimum to maximum in a very short time t_1. Also consider that the RC_p time of the circuit is much smaller than half the period of the excitation $RC_p \ll 0.5T$. In this case the piezo element discharges completely prior to a change in force. Also, if $RC_p \gg t_1$, the element behaves as an open circuit during the voltage change, generating a much higher voltage. It can be deduced that the power output would be similar to equation 3.11 of the SECE circuit. Since the ACIM circuit has no real applicability for powering electronics, this investigation is not continued.

6.4.2 DC Impedance matching

As with ACIM, a number of different simulations are run and compared to the analytical and experimental results. An analytical approach to the output of the DCIM circuit (section 3.4) is done using a low frequency approximation of equation 3.5. This yields a maximum power of 0.37 mW at an optimal resistance of 82.9 kΩ. This resistance does not adhere to equation 3.6 for the ideal resistance which results in 86 kΩ. This is due to the high coupling of the stack.

Figure 6.7 shows the results for simulation 1 and from the experiment for the DC case. The experiment uses a rectifier model B500R [81], with an average diode drop of 0.55 V per diode. Table 6.3 shows a summary of the most important data. Again, a number of simulations have been run:

- 'Analytical' represents equation 3.5. A harmonic force is applied to the stack.
- 'Experiment' is the result from the experiment. This includes diode drops and the real damper curve.
- 'Sim 1' is a simulation with the polynomial approach to the damper curve (figure 6.2). It includes a diode drop similar to that of the B500R rectifier.
- 'Sim 2' is a simulation using the experimentally determined force waveform. It is applied to the stack only. The diode drop is accounted for. It reproduces the loads on the stack and the operation of the circuit most accurately.
- 'Sim 3' is the same as 'Sim 2' but with almost zero diode drop.

Table 6.3: DCIM results.

	Analytical	Experiment	Sim 1	Sim 2	Sim 3
Diode drop	0	0.55	0.55	0.55	0.01
Damper force profile	Harmonic	Real	Model	Real	Real
Optimal load [kΩ]	82	66	80	81	81
DC voltage at R_{opt}	5.44	4.85	4.88	4.90	5.43
Power at R_{opt}	0.34	0.35	0.27	0.28	0.35

The results are summarised in table 6.3. The optimal resistance is equal for all simulations and the analytical approach, to within a small margin of error. This again proves the claim that the DCIM circuit is insensitive to the exact load path (section 3.4). Simulations 1 and 2 match well across all aspects. To demonstrate the equality of the simulation and the analytical approach, simulation 3 is run with a diode drop of nearly zero volts. The insensitivity to the load path is again demonstrated by using the experimentally determined force curve.

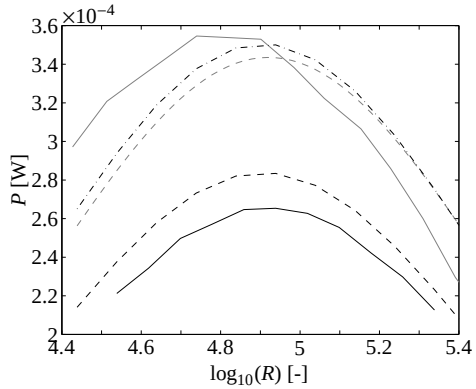

Figure 6.7: Power comparison for the DCIM damper experiment. Analytical (– – –), simulation 1, (———)simulation 2, (– – –)simulation 3 (– · – · –) and experiment (———).

As with ACIM, the experiment outperforms the simulation. The lower optimal resistance again imples an increase in capacitance as the two are inversely proportional (equation 3.6). The characterisation of the stack capacitance contradicts this, as the measured value at zero load and voltage is typically higher than most of figure 6.5.

Comparing the ACIM results with the DCIM results, the same ratio of the analytical and experimental optimal resistance arises. Due to the insensitivity of the DCIM circuit to the load path this further strengthens the idea that the piezo material itself is at fault for the change in optimal resistance: the passive operation and simplicity of both circuits exclude any unforeseen operation. Second, the maximum power figure matches quite well but is unexpected: the analytical approximation does not include the diode drop associated with the rectifier.

6.4.3 SSHI circuit

The SSHI circuit requires additional detailing before executing the experiment. The circuit must be tuned and components must be selected, see section 3.6 and appendix E for details on circuit operation. The SSHI circuit is tested twice, using two versions of the self-powered switching circuit. One uses a Bipolar Junction Transistor (BJT) as the switching component and the other uses a Field Effect Transistor (FET) (section 3.3); both will be discussed.

The maximum allowed load resistance, as indicated by equation 5.7, is derived based on the conceptual operation of the circuit. Considering the complexity of the real switching process it is prohibitively difficult to recalculate the maximum allowed resistance. There are non-linearities in the transistor voltage drops and various diodes. Trial and error in the simulation indicates that the maximum resistance for the real setup is a factor of 1.3 larger than the result of equation 5.7. Jumping ahead, this could not be confirmed in the experiments due to unexpectedly poor performance: the SSHI circuit was unable to build up voltage as high as the reverse bias. This means that the circuit can operate at the optimum resistance as calculated from equation 3.15.

NPN transistor switch

The choice of the components in the transistor switch is determined by the currents in the circuit. The maximum current through the inductor is given by $V_0 \sqrt{C_p/L}$. Given the Piezomechanik stack and a 100 mH inductor, this leads to 94 mA. At this collector current, the current gain of a BD139 NPN transistor [82] is 97, requiring a base current of just under 1 mA. Following the same reasoning for the PNP transistor, a BC560C [83] is a suitable choice with a current gain in the order of hundreds.

Following the selection of the transistors, the method explained in appendix E is employed to determine the values of the resistors and the envelope capacitor. An envelope capacitor C_e of at least 55 nF and a discharge resistor R_D of 11.2 kΩ is required (see figure E.5 for the definition of the symbols). The discharge resistor R_d is chosen as 1.8 MΩ, thereby limiting the current gain of the transistor. The achieved current gain is still sufficiently large such that the base current in the PNP transistor can be neglected in calculations.

Table 6.4: SSHI BJT parameters.

	Symbol	Value	Unit
Inductance	L_1	100	[mH]
Electrical natural frequency	ω_{el}	3.16	[krad/s]
Inductor resistance	R_L	62	[Ω]
Inductor quality at ω_{el}	Q_i	4.94	[-]
Envelope capacitance	C_e	82	[nF]
Charge resistor	R_c	27	[kΩ]
PNP base discharge resistor	R_d	1.8	[MΩ]
NPN base discharge resistor	R_D	12	[kΩ]
NPN current ratio I_{max}	h_{FE}	93	[-]
PNP current ratio (R limited)	h_{FE}	150	[-]

Table 6.4 summarises the settings for the BJT based switching circuit. The capacitance and resistances listed are calculated for a current gain of 80, implying a significant margin of safety for the NPN transistor.

Only introductory experiments were conducted with the BJT due to poor performance. This was caused by the combination of the BJT and the inductor. As the voltage amplitude increased the inversion waveforms became distorted, indicating a non-linearity in the coil (which is confirmed in section 6.5). This led to larger currents than expected, putting the transistor in the on-state while saturation is desired. A measurement of the voltage during the inversion process is shown in figure 6.8, showing the irregular inversion waveform. A sine wave is expected.

The non-linear behaviour of the core can be due to eddy currents in the core or hysteretic losses due to geometrical expansion and contraction of the core under influence of the magnetic field [84]. As already anticipated in section 5.3, the cored inductors indeed cause excessive losses.

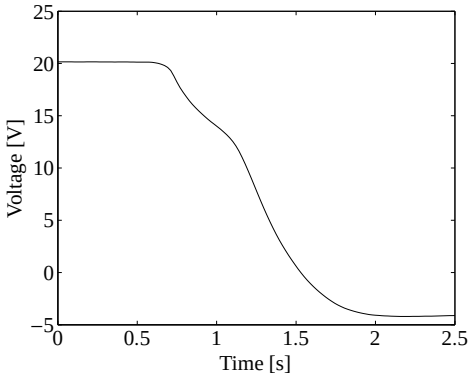

Figure 6.8: The piezo voltage during inversion for L =100 mH.

The circuit can also be designed with a 1 mH air core coil, but this leads to a significant increase in energy consumption by the switch. This is related directly to the transistor current gain ratio and the envelope capacitor size that is subsequently required. The stored energy in a capacitor equals $CV^2/2$. The higher the switched current capability of a transistor, the lower the current gain. Small signal transistors such as the BC560C [83] used here possess a current ratio h_{FE} in the hundreds and switch in the order of ten milliamps. The BD139 [82] switches up to an Ampère but the gain reduces to 50 at that current.

A switched current of 1 A therefore leads to a required envelope capacitance of 10-20 % of the piezo capacitance. Failure to do so will lead to blockage of the transistor as the switched current increases. Diode drops and various transistor effects marginally increase the envelope capacitance further, penalising the net power output of the harvester.

MOSFET based switch

A second variation of the self-powered switch involves the use of a MOSFET instead of the NPN transistor. As discussed in section 3.3, the MOSFET is a switch which uses a voltage

to control the switching action. In the absence of any current the power consumption ideally is zero, but in reality there is still a finite but large gate-source resistance (7-8 orders of magnitude) [53]. The penalty associated with the FET based circuit is that the switch does not begin to close until a certain voltage is built up at the gate. This is typically a few volts, whereas a transistor will go into conduction as soon as the diode drop is overcome.

In the FET circuit, once the PNP transistor goes into conduction, voltage builds up at the gate of the FET. Because of the gate-source capacitance and the threshold voltage $V_{GS(on)}$, the circuit must be tuned to expediate this process. There are also parasitic capacitances which must all be charged, delaying the build-up of the gate voltage. The gate-source resistor of the circuit is now chosen in the same order of magnitude as the PNP base resistor, so that this process occurs as quickly as possible.

Using the nomenclature of figure E.9, table 6.5 gives the circuit parameters. The stated quality factor includes the on resistance of the MOSFET. Also note that the discharge resistors are now identical. Considering that the combined RC_e time of the circuit is already much higher than that of the NPN based switch, the lower PNP base resistance is not a critical issue.

The MOSFET being used is a model 2N7000 [85]. This type has a comparatively low threshold voltage and sufficient current handling capability for the circuit. Most circuit parameters have been tested using simulations and component datasheets prior to experimenting. The stated inductor quality includes the resistance penalty incurred through the FET. It is a physically larger cored inductor but with a lower inductance value and significantly lower resistance.

Table 6.5: SSHI FET parameters.

	Symbol	Value	Unit
Inductance	L_1	10	[mH]
Electrical natural frequency	ω_{el}	10	[krad/s]
Inductor resistance	R_L	0.4	[Ω]
FET Drain source resistance	$R_{DS(on)}$	1.5	Ω
Inductor quality at ω_{el}	Q_i	53	[-]
Envelope capacitance	C_e	22	[nF]
Charge resistor	R_c	27	[kΩ]
PNP base discharge resistor	R_d	470	[kΩ]
FET gate discharge resistor	R_D	470	[kΩ]
FET gate threshold voltage	$V_{GS(th)}$	2.0	[V]
PNP current ratio (R limited)	h_{FE}	1	[-]

Four different sets of results are presented:

- The ‘Analytical’ results are from equation 3.14, using the component values given in table 6.5.
- ‘Experiment’ gives the results from experiment.
- ‘Sim 1’ is from the simulation using the values from table 6.5.

- 'Sim 2' is from simulation. It uses the same values as simulation 1, except that the coil resistance is increased so that the quality of the coil $Q_i = 1.6$.

Figure 6.9 shows the power as a function of load resistance. It shows both Simulink results, one is voltage limited as it enters the cross-hatched region (which represents too high a stack voltage) and the other is operating at the optimal resistance. The analytical result extends beyond the bounds of the plot, and is voltage limited as indicated in table 6.6. Contrary to the ACIM and DCIM circuits, the SSHI performs significantly poorer than the ideal simulation (sim 1).

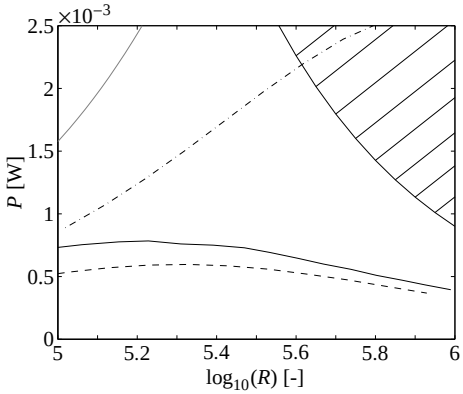

Figure 6.9: Power comparison for the SSHI damper experiment. Analytical result (——), experimental (——), simulation 1 (– · – ·) and simulation 2 (– – –). The cross-hatched region indicates the where the stack voltage exceeds the maximum allowed reverse field. The analytical data is only shown partially to maintain resolution of lesser results, see table 6.6.

The poor performance appears to be, for a large part, due to the coil (this will be confirmed in section 6.5). Figure 6.10 shows the inversion efficiency from experiment for an inversion event for each load resistance value. The inversion quality is based purely on the inversion process itself when the FET is conducting. Due to the poor inductor quality a second result is shown in 6.9, which is acquired using $Q_i = 1.6$. This yields an inversion efficiency which is similar to that determined from experiment at the optimal resistance, despite the real component exhibiting non-linear effects.

The main findings are summarised in table 6.6. The difference between the analytical approach ($Q_i = 53$) and simulation 1, which uses the same inductor quality, is due to the analytical approach neglecting the switching circuitry. Consider, for example, the voltage loss from the maximum prior to inversion and the diode in the oscillator loop. However, the difference is too large to explain using linear components. Simulation 1 is also limited by the maximum voltage of the stack. Simulation 2, surprisingly, shows the same trends as the ACIM and DCIM results. The optimal resistance is nearly 20% lower, and the optimal power is nearly one quarter higher than simulation. Due to the use of the rectifier the SSHI output is also independent of the load path, provided it is cyclic with no local extrema that could trigger the envelope detectors.

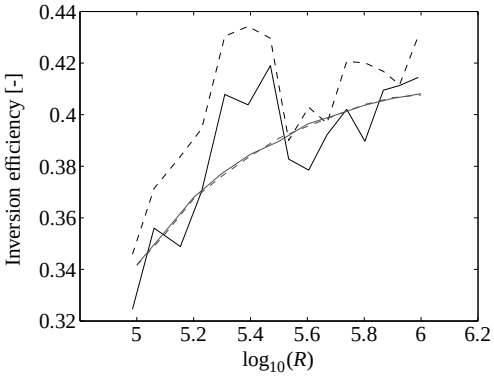

Figure 6.10: Inversion efficiency for the lag damper experiment. Experimental data from positive to negative (– – –) and negative to positive (———). Simulation data from positive to negative (– – –) and negative to positive (———).

Table 6.6: SSHI results.

	Analytical	Experiment	Sim 1	Sim 2
Coil resistance R_L [Ω]	1.9	-	1.9	64
Quality factor Q_i	53	1.6	53	1.6
Optimal load [kΩ]	234	278	416	213
Power at R_{opt} [mW]	3.2	0.78	2.2	0.6
DC voltage at R_{opt} [V]	30	11.5	30	11.3

6.4.4 Discussion

Considering the modelling assumptions of a constant capacitance C_p and force coefficient θ the simulations for the ACIM and DCIM circuits show consistent results. Since the circuitry is passive (aside from the diodes) there is little room for uncertainty in the simulations. Given that the force applied to the stack is measured as well, the only cause of the mismatch of results can lie within the stack. The change in capacitance for varying electrical and mechanical loads has been measured, but the observed variation is not sufficient to account for the difference between simulation and experiment. Characterising the complete piezoelectric performance of the stack is far more elaborate and beyond the scope of the research objectives.

The Piezomechanik stack which is used is poorly documented in terms of electromechanical properties and only a few material properties are available. This is circumvented by characterising the stack as a whole, but the stack performance was significantly less than what could be expected from the available material properties and when compared to other similar piezo ceramics. However, the lack of documentation means that pinpointing the cause becomes impossible without performing a full characterisation of all the properties.

Also, the issue of the poor coupling of the stack remains. This was only realised after the measurements, when calculating the stack properties. The cause is unclear. The stack

was first repolarised using a DC voltage of 150 V to maximise the piezoelectric coupling. The ACIM and DCIM circuits were tested first and are incapable of generating an excessive negative voltage. This excludes the possibility of accidental overload were the SSHI circuit tested first.

Aside from the uncertainty between material data and stack performance, it has already been concluded that the ACIM and DCIM simulation results show reasonable agreement with the experimental results, showing that the simulations are a step in the right direction towards developing a lag damper harvester. With the models validated, improvement must be made in the implementation of the advanced circuitry and better materials.

The SSHI circuit setup did not perform as well as anticipated. The probable cause is the non-linearity of the inductors which were used. The important conclusion here is that air core inductors are a necessity. Given that the SSHI circuit is considered the best choice for a lag damper harvester (section 5.4), more investigation is required towards developing a functioning SSHI circuit in combination with this stack, which is done in the remainder of this chapter.

6.5 Additional SSHI circuit investigation

Using only the electrical portion of the lag damper setup, the circuit was investigated in more detail. The circuits are mostly built up on a *breadboard*, a panel with interconnected sockets into which the components can be inserted. The stack is still connected electrically, but only functions as a capacitor. A current source is used to generate the current which normally results from straining the piezo material. Various settings and inductance values are investigated in order to assess the linearity of the inductors. Data is acquired using a Tektronix TDS2004B oscilloscope with USB support.

The schematic and associated waveforms of this circuit are shown in figure 6.11. The current source is constructed using a voltage source, a transformer which increases the voltage by a factor of approximately 10 and a resistor R_T which is relatively high compared to the

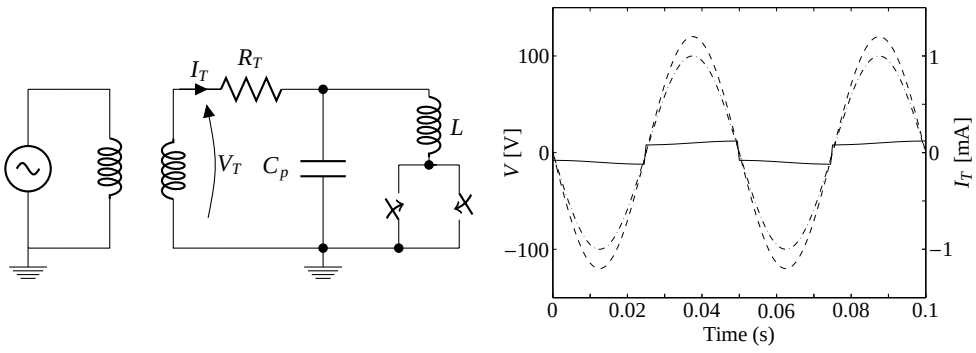

(a) Testing circuit schematic

(b) V_p (——), V_T (– – –), and I_T (– · – · –)

Figure 6.11: Schematic and waveforms of the SSHI testing circuit.

dynamic impedance of the stack. The resistor R_T, combined with the high voltage generated in the transformer, generates a nearly sinusoidal current through R_T. This current is virtually unaffected by what is happening in the LC_p loop.

Four coils are tested of which the data is summarised in table 6.7 and an image is provided in figure 6.12. The 100 mH coil is the same as what was used in the full setup with the BJT (section 6.4). The 10 mH coil is the same as what was used for the FET circuit in the setup with the damper. The 1 mH coil is a coil around a plastic core. This is very similar to an air core. Recall that the lag damper harvester requires as high an inductance as possible (section 5.3). The 1 mH coil is therefore not suitable for the experimental setup, but being an air core, it is more linear and may prove the claim that the ferrite core inductors are detrimental to the inversion performance. The last inductor, which is only tested with the MOSFET setup, is a large one which is manufactured locally. It is a circular multilayer air core with a diameter of 12 cm and 0.6 kilograms of 1 millimetre diameter wire. It represents an attempt to make the best possible applicable core for the lag damper setup. The circuit construction row indicates whether the circuit was tested using only breadboard construction, or if the oscillator loop is fully soldered. The latter is expected to yield better performance due to the addition of parasitic resistance in the breadboard.

Table 6.7: Coil data for the coils investigated in the electrical setup (exact permittivities unknown).

Inductance [mH]	1	6.7	10	100
Core	Plastic	Air	Ferrite	Ferrite
Relative permittivity order of magnitude	1	1	1000	1000
Circuit construction	BB and soldered	soldered	BB	BB
Natural frequency with C_p [krad/s]	31.6	12.2	10	3.16
Coil resistance R_L [Ω]	1.7	1.3	0.4	64
Inductor quality at ω_n	21	63	250	4.94

Figure 6.12: The coils used in the experment. From left to right: 6.7 mH, 10 mH, 1 mH and 100 mH.

The stated quality factor is that of the coil alone. In the circuit, additional diode drops and the finite resistance of, for example, the FET will decrease this value. The maximum piezo

voltage attained is in the range of 10-15 V, depending on the particulars of the circuit under investigation.

In assessing the cause of why the SSHI experiment performs poorer than simulation, the inversion process must be analysed in more detail. The switching delay, inductor quality and the diode drop must be included in the whole of the calculation. Lastly, following inversion, the envelope capacitor of the opposite switch is charged. With its R_cC_e time being much smaller than the period of the excitation an additional voltage drop of the stack will occur, as will be shown in the results.

Figure 6.13 shows the voltage inversion process in detail. The peak voltage is denoted V_0. Three more voltage values are indicated. These are defined and calculated as follows:

1. The switching delay following the maximum voltage manifests itself due to the diode drops of the circuit. The stack voltage must decrease in value identical to the sum of the PNP diode drop, and the discharge diode drop. With the components used in the circuit this threshold voltage V_{th} is approximately 0.9 V. The voltage at the onset of the actual inversion is thus: $V_1 = V_0 - V_{th}$.

2. The starting voltage of the inversion process is V_1. The voltage after inversion and the inductor quality have been addressed in detail in section 3.6. Equation 3.13b must me modified to include the effect of the diode in the switching circuit.

   The diode drop V_d in the capacitor-inductor loop is analogous to the effect of *Coulomb friction* on a mass-spring system in the mechanical domain [58]. Recall the analogues given in section 3.2. The mechanical analog to this system is a mass, spring, viscous damper and coulomb friction. Solving the differential equation of the electrical domain and evaluating it after half an oscillation yields:

$$V_2 = -(V_1 - V_d)\, e^{-\pi/(2Q_i)} + V_d \tag{6.3}$$

3. Assuming the worst-case scenario, the envelope capacitor of the inactive switch must be charged from the starting voltage $V_0 - V_d$ prior to inversion (note that there is a diode in the charging circuit). The charge is taken from the stack after inversion. The final voltage is calculated based on charge conservation between the two capacitors. In reality, and in particular when the R_cC_e time is short compared to the inversion time, this process will occur simultaneously to inversion. The result from step 3 is therefore not exact. The final voltage after charging the opposite envelope capacitor is V_3.

$$V_3 = \frac{C_pV_2 + C_e(-V_0 + V_d)}{C_p + C_e} \tag{6.4}$$

With the stack outside of the lag damper setup the influence of the mechanical domain can be ignored under normal operation: the mechanical eigenfrequency is 30 kHz (Piezomechanik specification) and the electrical eigenfrequency is 5 kHz for the 1 mH inductor. The larger inductances lead to lower electrical natural frequencies.

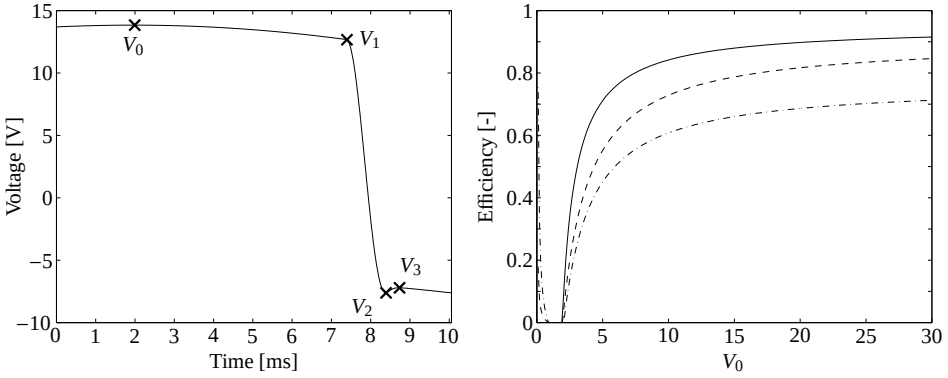

(a) Simulation result of the inversion process, 100 mH coil. V_0 = 13.8 V

(b) Analytical inversion efficiency for the 6.7 mH coil. $-V_2/V_1$ (———), $-V_3/V_0$ for FET (– – –) and $-V_3/V_0$ for BJT (– · – ·)

Figure 6.13: Voltage inversion details.

6.5.1 BJT based switch

The BJT switch requires recalculation for each inductance value as the current ratio determines the operation of the transistors. This is done according to the calculation of appendix E. The circuit parameters are given in table 6.8. Figure 6.14 shows the results for the positive to negative inversion.

Table 6.8: BJT circuit parameters.

Inductance [mH]	1	10	100
Charge resistor R_c [kΩ]		22	
Envelope capacitor C_e [nF]		62	
Discharge resistor R_D [kΩ]	1	3.3	10
PNP base resistor R_d [MΩ]	0.15	0.39	1.5

The efficiencies are presented in table 6.9. Value η is the efficiency for various situations. Superscript *eqn* refers to the analytical equations, and *exp* indicates the experimental value. Two efficiences are given: subscript *inv* is the efficiency of only the inversion process (V_2/V_1) and *tot* gives the total efficiency of the entire process: (V_3/V_0). The results from the analytical approach are evaluated using the value of the maximum voltage column, which is measured from the experiment. Column R_{bb} is an added parasitic resistance which will be elaborated on with the respective result.

The experimental data for the 1 mH coil is acquired using only a breadboard circuit, a soldered circuit has not been built. The exact parasitic resistance from the breadboard is not known. This coil performs the best, although the transistor is used close to its operating limit. This is signified by an increase in the collector-emitter voltage as the inductor current approaches the maximum value. At 0.5 A the BD139 transistor current gain is 80, which was

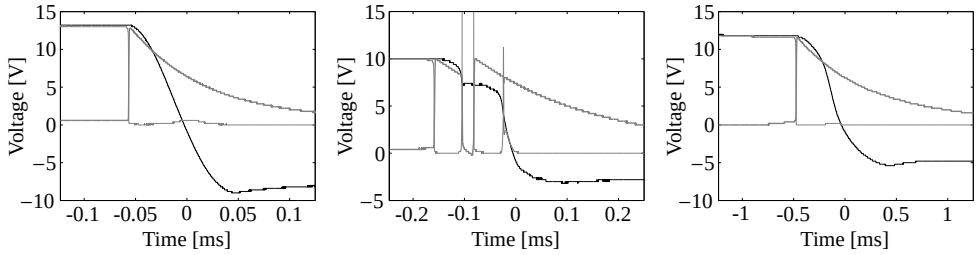

(a) 1mH inversion (b) 10mH inversion (c) 100mH inversion

Figure 6.14: BJT circuit results for the positive to negative inversion V_p (——), V_e (——) and V_{CE} (– – –).

Table 6.9: Inversion performance for the BJT switch.

Inductance [mH]	V_0	R_{bb}	η_{inv}^{eqn}	η_{inv}^{exp}	η_{tot}^{eqn}	η_{tot}^{exp}
1	13.8	0	0.85	0.68	0.63	0.52
		1.8	0.71		0.55	
10	10.4	0	0.89	-	0.65	0.25
100	12.2	0	0.66	0.46	0.50	0.39

used in dimensioning the resistors and envelope capacitor. Considering the lower operating voltage in this setup, compared to the damper test, this circuit would not operate correctly with the higher piezo voltage and resulting current in the damper setup. The experimental result closely resembles a sine wave, indicating good linearity of the components.

The second set of analytical results for the 1 mH inductor relate to the use of the breadboard. A breadboard can induce a parasitic resistance (R_{bb}) of up to a tenth of an Ohm for each connection. In this setup 18 connections are used in the LC_p loop, implying a total added resistance of up to 1.8 Ω. This value must be compared to the 1.7 Ω resistance of the 1 mH coil, and an equivalent resistance of the NPN transistor of approximately 1.5 Ω (which is derived from the experimental data). The equivalent resistance of the NPN transistor was not reproduced in the simulation due to the simplified models using Simscape. The parasitic resistance R_{bb} is clearly significant compared against the others within the loop. In reality, the total resistance of the oscillator loop can be anywhere between 3 to 5 Ω. Using the upper bound, the calculated inversion efficiencies closely match those from the experiment, although no experiment of a soldered circuit has been performed for the BJT switch.

The 10 mH coil performs the poorest as the circuit cannot function properly. The nonlinearity of the core material is so significant that it leads to a number of unexpected effects. First is blockage of the transistor. The result shows a peak current high enough to bring the NPN transistor out of saturation. The increase in the NPN base-emitter voltage, combined with the coil trying to maintain the current, progressively blocks the transistor. This is signified by the spike in the collector-emitter voltage. Interestingly, the current from the coil then goes to the envelope capacitor, charging it again. The envelope capacitor can

then again provide sufficient current to allow the NPN transistor to conduct a second time. In figure 6.14(b), at t=-25 μs the transistor nearly goes out of saturation again. A second effect is a delay in conduction through the inductor, once the switch has closed. Note how at $t \approx -0.15$ ms the collector-emitter voltage goes to zero, indicating that the switch is closed. The piezo voltage remains around 10 volts for a brief moment before changing. Compare this to the case of 1 mH where the inversion commences almost immediately.

The 100 mH coil performs in between both. Although the inversion process is completed without blockage of the transistors, the voltage curve is not purely sinusoidal. This indicates a mild non-linear effect of the ferrite core. In the damper experiments this effect was more profound (see figure 6.8) due to the higher stack voltage and the resulting inversion current. The performance is much less than expected.

Only one set of analytical results showed reasonable agreement with experiment. The reason for the cored inductors has been explained. For the 1 mH inductor the varying current gain ratio and the variation of the diode drop (1N5819 diode), which cannot be modelled in Simulink, are contributing factors. The use of a breadboard leads to uncertainty concerning the resistance of the oscillator loop. However, it has been demonstrated that the experimental results can be reproduced with realistic input values.

6.5.2 FET based switch

The FET switch does not require recalculation of the parameters for each coil. It is calculated once for the highest inductance value since this has the longest duration requirement for the gate-source voltage of the FET. The envelope capacitor is 22 nF, the charge resistor R_c is 68 kΩ, and the discharge resistors R_D and R_d are 4.7 MΩ and 470 kΩ, respectively. The main results are shown in figure 6.15 and the resulting efficiencies are listed in table 6.10.

Table 6.10: Inversion performance for the FET switch.

Inductance	V_0	R_{bb}	η_{inv}^{eqn}	η_{inv}^{exp}	η_{tot}^{eqn}	η_{tot}^{exp}
1	14.6	1.8	0.72	0.68	0.64	0.53
	13.8	0	0.78	0.68	0.70	0.55
6.7	15.8		0.88	0.75	0.79	0.65
10	11.4		0.88	0.40	0.77	0.33
100	12.4		0.65	0.45	0.57	0.4

Contrary to the BJT case, the FET has no difficulty passing the 0.5 A current associated with the 1 mH coil. This is evidenced by the drain-source voltage increasing to only 0.4 V for the FET (starting from 14.6 V) and the BJT V_{CE} increasing to 0.6 V, with a starting voltage of 13.8 V for the breadboarded circuit. The performance again falls short of what is expected analytically.

Two cases are presented for the 1 mH inductor. Contrary to the BJT circuit, both a soldered and breadboarded circuit are tested with the FET. The first row contains the breadboarded circuit data. The results fall short of the expected performance. Due to the low resistance of the coil and the high currents involved, a second soldered circuit is produced and tested. These results make up the second row of the 1 mH results. The lower V_0 is attributed

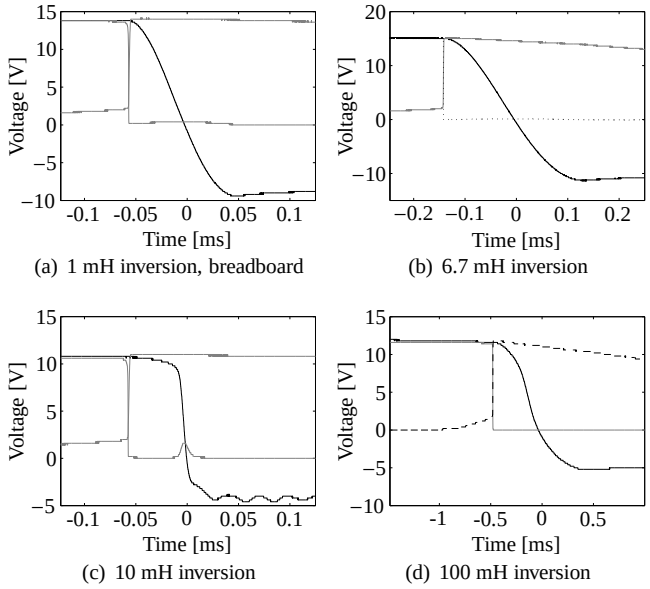

Figure 6.15: MOSFET circuit results for the positive to negative inversion. V_p (——), V_{GS} (– – –) and V_{DS} (——).

to a different setting of the transformer used to increase the signal generator voltage. The inversion itself shows a nearly identical performance, ruling out any significant breadboard losses in the experimental setup.

The overall performance of the soldered circuit is marginally better. It must be taken into account that, considering the resolution of the oscilloscope at the required voltage range (0.2 V), the efficiency can be calculated to within approximately 1.3%. Although this resolution is relatively poor, it is sufficient to establish whether or not the upper bound of the assumed parasitic resistance of 1.8 Ω is realistic. This does not seem to be the case. The experiment shows a more significant decrease in voltage following inversion than the analytical case implies. This can not be attributed to the envelope capacitor as the decrease is too large. The cause is unclear.

The locally made 6.7 mH coil functions the best and the results are acquired using a soldered circuit. It also does not achieve the performance predicted by equations 6.3 and 6.4. It also supports the requirement for an air core. Not shown in the figures is an oscillation of the opposite V_{GS} following inversion, the respective frequency is 111 kHz. With the switch being open, this is attributed to the self-resonant frequency of the coil, caused by the self-capacitance of the coil. Based on the measurements, the self-capacitance of the inductor is approximately 300 pF. This effect may cause some losses but these have not been quantified.

The 10 mH coil again performs the poorest. Contrary to the BJT switch, there are no problems with the FET passing the high current resulting from the non-linear behaviour of the coil. The current can be calculated from the slope of the voltage curve of the stack in figure

6.15(b), in this case it is over one Ampère. Recall the fundamental capacitor equation from section 3.2. In the linear case the current is 0.12 A, assuming the same voltage at the onset of inversion. The voltage change occurs so quickly that the mechanical natural frequency of the stack is excited, signified by the 30 kHz oscillation following voltage inversion. The non-linearity of the core is also evident at the start of the inversion process. The voltage remains relatively unchanged for 50 μs after the gate voltage is brought up to the full on-state, whereas the air cores starts immediately.

The 100 mH inductor performs less than is expected based on simulations. Upon close inspection of the waveforms, the piezo voltage does not accurately describe a sine wave. The non-linearity of the inductor is detrimental to the performance.

6.5.3 Discussion

Summarising the results, a number of difficulties have been identified. First is the use of cored inductors. Any non-linearity introduced by the core material is detrimental to inversion performance. The use of air-core inductors is a necessity.

Second is the choice of the BJT or FET based circuit. Considering the peak currents associated with the piezoelectric stack, the BJT is out of the question. Higher current requirements lead to a lower current-gain and in turn to a larger envelope capacitor. The use of a FET is necessary in order to build an efficient SSHI circuit for the lag damper concept. The low envelope capacitance required in the FET based circuit increases output over the BJT and the circuit also does not require as much fine-tuning as the BJT variant.

The third issue relates to the construction of the circuits. A breadboard was used, which is a platform with interconnected contacts. A circuit is built simply by inserting the components into the contacts. These contacts introduce parasitic resistances up to a tenth of an Ohm per connection. It should be noted that it is difficult to measure the parasitic resistance of the breadboard because it may change from contact to contact, and even shifting the components may influence this resistance. A simulation including an assumed parasitic resistance showed good agreement with the experimental results. However, in the FET experiments, comparing a soldered and breadboarded circuit, the improvement was not so significant as anticipated.

Both variations of the switching circuit possess a number of resistors which are all in the kΩ range or more, so that the parasitic resistance does not interfere with the switch. For the capacitor-inductor loop, the total resistance must be minimised. Non-linear effects set aside, the 100 mH coil does not suffer significantly due to its internal resistance of 62 Ω. The 10 mH and 1 mH inductors have a resistance in the order of 1 Ω, here the parasitic resistances accumulate and can represent 30-40% of the loop's total resistance. For proper experimentation this loop must be soldered and high quality BNC connectors should be used to connect the stack. This will limit the resistance of the loop to that of the internal resistance of the constituent components.

Using a linear inductor and inclusion of the parasitic resistance in the simulation, reasonable agreement was found between experiments and the simulation. However, a mismatch remains of which the cause is unclear. Considering the efforts which were undertaken to reduce the error (a large inductance air core and a soldered circuit), it is concluded that the causes are beyond the scope of this thesis and reside strictly within the electromechanical or material mechanics field.

6.6 Conclusions

This chapter presents comparisons between experiments and simulations which have been performed in order to validate the numerical models of chapter 5. A setup using a damper is designed and built. Two passive circuits (ACIM, DCIM) and one active circuit (SSHI) have been tested.

The non-linearity of the stack caused significant difficulties. The capacitance has been measured for a range of voltages and mechanical loads, and shows a variation of up to 15% when compared to the 0 V / 0 N situation. It is therefore conceivable that the piezoelectric force coefficient θ also varies. With the wide range of mechanical and electrical loads, a complex characterisation would be necessary in order to accurately match simulation and experiment. This characterisation has not been done. It is beyond the scope of this research.

The passive circuits (ACIM and DCIM) show reasonable agreement with simulation and analytical approximations. Despite the linear approximation of the stack, the differences in characteristic values remained within 20%, with the experiment typically outperforming the simulation. The optimal load of the circuits is smaller than what can be anticipated from the capacitance of the stack. This is the opposite of can be expected based on the characterisation of the stack capacitance, which is typically smaller than the unloaded capacitance. The observed difference could not be clarified fully. Despite these differences, the same trends are noticed, generating confidence in the models.

The active SSHI circuit validation was only partially successful. The experimental output was less than half of the output indicated by the simulation. One cause was the use of cored inductors where non-linear effects decrease the inversion quality. Rerunning the simulation, using the inversion quality from experiment, revealed similar trends as observed with the two impedance matching circuits. The experimental output is higher and the optimal resistance is lower.

Further investigation of the circuit was performed outside of the lag damper setup. The first conclusion here is that the cored inductors indeed proved non-linear. Second, the use of a breadboard in the setup introduced an extra parasitic resistance of a few Ohms in the capacitor-inductor loop. For the air core and one of the ferrite core inductors this added resistance presented a significant additional penalty. Assuming a realistic value for the total parasitic resistance and with an air core inductor in the setup, the results for the circuit simulation are in good agreement with the experimental results in this chapter. This generates confidence that the simulation can be used to model the setup, provided that linear components are used.

The SSHI circuit functioned correctly, but an efficient implementation (achieving 70% voltage inversion) has not been presented in this thesis. The causes have been identified and sufficient improvement is possible to achieve this value. Using the electrical setup, a custom air core inductor and proper circuit construction techniques led to better performance. With this result, it can be concluded that the simulation models for the SSHI circuit are reliable and are a good representation of reality.

Chapter 7

Conclusions and recommendations

7.1 Conclusions

The conclusions are discussed based on the list of research goals presented in chapter 1.

Develop a fundamental understanding of power harvesting. Chapters 1, 2 and 3 provide a comprehensive overview of the basics of power harvesting. While these basics are not new, more detailed modelling and consideration of the electromechanical coupling effects has led to more knowledge concerning effects which may occur due to high coupling.

By addressing the mechanical and electrical domain simultaneously, a number of effects of the high coupling have been explored. Most interesting is the effects that active circuits may have on the mechanical domain (sections 5.3 and 6.4). In low coupled systems such as harvester beams, there are few limitations with respect to how quickly the circuit may influence the voltage of the piezo element. Due to the low coupling this will not lead to undesired behaviour in the mechanical domain. On the other hand, the work presented in this thesis demonstrates that highly coupled systems will experience significant vibrations and loss of output if these processes are executed too quickly.

In line with the previous point and more fundamental is the combined approach of both domains. Often the literature starts with a harvesting system to finally only focus on the mechanical or electrical aspects, trying to optimise either of the two. It is to some extent understandable as mechanical and electrical engineering are separate fields, but considering both is necessary to develop an application. A one-sided approach excludes the discovery of combined effects, addressing multiple domains becomes more crucial in developing and optimising harvesting systems as the coupling increases.

Explore the potential for power harvesting in the rotor of a helicopter. In this thesis two concepts have been developed. The first concept is the placement of patches within a rotor blade (chapter 4). A tool has been developed which optimises patch placement within a slender low coupled beam-like structure.

Although not included in this work, the tool can be developed further to include highly coupled structures, executing an iterative calculation in order to converge to an optimum patch

distribution. The complete in-blade patch concept developed in chapter 4 is too complex a system to simulate due to the structural dynamics and aerodynamics and the aeroelastic coupling. However, simpler systems can be modelled in their entirety. For highly coupled structures, with the aid of an iterative calculation scheme, an optimum location can then be found based on the actual excitation.

From the power harvesting point of view this concept is applicable. The blade is a flexible structure and undergoes large strains during flight. Power can be harvested within centimetres of a location where power is required for sensing, making it a distributed concept.

The drawbacks mainly involve the mechanical implications. First is the addition of weight in a rotor blade. This leads to increased centrifugal forces, blade loads and modifies the dynamics of the blade. The second concerns the aeromechanical properties of the rotorcraft and in particular a phenomenon known as autorotation. Power can be safely harvested in the blade, but the potential is decreased due to the autorotation requirements. This requires that the centre of mass of the aerofoil is located ahead of the aerodynamic centre. Realistically, this means piezo material can only be added when it is located closer to the leading edge than the trailing edge. The patches that are located between the quarter and half chord points can be balanced by the patches ahead of the quarter chord point, maintaining the required balance.

The complexity associated with optimising each patch, analysing many flight profiles and dynamic considerations, makes this concept difficult to develop further. Analysing additional flight profiles also decreases the expected output because the number of feasible patch locations will decrease.

The second concept consists of modifying the lag damper to accommodate a stack of piezo material. This makes it a centralised concept: power is generated in only one location but in a larger quantity. The unique aspect of this idea is the application of a stack which is typically not suited for power harvesting. Combined with the simplicity of a single reliable excitation from the damper, this concept can be investigated using basic analytical equations. This concept is explained further in light of the next research goal.

Modelling, simulation and optimisation of a power harvesting device for use in a helicopter rotor. The lag damper concept was chosen to be developed in more detail. A simplified model was developed for simulation purposes (section 5.2). Despite neglecting seemingly significant aspects such as aerodynamics and blade flexibility, the behaviour of the damper was mostly preserved.

Various electrical circuits were simulated (chapter 3 and section 5.3). These simulations provided further insight into the behaviour and output of such a system. For each circuit a power output was established and important design choices were identified. The active circuits led to a number of difficulties such as introducing undesired vibrations back into the mechanical domain and imposed strict requirements on the properties of the electrical components. Through careful design all of these aspects can be addressed.

Upon optimising the mechanical and electrical design for each circuit the output, flexibility and technological readiness of each could be established. The passive Direct Current Impedance Matching circuit can be implemented without any further research as all the aspects have been researched either in this thesis or in the literature. Of the active circuits the Synchronous Electric Charge Extraction (SECE) can be used which offers 50%

more power, but at the cost of extensive electrical infrastructure in order to actually achieve this higher output.

The Synchronised Switch Harvesting on Inductor (SSHI) circuit is by far the most promising circuit. As with the SECE circuit it achieves higher output by switching the voltage of the stack. By modelling this process in more detail design rules are formulated which will help prevent undesired vibrations and will minimise losses. Using the lag damper defined in the Green RotorCraft project a figure of 5-7 Watts of power can be harvested per damper with the SSHI circuit, depending on the ambient conditions.

Experimental validation of the proposed concept and performed simulations. A laboratory scale setup is built and used to validate the simulation models developed previously. The linearity of the piezo material used in the setup caused difficulty in matching the simulation with the setup. With the simplicity of the passive circuits in mind, the stack represented the only uncertain factor. A capacitance measurement of the stack revealed significant variation for varying force and voltage, demonstrating that excellent agreement would not be achieved. A similar characterisation of the piezoelectric force factor was not performed since detailed material characterisation is beyond the main scope of this reserach.

The two passive circuits were validated first. Despite the variation in the piezo material properties, similar trends are discovered for both circuits. This further affirms that the stack is the uncertain factor because the simplicity of the circuits cause no uncertainties. The predicted output of the circuits was exceeded by approximately 20% in the experiments. The optimal resistance associated with both circuits also shows a consistent error with the experiment being around 25% more than simulation. This difference is significant as it is contrary to what could be expected from the variation in piezo capacitance.

The SSHI circuit is also tested, but in the complete setup validation is initially unsuccesful. Using a separate electrical setup the circuit is investigated further. The design of the switching circuit of the SSHI circuit is modified in order to cope with the high currents associated with switching the voltage of the stack. The modification is tested succesfully and can cope with currents up to a number of Ampères. Various inductors are also investigated. The prediction that ferrite-core coils could present problems was confirmed. Air coils show far superior performance at the cost of a physically larger and heavier component.

Combining the results of the simulations, the mechanical setup and the electrical setup, all necessary steps have been taken to design a working concept. The resulting design guidelines and insights can be used in subsequent projects to quickly and efficiently develop harvester concepts.

Application development. The final research goal is partially met. Concerning the lag damper, a great deal of research has been done towards a full-scale lag damper harvester (chapters 5 and 6). Design guidelines have been established, models have been developed and experimental work has been performed which generates confidence in the work. What remains prior to a full-scale implementation is a final experiment which combines the best components, from stack to circuitry and mechanical integration of a stack in to the lag damper.

Within the University of Twente other projects [46, 47] have been undertaken as well in cooperation with the engineering firm Tauw. An important conclusion that can be drawn

from these projects is that accurately predicting the output of a harvesting system requires, first and foremost, detailed knowledge of the excitation and all damping sources. For low coupled systems, knowledge of the displacement or deformation of the source is sufficient. For highly coupled systems knowledge of the excitation, the structure under consideration and the geometry and dynamics of the harvesting component are necessary.

7.2 Recommendations

Significant steps have been taken towards the development and realisation of a power harvesting system intended for use in the rotor of a helicopter. A number of follow-up research options are presented here.

- Research into material which demonstrates more predictable behaviour. The material used in the experimental work (chapter 6) displayed significant non-linear effects, thereby reducing the accuracy of the conducted simulations. For the lag damper simulations the best performing material from PICeramic was selected. Testing a sample of this material under the intended stresses and voltage fields will help in further establishing the accuracy of the full-scale simulations.

- Following the investigation into more linear material, the experiments presented in chapter 6 should be repeated with a stack of the chosen ceramic. Combined with the knowledge of a full characterisation of the material under consideration better agreement should be found between simulation and experiment.

- Full-scale realisation of a power harvesting lag damper is the final step in developing a prototype lag damper harvester. The stack must be integrated in the damper and tested.

- Development of a design tool which translates a given base excitation to a power figure. Examples [46, 47] show that good engineering judgement is insufficient in developing a power harvesting system. Such a tool should encompass the dynamic data of the vibration source and also a means to quantify the power which can be harvested from it. Since a power figure is fully dependent on the size of the intended harvester, dimensioning of the beam is required.

  For large structures, of which it is clear that the harvester will be uncoupled, the calculation is straightforward. Measuring the base excitation and modelling a beam or harvester element will suffice. For potentially high coupled systems the system must be analysed as a whole. The dynamics of the structure must be considered in combination with the harvester itself, optimising the combination for maximum output.

Nomenclature

Latin symbols

A	Area [m^2]
C	Capacitance [F]
$\mathbf{C}^D, \mathbf{C}^E$	Piezoelectric compliance matrix at constant electrical displacement or voltage field [N/m^2]
C_e	Envelope capacitance in SSHI switch [F]
C_p	Piezo element capacitance [F]
c	Blade chord length [m]
c, c_s	Damping coefficient (of the structure) [Ns/m]
D	Electric charge density [C/m^2]
$\mathbf{d}$	Piezoelectric charge constant [m/V]
E, E_{33}	Bulk Young's modulus [N/m^2]
E_c	Charge energy [J]
E_v	Voltage field [V/m]
$E_{v,max}$	Maximum allowed voltage field [V/m]
$\mathbf{e}$	Piezoelectric force coefficient [N/Vm]
F	Force [N]
F_0	Force amplitude [N]
$\mathbf{g}$	Piezoelectric voltage constant [Vm/N]
$\mathbf{h}$	Piezoelectric constant [V/m]
h_{FE}	Transistor current gain ratio [-]
I	Current [A]
I_p	Piezo current [A]
I_r	Rectifier current [A]
i	Imaginary number
J	Mass moment of inertia [kg/m^2]
L_1, L_2	Inductance (Primary and secondary) [H]
L_s	Stack length [m]
k_e	Electromechanial coupling coefficient
k_{ij}	Electromechanical coupling coefficient of a piezo element (operation mode specified)
k	Stiffness [N/m]
k_p	Piezo element stiffness [N/m]

k_s	Structure stiffness (excluding piezo material) [N/m]
l	Length [m]
M	Mass [kg]
M_0	Moment excitation amplitude [Nm]
n	Number of layers [-]
P	Power [W]
P_{avg}	Time averaged power output [W]
P_{max}	Maximum power output [W]
P'_{avg}	Normalised time averaged power output [W]
Q	Electric charge [C]
Q_i	Inductor quality factor [-]
q_I	Inverion efficiency, $e^{-\pi/(2Q_i)}$
R	Resistance [Ω]
R_D, R_d, R_e	High current and low current discharge resistor, envelope charging resistor [Ω]
R	Blade radius (chapter 4 only) [m]
R_L	Intrinsic resistance of an inductor [Ω]
R_{max}	Maximum resistance [Ω]
R_{opt}	Optimal resistance [Ω]
r	Normalised resistance [-]
r	Normalised span-wise rotor coordinate, from 0 to 1 [-] (chapter 4 only)
r_{max}	Normalised maximum resistance [-]
r_{opt}	Optimal normalised resistance [-]
$\mathbf{S}^D, \mathbf{S}^E$	Piezoelectric stiffness matrix at constant electrical displacement or voltage field [N/m^2]
s	Surface coordinate along blade circumference in $\eta\zeta$ plane[m]
$\mathbf{T}$	Transformation matrix
T	Oscillation period [s]
t	Time [s]
t_{inv}	Inversion time [s]
t_l	Layer thickness [m]
u	Mechanical displacement [m]
u_0	Mechanical displacement amplitude[m]
u'_0	Normalised mechanical displacement amplitude [m]
V_0	Voltage amplitude [V]
V'_0	Normalised voltage amplitude [V]
V_d	Diode drop [V]
V_{ac}	AC voltage [V]
V_{dc}	Voltage in the DC part of an electrical circuit [V]
V_p	Piezo voltage [V]
$\mathcal{V}$	Volume [m^3]
w	Width [m]

Greek symbols

$\boldsymbol{\beta}^{\varepsilon}$	Inverse permittivity matrix at constant stain [m/F]
ϵ	Permittivity [F/m]
ϵ_r	Relative permittivity [-]
$\boldsymbol{\epsilon}^{\varepsilon}, \boldsymbol{\epsilon}^{\sigma}$	Electric permittivity matrix at constant strain / stress [F/m]
$\varepsilon_{ij}, \boldsymbol{\varepsilon}$	Strain component, vector [-]
ζ	Normalised mechanical damping coefficient [-]
ζ	Local blade axis ($\eta\zeta$ frame)
η	Local blade axis ($\eta\zeta$ frame)
η	Efficiency [-]
θ	Piezoelectric force coefficient [N/V]
κ	Curvature of neutral line [1/m]
ρ	Density [kg/m^3]
$\sigma_{ij}, \boldsymbol{\sigma}$	Stress component, vector [Pa]
τ	Angle between the rotor xy coordinate system and the blade $\eta\zeta$ system [-]
Φ	Mode shape [-]
ϕ	Azimuth angle [rad]
ξ	Blade lead angle [rad]
χ	Characteristic function [-]
Ω	Normalised frequency [-]
Ω_R	Rotor frequency [rad/s]
ω	Frequency [rad/s]
ω_{inv}	Inversion frequency [rad/s]
$\omega_n, \omega_m, \omega_{el}$	Natural frequency, mechanical natural frequency, electrical natural frequency [rad/s]
ω_{sc}, ω_{oc}	Short circuit and open circuit mechanical natural frequency [rad/s]

Abbreviations

ACIM	Alternating Current Impedance Matching
AW	Agusta Westland
BJT	Bipolar Junction transistor
CG	Centre of Gravity
DCIM	Direct Current Impedance Matching
FET	Field Effect Transistor
GRC	Green Rotor Craft
IPM	Ideal Physical Model
MOSFET	Metal-Oxide Semiconductor Field Effect Transistor
PVDF	PolyVinyliDene Fluoride
PZT	Lead Zirconate Titanate
SECE	Synchronous Electric Charge Extraction
SSHI	Synchronised Switch Harvesting on Inductor
VBEH	Vibration Based Energy Harvesting

Appendices

Appendix A

Alternative formulations of the piezoelectric equations

The piezoelectric equations can be formulated using 4 different sets of equations and associated variables. These are referred to as the *d*, *e*, *g* and *h* formulations. The variables are linked using additional sets of equations.

$$\begin{Bmatrix} \boldsymbol{\varepsilon} \\ \mathbf{D} \end{Bmatrix} = \begin{bmatrix} \mathbf{S}^E & \mathbf{d}^T \\ \mathbf{d} & \boldsymbol{\epsilon}^\sigma \end{bmatrix} \begin{Bmatrix} \boldsymbol{\sigma} \\ \mathbf{E} \end{Bmatrix} \tag{A.1}$$

$$\begin{Bmatrix} \boldsymbol{\sigma} \\ \mathbf{D} \end{Bmatrix} = \begin{bmatrix} \mathbf{C}^E & -\mathbf{e}^T \\ \mathbf{e} & \boldsymbol{\epsilon}^\varepsilon \end{bmatrix} \begin{Bmatrix} \boldsymbol{\varepsilon} \\ \mathbf{E} \end{Bmatrix} \tag{A.2}$$

$$\begin{Bmatrix} \boldsymbol{\varepsilon} \\ \mathbf{E} \end{Bmatrix} = \begin{bmatrix} \mathbf{S}^D & \mathbf{g}^T \\ -\mathbf{g} & \boldsymbol{\beta}^\sigma \end{bmatrix} \begin{Bmatrix} \boldsymbol{\sigma} \\ \mathbf{D} \end{Bmatrix} \tag{A.3}$$

$$\begin{Bmatrix} \boldsymbol{\sigma} \\ \mathbf{E} \end{Bmatrix} = \begin{bmatrix} \mathbf{C}^D & -\mathbf{h}^T \\ -\mathbf{h} & \boldsymbol{\beta}^\varepsilon \end{bmatrix} \begin{Bmatrix} \boldsymbol{\varepsilon} \\ \mathbf{D} \end{Bmatrix} \tag{A.4}$$

Matrices **C** and **S** represent the compliance and stiffness, respectively. The electrical field **E** and charge displacement **D** also function as superscripts. For instance, $\mathbf{S}^E$ indicates the stiffness matrix for a constant electrical field. Variables **d**, **e**, **g** and **h** are the various piezoelectric coefficients. Lastly, the permittivity and its inverse are denoted using $\boldsymbol{\epsilon}$ and $\boldsymbol{\beta}$. All the variables are linked using the following equations.

$$\begin{array}{lll} \mathbf{C}^E\mathbf{S}^E=\mathbf{I} & \mathbf{C}^D=\mathbf{C}^E+\mathbf{e}^T\mathbf{h} & \mathbf{e}=\mathbf{d}\mathbf{C}^E \\ \mathbf{C}^D\mathbf{S}^D=\mathbf{I} & \mathbf{S}^D=\mathbf{S}^E-\mathbf{d}^T\mathbf{g} & \mathbf{d}=\boldsymbol{\varepsilon}^\sigma\mathbf{C}^E \\ \boldsymbol{\epsilon}^\varepsilon\boldsymbol{\beta}^\varepsilon=\mathbf{I} & \boldsymbol{\epsilon}^\sigma=\boldsymbol{\epsilon}^\varepsilon+\mathbf{d}\mathbf{e}^T & \mathbf{g}=\boldsymbol{\beta}^\sigma\mathbf{d} \\ \boldsymbol{\epsilon}^\sigma\boldsymbol{\beta}^\sigma=\mathbf{I} & \boldsymbol{\beta}^\sigma=\boldsymbol{\beta}^\varepsilon-\mathbf{g}\mathbf{h}^T & \mathbf{h}=\mathbf{g}\mathbf{C}^D \end{array}$$

Appendix B

Element equations for various actuation modes

Following the derivation given in section 2.3 it is possible to derive similar element equations for different actuation modes. Consider first a patch operating in 31 mode under a plane stress assumption. The dimensions along the 1, 2 and 3 axes are, l, w, and t respectively. A lumped Young's modulus E_{11} is assumed. The length change of interest is that along axis 1. Also note that the relevant variables are the elasticity and piezoelectric constant along the 1 axis. Starting from the constitutive equations 2.1 and using the same assumptions the following can be written:

$$\frac{F}{wt} = E_{11}^{E}\frac{\Delta l}{l} + e_{31}\frac{V_p}{t} \tag{B.1a}$$

$$\frac{Q_3}{lw} = e_{31}\frac{\Delta l}{l} - \epsilon^{\varepsilon}\frac{V_p}{t} \tag{B.1b}$$

Note that here the mechanically loaded surface is the 13 surface with respective area wt, and the capacitance is created by the 12 surface with area lw. Multiplying each equation by the relevant surface area, deriving the second equation with respect to time and rearranging:

$$F = \frac{E_{11}^{E}wt}{l}\Delta l + \frac{e_{31}wt}{t}V_p \tag{B.2a}$$

$$Q_3 = \frac{e_{31}lw}{l}\dot{\Delta} l - \frac{\epsilon^{\varepsilon}lw}{t}\dot{V}_p \tag{B.2b}$$

The following parameters are then recognised for the 31 actuation mode:

$$k_p = \frac{E_{11}^{E}wt}{l}, \qquad \theta = e_{31}w, \qquad C_p = \frac{\epsilon^{\varepsilon}lw}{t} \tag{B.3}$$

Note that the capacitance remains unchanged. Secondly the stiffness is, as expected, that of the element along the loaded axis. Thirdly, the piezoelectric coupling coeffecient is now dependent on only the width of the element. The thickness t cancels out.

Consider next a stack of piezoelectric plates operating in the 33 mode, with alternating positive and negative electrodes. All the individual capacitances are then coupled in parallel. Let n be the number of layers, t_l the layer thickness, A the cross-sectional area perpendicular to the 3 axis and L_s the stack length (with $L_s = nt$). Considering 33 mode operation the constitutive equations are rewritten as:

$$\frac{F}{A} = E_{33}^E \frac{n\Delta t}{nt_l} + e_{33}\frac{V_p}{t_l} \tag{B.4a}$$

$$\frac{Q_3}{nA} = e_{33}\frac{n\Delta t}{nt_l} - \epsilon^{\varepsilon}\frac{V_p}{t_l} \tag{B.4b}$$

A few remarks concerning these equations: the loaded cross section is simply wl. The elongation can be written in terms of L_s or nt. The choice for nt becomes clear in the next step. The voltage field is dependent only on t, not nt. This is because the layers are electrically coupled in parallel: each layer experiences the same voltage relative to ground. In the case of series coupling the voltage field would be V/L_s. Note that due to the parallel electrical coupling the relevant surface area is the total area of all electrodes, hence nA. Therefore, in the second equation the generated charge is divided by nA. For electrical series coupling, n would be omitted.

Rewriting and again deriving the second equation yields:

$$F = \frac{E_{33}^E A}{L_s}\Delta L_s + \frac{e_{33}A}{t_l}V_p \tag{B.5a}$$

$$Q_3 = \frac{e_{33}A}{t_l}\Delta \dot{L}_s - \frac{\epsilon^{\varepsilon}nA}{t_l}\dot{V}_p \tag{B.5b}$$

For the multilayer stack the following parameters arise:

$$k_p = \frac{E_{33}^E A}{L_s}, \qquad \theta = \frac{e_{33}A}{t_l}, \qquad C_p = \frac{\epsilon^{\varepsilon}nA}{t_l} \tag{B.6}$$

The stiffness value is again expected, as is the capacitance. The piezoelectric coupling coefficient is now dependent on the geometry of a single layer, not the total length of the stack.

Appendix C

DC Impedance matching operation

C.1 Conceptual circuit operation

The DCIM circuit [20, 56] has 3 modes of operation. The positive and negative rectifier conduction phases and the alternating phase where the piezo voltage changes with displacement. The positive conduction phase is shown in figure C.1. Here the current is positive upward through the current source. For the negative conduction phase the current flows opposite the arrow and the other diode pair becomes active. Simultaneously energy is dissipated in the resistor.

In figure C.2 the alternating phase is shown. The AC voltage of the piezo element is going from positive to negative or vice versa and the storage capacitor is discharging energy through the resistor. The rectifier is fully blocked.

C.2 Circuit waveforms

Figure C.3 show the resulting waveforms for various settings of the load resistance. All figures have the same normalised scale to demonstrate the differences in magnitude. For a resistance below the optimal resistance (subfigures (b) and (c)) the voltage is relatively low and the conduction phase is longer than the alternating phase. For a load of 0 Ω the conduction phase would be the only phase but the zero voltage implies no harvested power.

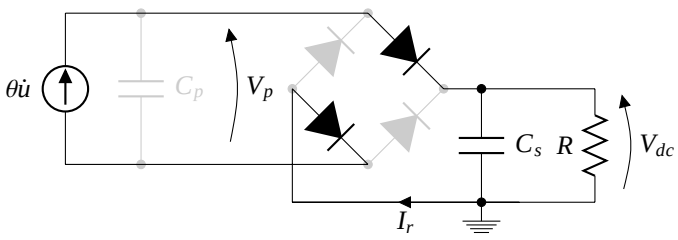

Figure C.1: DCIM circuit conduction phase.

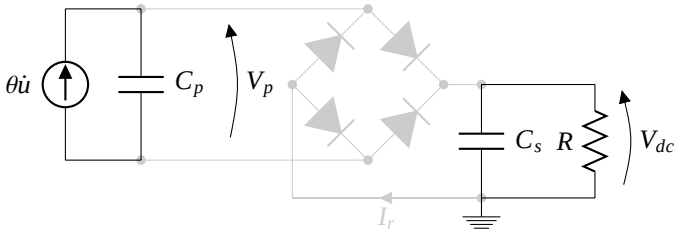

Figure C.2: DCIM alternating phase.

As the resistance increases to the optimal value (subfigures (d) and (e)) voltage increases significantly and the duration of the conduction phase decreases to a duty of 50%. Here there is voltage as well as current, implying a transfer of power.

Further increasing the load resistance above the optimal value (subfigures (f) and (g)) shows a less profound increase in the voltage and the duration of the conduction phase decreases further. For the limit value of an infinite resistance the voltage would be maximised to the open circuit value but the duty of the conductive phase would be zero, again leading to no transfer of power from the piezo element to the DC part of the circuit.

C.3 Determination of parameters

The ideal load resistance (real and normalised) for low coupled systems is

$$R_{opt} = \frac{\pi}{2C_p\omega} \qquad r_{opt} = \frac{\pi}{2\Omega} \tag{C.1}$$

The determination of the capacitance C_s is based on the desired RC_s time t_{RC} of the DC branch of the circuit:

$$C_s = \frac{t_{RC}}{R} \tag{C.2}$$

To ensure a fairly constant DC voltage, t_{RC} must satisfy the following inequality with the period of excitation: $t_{RC} \gg T$.

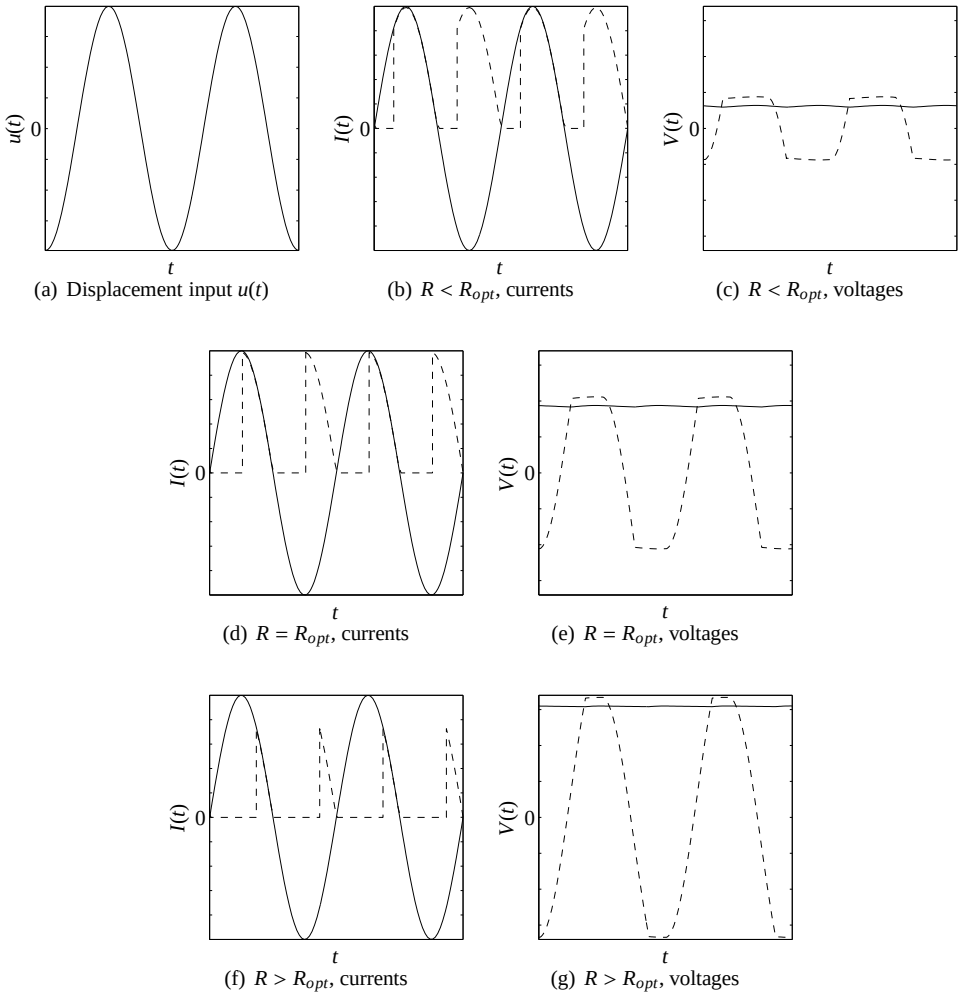

(a) Displacement input $u(t)$ (b) $R < R_{opt}$, currents (c) $R < R_{opt}$, voltages

(d) $R = R_{opt}$, currents (e) $R = R_{opt}$, voltages

(f) $R > R_{opt}$, currents (g) $R > R_{opt}$, voltages

Figure C.3: DCIM waveforms for varying resistance values. Currents shown are $\theta\dot{u}$ (——) and I_r (– – –). Voltages shown are V_{dc} (——) and V_p (– – –).

Appendix D

SECE Circuit

The Synchronous Electric Charge Extraction (SECE) circuit [17] is an active circuit that operates mainly in the open circuit mode. Only when the accumulated charge has reached a maximum is the piezo element quickly discharged through a single or coupled inductor. The inductor then passes its energy on to the storage capacitor. The conceptual operation is first elaborated on, followed by the derivation of equations which drive the parameters of the individual components. Physical implementation is not discussed due to the lack of literature concerning the switch which must control the discharging process.

D.1 Conceptual circuit operation

The SECE circuit has three phases of operation. First is the charging phase, figure D.1. The piezo element is in open circuit mode and accumulates charge across its electrodes. Due to the open circuit operation the final voltage is easy to calculate using the open circuit variation of equation 2.8:

$$V_{max} = \frac{2\theta u_0}{C_p} \tag{D.1}$$

Upon reaching the maximum voltage the primary discharge phase starts. A switch is closed, allowing the element to discharge through an inductor, figure D.2. The current source is greyed out to signify that the discharging takes place much more rapidly than the change in the piezoelectric charge displacement. The switch must open again precisely when the piezo voltage has been reduced to zero. By doing to, the magnetic field in the core of the inductor is maximised and the secondary discharge phase starts. Depending on the implementation, a continued current is generated through the single inductor, or a new current is generated in the secondary coil of the coupled inductor, shown in figure D.3. This current charges the storage capacitor and the piezo element begins to charge again.

As with the other circuits, the capacitor C_s is chosen sufficiently large such that the DC voltage remains nearly constant. Because there is no direct link between the piezo element and the storage capacitor, there is also no optimal load resistance, as discussed in section 3.5.

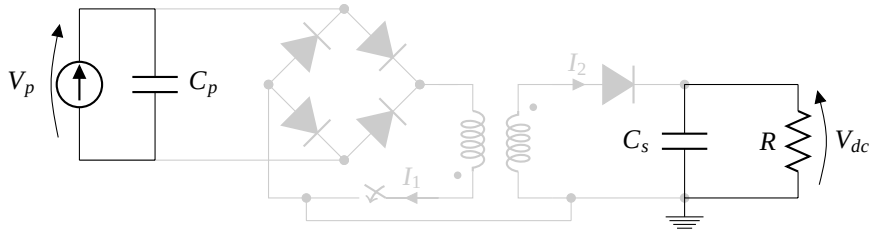

Figure D.1: SECE charging phase.

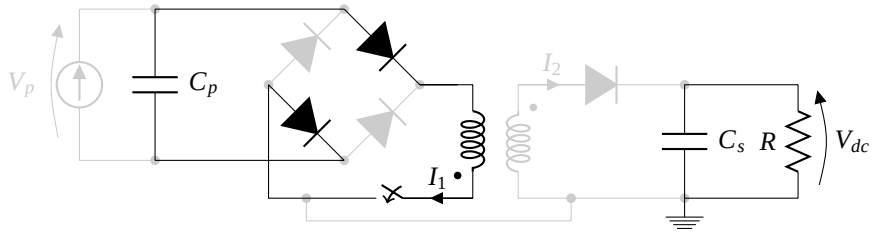

Figure D.2: SECE primary discharging phase.

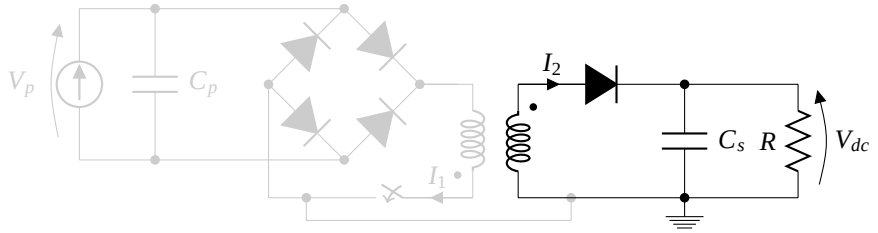

Figure D.3: SECE secondary discharging phase.

D.2 Circuit waveforms

The associated waveforms are presented in figure D.4. The current plot (b) and voltage plot (d) cover only one discharge event. Current I_1 is above zero only during the primary discharge phase. Current I_2 is only above zero for the secondary discharge phase. The sharp decrease in voltage V_p occurs only during the primary discharge phase.

D.3 Determination of parameters

With the addition of a coupled inductor comes the determination of the desired inductance values. Starting with the primary coil the following holds for the natural frequency of the LC circuit, and the duration of the primary discharge phase:

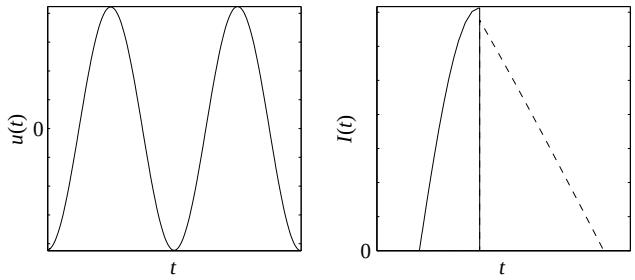

(a) Displacement input $u(t)$ (b) I_1 (——) and I_2 (– – –)

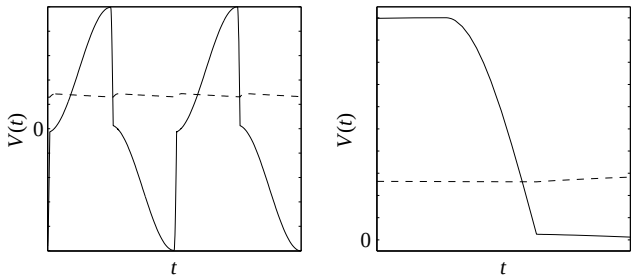

(c) V_p (——) and V_{dc} (– – –) (d) Voltages during discharge

Figure D.4: SECE circuit waveforms.

$$\omega_{el} = \frac{1}{\sqrt{C_p L_1}} \qquad t_{dis} = \frac{1}{2}\pi\sqrt{L_1 C_p} \tag{D.2}$$

Depending on the choice of the designer, either the discharge duration t_{dis} or the choice of the primary inductance L_1 can be leading. For the secondary circuit coil, a similar approach is taken but with different results. Due to the assumption that the DC voltage remains constant, the current discharging from the secondary winding decreases linearly with time, as shown in figure D.5. The standard inductor equation then leads to the following:

$$t_{off} = \frac{I_2 L_2}{V_{dc}} \tag{D.3}$$

The secondary peak current I_2 follows from an energy balance of the inductor. The energy within an inductor is $LI^2/2$. Writing an energy balance from the piezo element to the secondary inductor coil yields:

$$\frac{1}{2}C_p V_{p,0}^2 = \frac{1}{2}L_2 I_2^2 \tag{D.4}$$

From 3.11 the normalised power is:

$$P'_{max} = \frac{2k_e^2 \Omega u_0'^2}{\pi} \tag{D.5}$$

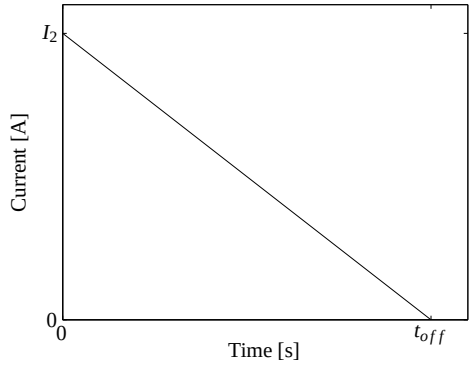

Figure D.5: Schematic representation of the SECE secondary discharge current.

Rewriting in physcial quantities and recognising that $P = V_{dc}^2/R$, the following equation is found for the DC voltage:

$$V_{dc} = V_{p,0}\sqrt{\frac{\Omega C_p R}{2\pi}} \tag{D.6}$$

Combining equations D.3, D.4 and D.6 yields:

$$L_2 = \frac{\Omega R t_{off}^2}{2\pi} \tag{D.7}$$

This equation gives the relation between the choice of the inductance L_2 and the time it takes to discharge the current into the storage capacitor. The following summarises the results for the currents in the circuit:

$$I_1 = V_{p,0}\sqrt{\frac{C_p}{L_1}} \qquad I_2 = V_{p,0}\sqrt{\frac{C_p}{L_2}} \tag{D.8}$$

These final equations emphasise the choice that must be made, either minimising the current or the inductance value. For small stacks this is not an issue, but as the size increases this becomes more of a challenge.

Appendix E

SSHI circuit

The SSHI circuit functions very similarly to the DCIM circuit. The difference is the addition of a switched inductor on the AC side as indicated in figures 3.16 and E.1. As shown in section 3.2, a capacitor and inductor form an electrical oscillator. The purpose of this inductor is to switch the voltage electronically from positive to negative and vice versa. Its natural frequency must therefore be much higher than the dominant frequency of the mechanical system.

First, the conceptual operation will be discussed to develop understanding of the advantages of the circuit and second, the physical implementation will be addressed and the relevant additional circuitry introduced. The last section will cover the analytical determination of critical parameters within the circuit.

E.1 Conceptual circuit operation

There are 3 phases in the circuit operation. Starting with the conduction phase, the piezo voltage has reached the threshold voltage of the rectifier ($|V_p| \geq V_{dc}$) and is conducting through the rectifier to the DC side of the circuit as in figure E.1. When the piezo voltage begins to drop the switching phase starts, figure E.2. The switch closes, allowing the electrical oscillator to work at the electrical natural frequency formed by the piezo capacitance and inductance: $\omega_{el} = 1/\sqrt{C_p L_1}$. When half an oscillation is complete the switch opens, leaving the piezo voltage at the maximum opposite value when compared to the start of the switching phase. With the switch open no current passes through the inductor and the recovery phase starts, figure E.3. The switching process incurs a voltage loss, which depends on the quality of the inductor, which must be recovered by the piezo element.

The piezo voltage then again reaches $|V_p| \geq V_{dc}$ starting the opposite conduction phase. A second switch is used to switch the voltage in the opposite direction. Note that in the circuit diagram of figure E.2 two switches are shown which are connected with opposite polarity. This is due to the physical design of the switch which can only operate in one direction (see figure E.5).

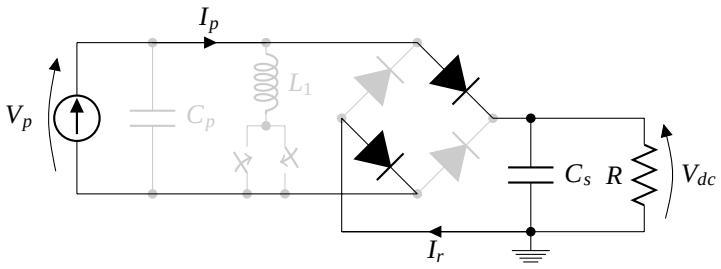

Figure E.1: SSHI conduction phase.

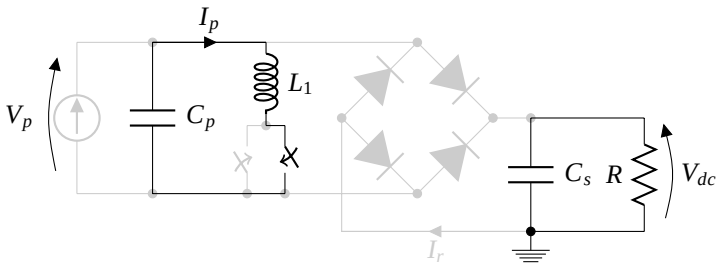

Figure E.2: SSHI switching phase.

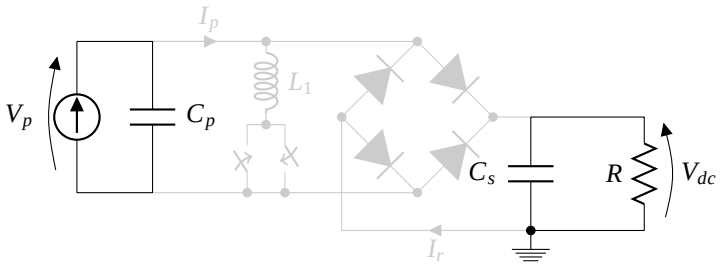

Figure E.3: SSHI recovery phase.

E.2 Circuit waveforms

Indicative waveforms for a displacement driven harvester are shown in figure E.4. The input (a) is sinusoidal. The inversion frequency is chosen as 25 times larger than the excitation frequency with a quality factor Q_i of only 5. The storage capacitance C_s is again chosen sufficiently large to prevent any appreciable decrease in V_{dc} in between two consecutive conduction phases. Note, however, that due to the much higher ideal load resistance this capacitance is much smaller than the DCIM case. The result here is a storage capacitance that is only 10 times the piezo capacitance.

In (b) the piezoelectrically generated current and the current at the piezo contacts is shown for the optimal load resistance. The generated current ($\theta\dot{u}$) is sinusoidal, with 90 degrees phase difference to the displacement. The piezo current peaks exceeding beyond the bounds are the currents associated with inverting the voltage and are half sine-waves. The peak inductor current is $V_{p,0}\sqrt{C_p/L}$. The visible extrema show the rectifying currents. Note that the piezo current is somewhat lower than the generated current. This is due to the smaller storage capacitance. Lastly, the trend of the piezo current for increasing load resistance is the same as for the DCIM case. As the resistance increases the duty cycle decreases to zero for an infinite load resistance.

Figures E.4(c), (d) and (e) show the voltage levels for a load resistance that is less than optimal, optimal and more than optimal, respectively. Comparing these to figure 3.11 the DC voltage of figure E.4(c) can already exceed that of the optimal case for DCIM, for an identical mechanical setup. A similar trend holds here as for the DCIM case: as the load resistance increases, the conduction phase becomes shorter, and the peak voltage increases. Differing from DCIM, although the piezo voltage is shown to increase with higher resistance, the resulting voltage for an infinite resistance is many times higher. The value for the SSHI circuit far exceeds the open circuit voltage of the piezo element alone, due to the inversion operation. Caution is required to prevent an excessive reverse field in the material.

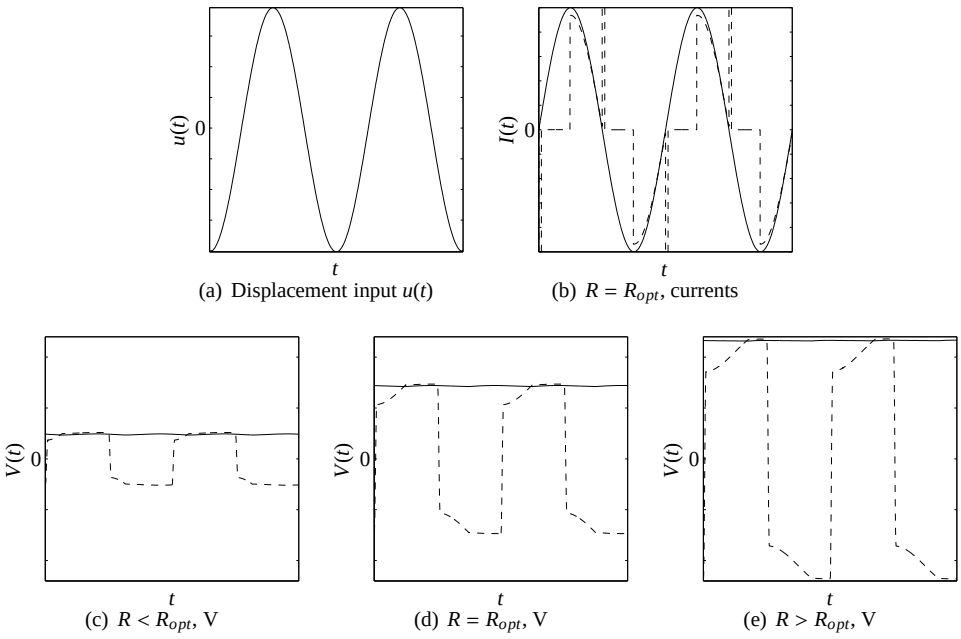

(a) Displacement input $u(t)$ (b) $R = R_{opt}$, currents

(c) $R < R_{opt}$, V (d) $R = R_{opt}$, V (e) $R > R_{opt}$, V

Figure E.4: SSHI waveforms for varying resistance values. Currents shown are $\theta\dot{u}$ (——) and I_p (– – –). Voltages shown are V_{dc} (——) and V_p (– – –).

E.3 Physical implementation

The challenge with the SSHI circuit is the electronics within the switch. It must be self-powered, efficient, and capable of the action described previously. The switching circuit used here is shown in figure E.5 [25]. It consists of a capacitor, diodes, resistors, an NPN and a PNP transistor. The capacitor C_e functions as a voltage envelope detector. It follows the piezo voltage with a slight delay as it is charged through R_c, creating an R_cC_e circuit as shown in figure E.6(a).

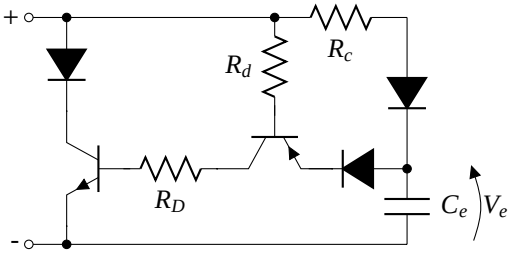

Figure E.5: SSHI switching circuit diagram.

When the piezo voltage drops below the envelope voltage V_e, the switch becomes active, see figure E.6(b). As the piezo voltage drops, the PNP transistor begins to conduct a current I_d through resistor R_d. This allows a larger current I_D to flow through R_D as well. Both are discharge resistors with R_D sinking most of the current. Recall the current ratio of the PNP transistor (section 3.3), ideally R_D is chosen as nearly a factor h_{FE} smaller than R_d. This current I_D then passes through the NPN transistor, allowing a collector-emitter current which is the inductor current I_L. The following inequality holds for the various currents: $I_L \gg I_D \gg I_d$. The diode connected to the collector of the NPN transistor prevents any reverse current, closing the switch precisely when the inductor current reaches zero.

E.4 Determination of parameters

Determining the switch parameters requires a number of basic electrical calculations. Due to the use of transistors this calculation is based on the required currents. Therefore all values must be back-calculated based on the voltage of the piezo element at the onset of switching, $V_{p,0}$. Transient switching effects surrounding the transistor-turn-on are ignored to simplify the approach, as these typically require in the order of nanoseconds to complete and minimally influence the actual voltage and current levels.

First the maximum switching current $I_{p,0}$ must be determined. Assuming an undamped second order system (LC circuit) the energy present in the capacitor at $t = 0$ must equal the energy in the inductor after one quarter of the vibration period. At this time all energy in the capacitor has been transferred to the inductor, which then has maximum current passing through it. The maximum switching current is therefore:

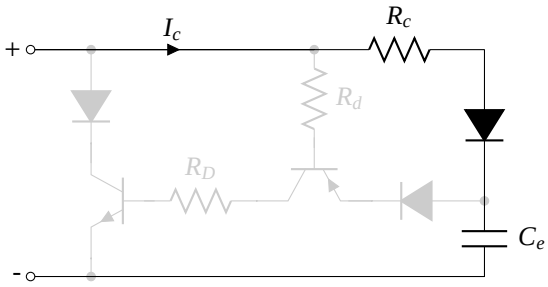

(a) Charging

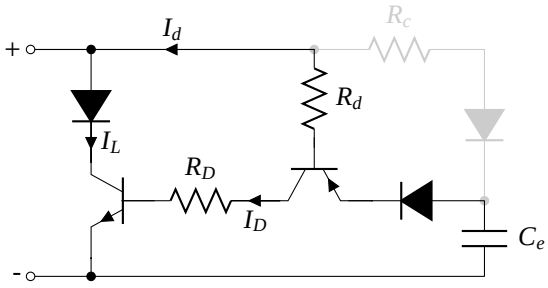

(b) Discharging

Figure E.6: Switching circuit charge and discharge phases.

$$\frac{1}{2}L_1 I_{p,0}^2 = \frac{1}{2}C_p V_{p,0}^2 \tag{E.1a}$$

$$I_{p,0} = V_{p,0}\sqrt{\frac{C_p}{L_1}} \tag{E.1b}$$

For the NPN transistor the inequality $h_{FE}I_{BE} \geq I_{CE}$ holds; this is required to remain in the saturation region of the transistor. The collector current I_{CE} is the same as the inductor current I_L and is a sinusoidal signal. I_{BE} is equal to I_D, resulting from the discharging of the envelope capacitor C_e through resistor R_D. The current through R_d is ignored here because h_{FE} is typically in the order of 100 or more (recall the current gain of the transistor). This leads to the following inequality for R_D and C_e:

$$\frac{V_{p,0}}{R_D}e^{\frac{-t}{R_D C_e}} \geq V_{p,0}\sqrt{\frac{C_p}{L_1}}\sin\left(\frac{t}{\sqrt{C_p L_1}}\right) \tag{E.2}$$

In reality, a number of diode drops are also present in the circuit, one for current I_L and two for I_D. For large V_0 these become negligible. However, even when ignoring the diodes this equation has no closed form solution. This equation must be solved numerically, allowing

for simple inclusion of the diode drops. Figure E.7 shows an example for a current ratio of 88 for the NPNBJT[1]. The axes in the figure are all normalised, showing the capacitance ratio C_e/C_p, the R_DC_e time of the envelope capacitor normalised with the oscillation period of the inductor, and the vertical axis the minimal normalised current margin $(I_D - I_L)/I_{p,0}$. This must be positive for the switch to operate. In order to minimize the power consumption of the switch, a minimal value of the envelope capacitance C_e must be chosen.

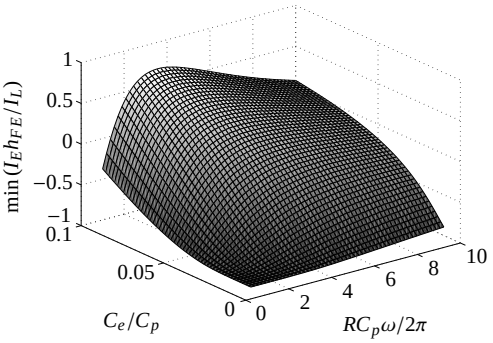

Figure E.7: The current ratio margin for the self-powered switch, $h_{FE} = 88$.

With C_e and R_D set, R_d can be chosen up to $h_{FE}^{PNP}R_D$. This resistor value quickly exceeds 10^7 Ω because the h_{FE} of small signal transistors can be 500 or more. For the investigations of chapter 6, R_D is in the order of 10 kΩ. A resistor in the MΩ range is therefore sufficient.

The charge resistor R_c is not very critical. It is used to tune how sensitive the envelope detector is. If it is too low the envelope capacitor charges quickly and the switch may respond to high frequency oscillations. If it is too low the envelope capacitor does not accurately follow the envelope of the excitation frequency. A decent first choice for the R_cC_e time is in the order of t_{inv}.

With all quantities determined it is possible to turn to results. An example of the operation of the SSHI circuit around one voltage inversion is shown in figure E.8. First the absolute piezo voltage drops below the absolute envelope voltage. Once the difference is large enough to overcome the diode drop from the diode and PNP transistor, the envelope capacitor begins to discharge. In the figure this occurs at $t = 1.1$ ms. The collector current from the PNP passes through the NPN as well. The latter transistor switches into saturation due to V_{CE} dropping to nearly zero. With the NPN allowing a collector-emitter current, V_p inverts while V_e decreases exponentially. When the peak reverse amplitude has been reached the diode prevents reverse conduction. The slight decrease in V_p following the completion of the inversion is due to the coupling ($k_e^2 = 0.013$) in this example. The sharp change in voltage alters the balance of forces in the mechanical domain. Initial charging of the opposite envelope capacitor also decreases the stack voltage.

The associated currents are shown in the figure as well. The PNP base current is not shown because it is a factor of 150 smaller than the NPN base current. The end of the

[1]This is exemplary for a BD139 transistor switching a 1μF capacitor charged to 30 volts, over a 1mH inductor, as in sections 6.4 and 6.5.

previous conduction phase can just be seen adjacent to the *y*-axis as well as the start of the next conduction phase after $t = 2.5$ ms. The small voltage drop following the inversion phase seen in the previous figure can be seen here as well as the piezo current drops below zero. The inductor current is mostly identical to the piezo current, but does not go negative following inversion. This is due to the opposite envelope capacitor acquiring some of the charge.

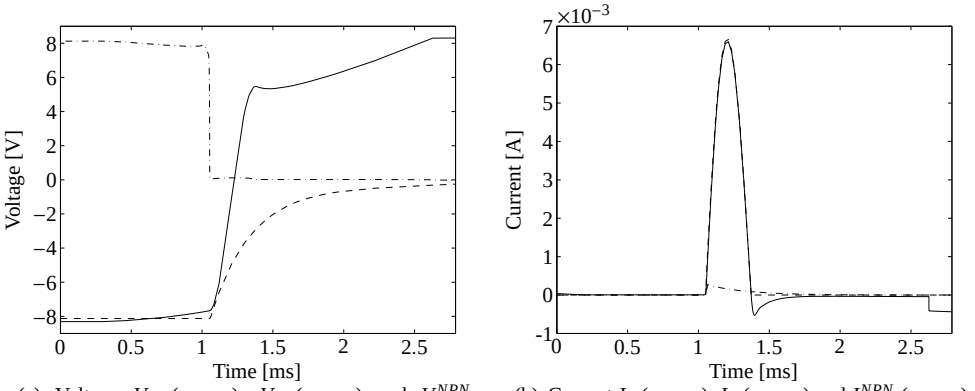

(a) Voltage V_p (———), V_e (– – –) and V_{CE}^{NPN} (– · – · –)

(b) Current I_p (———), I_L (– – –) and I_B^{NPN} (– · – · –)

Figure E.8: An example of the voltages and currents during an inversion event.

E.5 FET based switch

It is also possible to alter the circuit to use a MOSFET as the switching element. This requires a far smaller envelope capacitor C_e since I_e is no longer required to be a ratio of I_L: the FET is voltage controlled. The layout is shown in figure E.9. The added diode is to prevent reverse operation of the PNP transistor [2].

Considering the minimally required voltage $V_{GS,on}$ to open the FET completely the envelope capacitor must now maintain a V_{GS} of at least that value until time t_{inv} from the onset of switching. The combined resistance of R_d and R_D (R') must be considered in combination with C_e to provide an $R'C_e$ time that is sufficient to achieve this requirement. Using the discharging variant of equation 3.4, the inversion time of the LC circuit for t, and a voltage ratio of $V_{GS(on)}/V_0$ the following relation is found for $R'C_e$:

$$V_{GS(on)} = V_0 e^{\frac{-2\pi\sqrt{L_1 C_p}}{R'C_e}} \rightarrow \frac{-\pi\sqrt{L_1 C_p}}{\ln \frac{V_{GS,on}}{V_0}} = R'C_e \tag{E.3}$$

Note that if the piezo voltage amplitude V_0 does not reach $V_{GS,on}$ then the switch will not function optimally, if at all. With the value of $R'C_e$ known, C_e must be chosen as small as possible to maximise efficiency of the switch. The trade-off is an unrealistically high

[2] Consider the diode model of the NPNBJT. In the NPN transistor based circuit, the diode action of the NPN transistor itself provides this safety.

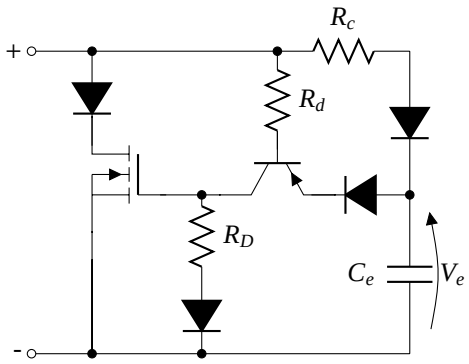

Figure E.9: Self-powered circuit layout, MOSFET variant.

resistance where 1 MΩ is already quite high, limiting how low C_e can go. There are also transient effects within the circuit and parasitic capacitances in all semiconductor components as well as diode losses. A margin must be maintained for C_e so that these effects remain minor. A value of a few percent of C_p combined with the associated resistor for the desired RC time is a good rule of thumb, after which R_d and R_D can be determined.

Appendix F

GRC Rotor blade data

The dynamic data used to calculate the power output of the in-blade power harvesting concept of chapter 4 is listed here. The geometrical properties, mass and stiffness properties, natural frequencies, and the Fourier series of the tip displacement are all given here.

F.1 General properties

The rotor blade consists of two profiles, the NACA23012 from $r = 0.2$ to $r = 0.75$ and the OA209 from $r = 0.9$ to the tip. The region in between is a transition zone from one to the other. For the power calculation in chapter 4 only the NACA profile is considered, without the taper at the tip of the blade.

Table F.1: General properties.

Parameter	Value	Unit
Blade radius	8.15	m
Chord length	0.65	m
Rotor speed	26.26	rad/s

The geometrical twist gives the rotation of the aerofoil cross-section relative to a reference position. This position is the global pitch setting of the blade. In calculating the strains within the blade the local geometry must be known, the global strains and rotations must be multiplied with the distance from the neutral bending line.

F.2 Mass and stiffness data

The mass and stiffness data used to calculate the mode shapes are given in tables F.3 and F.4. Dynamic stiffening due to the rotor speed is included in the analysis. The mode shapes are calculated without damping. The mass increase at 90% is due to the inclusion of balance masses.

Table F.2: Geometrical twist.

r/R	Value [deg]
0.2	4.401
0.75	-1.099
0.9	-0.927
1	-1.927

Table F.3: Mass data.

R [%]	R [m]	Mass [kg/m]	ζ_{CG} [m]	η_{CG} [m]	I_ζ [kgm]	I_η [kgm]
5.00	0.407	70.00	0.00	0.000	1.0264	1.0264
15.00	1.222	70.00	0.00	0.000	1.0264	1.0264
20.00	1.630	21.99	0.00	0.000	0.0173	0.4944
90.00	7.335	12.37	0.00	0.000	0.0097	0.2781
90.00	7.335	51.71	0.00	0.000	0.0199	0.3747
91.67	7.471	51.48	0.00	0.000	0.0198	0.3731
91.67	7.471	12.14	0.00	0.000	0.0096	0.2729
94.70	7.718	11.73	0.00	0.000	0.0092	0.2636
96.40	7.857	9.88	0.00	0.036	0.0067	0.1997
98.20	8.003	5.53	0.00	0.146	0.0021	0.0816
100.00	8.150	1.22	0.00	0.325	0.0001	0.0132

Table F.4: Stiffness data.

R [%]	R [m]	EI_ζ [N/m^2]	EI_η [N/m^2]	EA [N]	GJ [N/m^2]	ζ_{NA} [m]	η_{NA} [m]
5.0	0.407	$3.897 \cdot 10^6$	$3.897 \cdot 10^6$	$5.939 \cdot 10^8$	$2.887 \cdot 10^6$	0.0	0.0
15.0	1.222	$3.897 \cdot 10^6$	$3.897 \cdot 10^6$	$5.939 \cdot 10^8$	$2.887 \cdot 10^6$	0.0	0.0
20.0	1.630	$2.837 \cdot 10^5$	$3.534 \cdot 10^6$	$4.871 \cdot 10^8$	$2.184 \cdot 10^5$	0.0	0.0
94.7	7.718	$1.513 \cdot 10^5$	$1.884 \cdot 10^6$	$2.597 \cdot 10^8$	$1.165 \cdot 10^5$	0.0	0.0
96.4	7.857	$1.095 \cdot 10^5$	$1.364 \cdot 10^6$	$2.187 \cdot 10^8$	$8.431 \cdot 10^4$	0.0	0.0
98.2	8.003	$3.510 \cdot 10^4$	$4.373 \cdot 10^5$	$1.225 \cdot 10^8$	$2.703 \cdot 10^4$	0.0	0.0
100.0	8.150	$1.756 \cdot 10^3$	$2.187 \cdot 10^4$	$2.709 \cdot 10^7$	$1.352 \cdot 10^3$	0.0	0.0

F.3 Fourier series data

The tip displacement of the blade during one revolution is described by a Fourier series [63]:

$$f_i(t) = \frac{a_{0,i}}{2} \sum_n \left[a_{n,i} \cos\left(n_i t\right) + b_{n,i} \sin\left(n_i t\right) \right] \tag{F.1}$$

with i representing the mode number. The coefficients a and b are given in table F.5

	L1	F1	F2	L2	F3	T1	F4	L3
a_0	$-6.28\cdot10^{-1}$	$4.54\cdot10^{-1}$	$-4.40\cdot10^{-4}$	$-8.39\cdot10^{-4}$	$-3.28\cdot10^{-3}$	$-1.65\cdot10^{-3}$	$-4.02\cdot10^{-4}$	$-6.51\cdot10^{-6}$
a_1	$-3.13\cdot10^{-2}$	$2.58\cdot10^{-1}$	$-1.30\cdot10^{-2}$	$1.28\cdot10^{-3}$	$-7.82\cdot10^{-4}$	$-1.12\cdot10^{-3}$	$-1.09\cdot10^{-4}$	$-4.20\cdot10^{-5}$
a_2	$1.63\cdot10^{-3}$	$7.36\cdot10^{-2}$	$-1.96\cdot10^{-2}$	$2.34\cdot10^{-4}$	$1.92\cdot10^{-3}$	$6.98\cdot10^{-5}$	$4.98\cdot10^{-5}$	$-4.97\cdot10^{-6}$
a_3	$1.24\cdot10^{-3}$	$3.81\cdot10^{-4}$	$9.94\cdot10^{-4}$	$4.82\cdot10^{-4}$	$-1.89\cdot10^{-4}$	$1.39\cdot10^{-5}$	$4.43\cdot10^{-5}$	$3.16\cdot10^{-6}$
a_4	$1.64\cdot10^{-4}$	$3.54\cdot10^{-4}$	$1.69\cdot10^{-3}$	$5.04\cdot10^{-4}$	$-1.61\cdot10^{-4}$	$-2.17\cdot10^{-4}$	$-9.37\cdot10^{-5}$	$-8.56\cdot10^{-6}$
a_5	$4.99\cdot10^{-5}$	$-5.95\cdot10^{-5}$	$3.10\cdot10^{-5}$	$4.97\cdot10^{-4}$	$7.74\cdot10^{-5}$	$-5.59\cdot10^{-5}$	$3.50\cdot10^{-5}$	$2.18\cdot10^{-6}$
a_6	$-2.98\cdot10^{-6}$	$-1.35\cdot10^{-4}$	$-2.34\cdot10^{-4}$	$-5.22\cdot10^{-5}$	$-3.55\cdot10^{-4}$	$-1.43\cdot10^{-4}$	$-1.43\cdot10^{-6}$	$5.97\cdot10^{-7}$
a_7	$-4.30\cdot10^{-6}$	$-2.58\cdot10^{-5}$	$7.77\cdot10^{-7}$	$-6.01\cdot10^{-5}$	$-1.70\cdot10^{-4}$	$-7.40\cdot10^{-5}$	$-9.45\cdot10^{-6}$	$2.24\cdot10^{-7}$
a_8	$-1.17\cdot10^{-6}$	$4.83\cdot10^{-5}$	$5.78\cdot10^{-5}$	$-7.40\cdot10^{-6}$	$2.09\cdot10^{-5}$	$7.46\cdot10^{-6}$	$-1.43\cdot10^{-5}$	$5.67\cdot10^{-7}$
b_1	$3.65\cdot10^{-2}$	$3.55\cdot10^{-1}$	$4.78\cdot10^{-2}$	$1.28\cdot10^{-3}$	$1.82\cdot10^{-3}$	$1.33\cdot10^{-3}$	$4.40\cdot10^{-5}$	$-8.23\cdot10^{-6}$
b_2	$4.97\cdot10^{-3}$	$1.35\cdot10^{-2}$	$-1.24\cdot10^{-2}$	$1.79\cdot10^{-4}$	$7.25\cdot10^{-4}$	$-4.55\cdot10^{-4}$	$-3.99\cdot10^{-5}$	$-1.80\cdot10^{-5}$
b_3	$-1.25\cdot10^{-3}$	$8.15\cdot10^{-3}$	$-5.13\cdot10^{-3}$	$-7.35\cdot10^{-4}$	$7.86\cdot10^{-4}$	$1.85\cdot10^{-4}$	$1.59\cdot10^{-4}$	$9.70\cdot10^{-6}$
b_4	$-9.29\cdot10^{-5}$	$1.87\cdot10^{-4}$	$2.34\cdot10^{-4}$	$-6.59\cdot10^{-5}$	$-2.21\cdot10^{-4}$	$-1.17\cdot10^{-4}$	$-5.21\cdot10^{-5}$	$-2.89\cdot10^{-6}$
b_5	$-1.09\cdot10^{-5}$	$8.64\cdot10^{-5}$	$1.65\cdot10^{-4}$	$-1.23\cdot10^{-4}$	$-6.89\cdot10^{-4}$	$-1.16\cdot10^{-4}$	$-4.54\cdot10^{-5}$	$-4.10\cdot10^{-6}$
b_6	$-3.38\cdot10^{-6}$	$-1.07\cdot10^{-4}$	$-1.06\cdot10^{-4}$	$1.40\cdot10^{-5}$	$1.88\cdot10^{-4}$	$1.26\cdot10^{-4}$	$4.65\cdot10^{-5}$	$2.25\cdot10^{-8}$
b_7	$-2.34\cdot10^{-7}$	$-4.76\cdot10^{-5}$	$-9.78\cdot10^{-5}$	$2.13\cdot10^{-5}$	$-1.65\cdot10^{-4}$	$-6.01\cdot10^{-6}$	$6.01\cdot10^{-5}$	$-9.13\cdot10^{-7}$
b_8	$3.03\cdot10^{-6}$	$-2.58\cdot10^{-5}$	$7.07\cdot10^{-6}$	$1.04\cdot10^{-5}$	$-6.88\cdot10^{-5}$	$-1.16\cdot10^{-5}$	$6.60\cdot10^{-5}$	$-9.62\cdot10^{-7}$

Table F.5: Tip motion Fourier series data.

F.4 Lag damper properties

The detailed lag damper curve is given here. The damper velocity data used in section 5.2 is derived from the motion analysis of the blade. The lag hinge angle multiplied by the mounting distance is used as the velocity input of the damper.

Table F.6: Lag damper data.

Velocity [m/s]	Force [N]
0.0	0.0
0.002	162.3
0.003	365.2
0.0051	1014.5
0.0076	2282.6
0.0102	4058.0
0.0127	6340.6
0.014	7672.2
0.0241	8608.8
1.016	18237.5

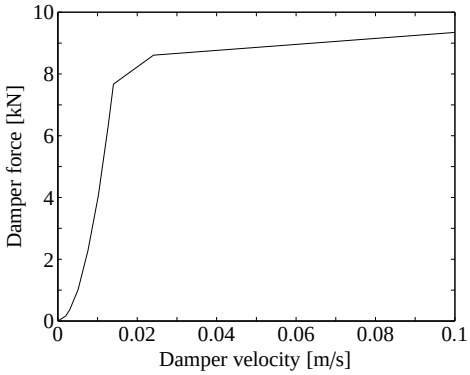

Figure F.1: Lag damper curve.

Appendix G

Power calculation for the rotor blade concept

In section 4.3 it is explained how the power is calculated for each patch within the rotor blade. The underlying equations are given here using the same numbering as the steps mentioned in section 4.3. The subscript i, j is omitted for ease of reading but is implied for most variables.

1. All times t_k are found for which the time derivative of the strain is zero:

$$\frac{d\varepsilon}{dt} = 0 \tag{G.1}$$

   The associated strains ε_k are stored.

2. The maximum strain variation is $\varepsilon_{max} - \varepsilon_{min}$. The maximum allowed strain for the material is ε_{mat}. A characteristic function χ^{ε} is formulated as follows:

$$\varepsilon_{max} - \varepsilon_{min} > \varepsilon_{mat} \rightarrow \chi^{\varepsilon} = 0 \tag{G.2a}$$

$$\varepsilon_{max} - \varepsilon_{min} < \varepsilon_{mat} \rightarrow \chi^{\varepsilon} = 1 \tag{G.2b}$$

3. The energy density of each discharge is calculated. First the strain input from the previous step is used to determine the strain field by rewriting the g approximation, as stated section 4.3.

$$\boldsymbol{\varepsilon} = \frac{\varepsilon_1}{S^D_{1,1}} \mathbf{S}^D_{m,1} \tag{G.3}$$

   Next the voltage field in the material is:

$$\mathbf{E} = -\boldsymbol{\beta}^{\varepsilon} \mathbf{e} \boldsymbol{\varepsilon} \tag{G.4}$$

   Note that $\boldsymbol{\beta}^{\varepsilon} = (\boldsymbol{\epsilon}^{\varepsilon})^{-1}$. The energy is calculated in two ways. Energy U_{loc} is calculated assuming each local extreme value triggers the SECE circuit. Energy U_{glo} is calculated

using the global extrema ε_{max} and ε_{min}, multiplied by 2 as one cycle yields 2 discharges. If the energy stored in a capacitor is $C_p V^2/2$, then substituting the capacitance equation and voltage field E_3 in the equation yields the following energies:

$$U_{loc} = \sum_k \frac{1}{2}\epsilon_3^{\varepsilon} wlt E_{3,k}^2 \tag{G.5a}$$

$$U_{glo} = \epsilon_3^{\varepsilon} wlt E_3^2 \tag{G.5b}$$

$$U = \max\left(U_{loc}, U_{glo}\right) \tag{G.5c}$$

The energy density U' per patch is found by dividing U by the volume $\mathcal{V} = wlt$.

4. The best performing patch passing the strain requirement is found

$$U'_{max} = \max\left(\chi^{\varepsilon} U'\right) \tag{G.6}$$

5. The minimal desired patch efficiency is η_p. A second characteristic function χ^{η} denotes the subset that passes the efficiency criterion and is defined as follows:

$$\chi^{\varepsilon} U' > \eta_p U'_{max} \rightarrow \chi^{\eta} = 1 \tag{G.7a}$$

$$\chi^{\varepsilon} U' < \eta_p U'_{max} \rightarrow \chi^{\eta} = 0 \tag{G.7b}$$

6. Finally the power is calculated by summing the energy from each individual patch and dividing by the simulation time (which represents one revolution of the blade):

$$P = \sum_i \sum_j \frac{\chi^{\eta} U_{i,j}}{t_{max}} \tag{G.8}$$

Appendix H

Lag damper results with SECE circuit

The graphs of figure H.1 supplement the results of section 5.3.2. They visualise the variation of currents and inductances for varying input parameters.

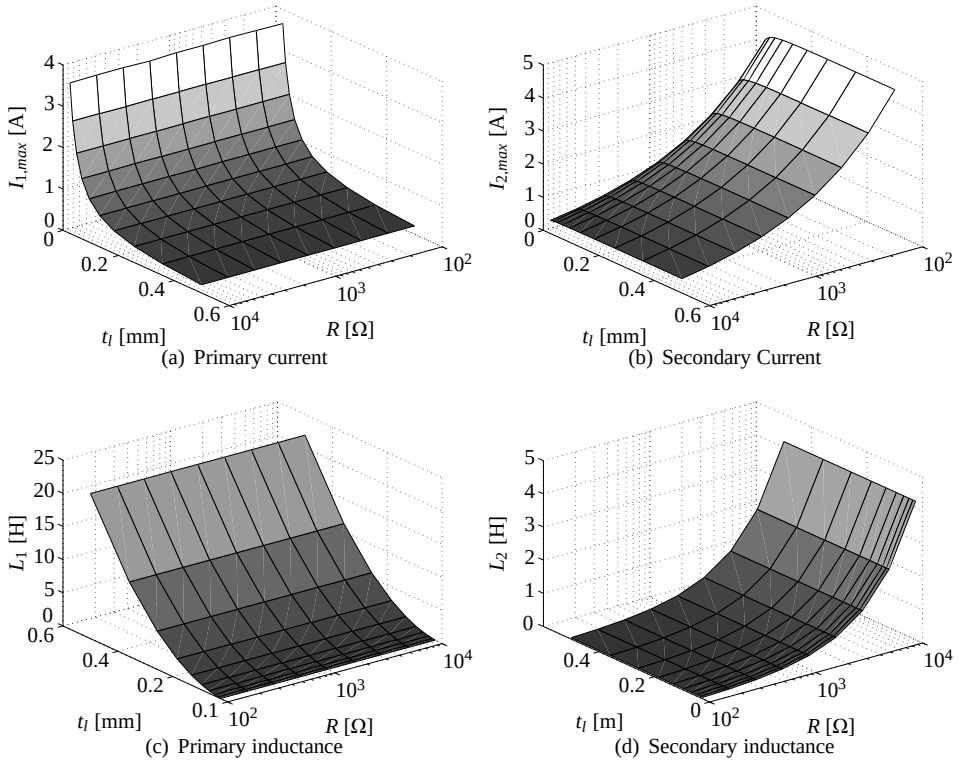

(a) Primary current (b) Secondary Current

(c) Primary inductance (d) Secondary inductance

Figure H.1: Variation of inductances and currents for the coupled inductor in the SECE circuit.

Note the reverse axes in some cases. The realistic cases are those for which the inductance values are below approximately 100 mH when an air core is considered. Inductance L_1 presents the strictest limitation with a layer thickness of at most 50 μm. The maximum load resistance is then 300 Ω. The resulting currents are then $I_1 = 2$ A and $I_2 = 1$ A.

Bibliography

[1] B. Scrosati. History of lithium batteries. *Journal of solid state electrochemistry*, 15:1623–1630, 2011.

[2] G. Moore. Cramming more components onto integrated circuits. *Electronics magazine*, 38, 1965.

[3] C. Geurts, T. Vrouwenvelder, P. van Staalduinen, and J. Reusink. Numerical modelling of rain-wind induced vibrations: Erasmus Bridge, Rotterdam. *Structural Engineering International*, 8:129–135, 1998.

[4] L. Zuo, B. Scully, J. Shestani, and Y. Zhou. Design and characterization of an electromagnetic energy harvester for vehicle suspensions. *Smart Materials and Structures*, 19:045003, 2010.

[5] J. H. Kwon, K. J. Hwang, S. S. Kim, P. J. Kim, and C. S. Kim. Fatigue life evaluation in composite rotor blade of multipurpose helicopter. In *KORUS*, 2002.

[6] E. Head. Blade trouble. Vertical Magazine, February 2012.

[7] C. B. Williams and R. B. Yates. Analysis of a micro-electric generator for microsystems. In *Transducers 95 / Eurosensors IX*, 1995.

[8] V. H. Schmidt. Piezoelectric energy conversion in windmills. In *Ultrasonics Symposium*, 1992.

[9] M. Umeda, K. Nakamura, and S. Ueha. Analysis of the transformation of mechanical impact energy to electric energy using piezoelectric vibrator. *Japanese Journal of Applied Physics*, 35:3267–3273, 1996.

[10] J. Kymissis, C. Kendall, J. Paradiso, and N. Gershenfeld. Parasitic power harvesting in shoes. In *Second IEEE International Conference on Wearable Computing*, 1998.

[11] G. K. Ottman, H. F. Hofmann, A. C. Bhatt, and G. A. Lesieutre. Adaptive piezoelectric energy harvesting circuit for wireless remote power supply. *IEEE Transactions on Power Electronics*, 2002.

[12] G. K. Ottman, H. F. Hofmann, and G. A. Lesieutre. Optimized piezoelectric energy harvesting circuit using step-down converter in discontinuous conduction mode. *IEEE Transactions on Power Electronics*, 2003.

[13] H. A. Sodano, G. Park, and D. J. Inman. Estimation of electric charge output for piezoelectric energy harvesting. *Strain*, 40(2):49–58, 2004.

[14] Y. B. Jeon, R. Sood, J. h. Jeong, and S.-G. Kim. MEMS power generator with transverse mode thin film PZT. *Sensors and Actuators A: Physical*, 2005.

[15] M. Goldfarb and L. D. Jones. On the efficiency of electric power generation with piezoelectric ceramic. *Transaction of the ASME*, 121:566–571, 1999.

[16] A. Badel, D. Guyomar, E. Lefeuvre, and C. Richard. Efficiency enhancement of a piezoelectric energy harvesting device in pulsed operation by synchronous charge inversion. *Journal of Intelligent Material Systems and Structures*, 16, 2005.

[17] E. Lefeuvre, A. Badel, C. Richard, and D. Guyomar. Piezoelectric energy harvesting device optimization by synchronous charge extraction. *Journal of Intelligent Material Systems and Structures*, 16:865–876, 2005.

[18] A. Badel, D. Guyomar, E. Lefeuvre, and C. Richard. Piezoelectric energy harvesting using a synchronized switch technique. *Journal of Intelligent Material Systems and Structures*, 17, 2006.

[19] E. Lefeuvre, A. Badel, C. Richard, L. Petit, and D. Guyomar. A comparison between several vibration-powered piezoelectric generators for stand-alone systems. *Sensors and Actuators A: Physical*, 126:405–416, 2006.

[20] Y. C. Shu and I. C. Lien. Analysis of power output for piezoelectric energy harvesting systems. *Smart Materials and Structures*, 15:1499–1512, 2006.

[21] M. Lallart, E. Lefeuvre, C. Richard, and D. Guyomar. Self-powered circuit for broadband, multimodal piezoelectric vibration control. *Sensors and Actuators A: Physical*, 143:377–382, 2007.

[22] Y. C. Shu, I. C. Lien, and W. J. Wu. An improved analysis of the SSHI interface in piezoelectric energy harvesting. *Smart Materials and Structures*, 16:2253–2264, 2007.

[23] M. Lallart, L. Garbuio, L. Petit, C. Richard, and D. Guyomar. Double synchronized switch harvesting (DSSH): A new energy harvesting scheme for efficient energy extraction. *IEEE Transaction on Ultrasonics, Ferroelectrics and Frequency Control*, 55(10), October 2008.

[24] M. Lallart, D. Guyomar, Y. Jayet, L. Petit, E. Lefeuvre, T. Monnier, P. Guy, and C. Richard. Synchronized switch harvesting applied to self-powered smart systems: Piezoactive microgenerators for autonomous wireless receivers. *Sensors and Actuators A: Physical*, pages 263–272, 2008.

[25] M. Lallart and D. Guyomar. An optimized self-powered switching circuit for non-linear energy harvesting with low voltage. *Smart Materials and Structures*, 17:1–8, 2008.

[26] J. Dicken, P. D. Mitcheson, I. Stoianov, and E. M. Yeatman. Increased power output from piezoelectric energy harvesters by pre-biasing. In *PowerMEMS*, December 2009.

[27] J. Liang and W-H Liao. Improved design and analysis of self-powered synchronized switch interface circuit for piezoelectric energy harvesting systems. *IEEE Transactions on indstrial electronics*, 59(4):1950–1960, 2012.

[28] M. Ferrari, V. Ferrari, M. Guizzetti, D. Marioli, and A. Taroni. Piezoelectric multifrequency energy convertor for power harvesting in autonomous microsystems. *Sensors and Actuators A: Physical*, 142:329–335, 2007.

[29] I. Sari, T. Balkan, and H. Kulah. A wideband electromagnetic micro power generator for wireless microsystems. In *Transducers and Eurosensors '07*, 2007.

[30] M. O. Mansour, M. H. Arafa, and S. M. Megahed. Resonator with magnetically adjustable natural frequency for vibration energy harvesting. *Sensors and Actuators A: Physical*, 2010.

[31] H. Kulah and K. Najafi. Energy scavenging from low-frequency vibrations by using frequency up-conversion for wireless sensor applications. *IEEE Sensors Journal*, 8:261–268, 2008.

[32] A. M. Wickenheiser and E. Garcia. Broadband vibration-based energy harvesting improvement through frequency up-conversion by magnetic excitation. *Smart materials and Structures*, 19(5), 2010.

[33] A. Dogan, J. F. Fernandez, K. Uchino, and R. E. Newnham. The "cymbal" electromechanical actuator. In *IEEE International Symposium on Applications of Ferroelectrics*, pages 213–216, 1996.

[34] B. Zheng, C.-J. Chang, and H. C. Gea. Topology optimization of energy harvesting devices using piezoelectric materials. *Structural and Multidisciplinary Optimization*, 38:17–23, 2009.

[35] D. Benasciutti, L. Moro, S. Zelenika, and E. Brusa. Vibration energy scavenging via piezoelectric bimorphs of optimized shapes. *Microsystem Technologies*, 16:657–668, 2010.

[36] C. Rupp, A Evgrafov, K. Maute, and M. L. Dunn. Design of piezoelectric energy harvesting systems: A topology optimization approach based on multilayer plates and shells. *Journal of Intelligent Materials Systems and Structures*, 2009.

[37] J. M. Dietl and E. Garcia. Beam shape optimization for power harvesting. *Journal of Intelligent Material Systems and Structures*, 21:633–646, April 2010.

[38] S. Roundy, P. K. Wright, and J. Rabaey. A study of low level vibrations as a power source for wireless sensor nodes. *Computer communications*, 26:1131–1144, 2003.

[39] S. Roundy. On the effectiveness of vibration based energy harvesting. *Journal of Intelligent Material Systems and Structures*, 16:809–823, 2005.

[40] D. L. Chandler. More power from bumps in the road, February 2009.

[41] J. C. Maxwell. A dynamical theory of the electromagnetic field. *Proceedings of the Royal Society of London*, 13:531–536, 1863.

[42] J. D. Snodgrass and O. D. McMasters. High performance rare earth-transition metal magnetostrictive materials. *USA, Patent No. 6,273,966*, 2001.

[43] I. Newton. *Philosophiae Naturalis Principia Mathematica*. Halley, 1687.

[44] PI Ceramic. Accessed 4-5-12.

[45] G. W. Taylor, J. R. Burns, S. M. Kammann, W. B. Powers, and T. R. Welsh. The energy harvesting eel: A small subsurface ocean/river power generator. *IEEE Journal of Oceanic Engineering*, 2001.

[46] S. Jansma. The feasibility and design of piezoelectric energy harvester for civil applications. Master thesis, University of Twente, 2010.

[47] R. Huinink. Energy harvesting with piezoelectric material. Master thesis, University of Twente, 2011.

[48] R. Southey. *The story of the three bears*. Anonymous, 1837.

[49] P. J. Sloetjes and A. de Boer. Vibration reduction and power generation with piezoceramic sheets mounted to a flexible shaft. *Journal of Intelligent Material Systems and Structures*, 2007.

[50] P. Curie and J. Curie. Développement, par pression, de l'électricité polaire dans les cristaux hémièdres à faces inclinées. *Comptes rendus hebdomadaires des séances de l'Académie des sciences*, 91:294–295, 1880.

[51] J. Holterman and P. Groen. *An Introduction to Piezoelectric Materials and Components*. Stichting Applied Piezo, the Netherlands, 2012.

[52] A. H. Meitzler, D. Berlincourt, F. S. Welsh, H. F. Tiersten, G. A. Coquin, and A. W. Warner. IEEE standard on piezoelectricity. *IEEE*, 1987.

[53] P. Horowitz and W. Hill. *The Art of Electronics*. Cambridge University Press, 2nd edition, 1989.

[54] G. S. Ohm. *Die galvanische Kette, mathematisch bearbeitet*. T. H. Riemann, 1827.

[55] M. Oude Nijhuis. *Analysis Tools for the Design of Active Structural Acoustic Control Systems*. PhD thesis, University of Twente, 2003.

[56] Y. C. Shu and I. C. Lien. Efficiency of energy conversion for a piezoelectric power harvesting system. *Journal of micromechanics and microengineering*, 16:2429–2438, 2006.

[57] S. Kirchhhoff. Ueber den durchgang eins elektrischen stromes durch eine ebene, insbesondere durch eine kreisförmige. *Annalen der Physik*, 140:497–514, 1845.

[58] L Meirovitch. *Fundamentals of Vibrations*. McGraw Hill, 2001.

[59] W. Maybury, A. Visingardy, S.C. van't Hoff, J. Betran, and A. de Boer. GRC1.1 Technology Review Document. Technical report, GRC Report CS JU/ITD GRC/RP/1.1/31005, 2010.

[60] P. H. de Jong. A study of power harvesting using piezo material in a helicopter rotor blade. University of Twente - Faculty CTW - SD & A group, September 2009.

[61] W. Maybury, A. D'Andrea, R. Hilditch, P. Beaumier, and C. Garcia-Duffy. Baseline blade definition for GRC1.1. GRC technical report CS JU/ITD GRC/RP/1.1/31002, Green Rotorcraft, 2009.

[62] J. D. Anderson Jr. *Introduction to Flight*. McGraw-Hill, 1st international edition, 2000.

[63] J. B. J. Fourier. *Théorie analytique de la chaleur*. Chez Firmin Didot, père et fils, 1822.

[64] M. Moreno-Caracciolo. The 'autogiro'. Ingeniera y Construcción, March 1923.

[65] A. R. A. Paternoster. *Smart Actuation Mechanism for Helicopter rotor blades - Design case for Mach-scaled model blade*. PhD thesis, University of Twente, 2013.

[66] A. Erturk and D. J. Inman. A distributed parameter electromechanical model for cantilevered piezoelectric energy harvesters. *Journal of Vibration and Acoustics*, 130:041002–1 – 041002–15, 2008.

[67] S. D. Poisson. Note sur l'extension des fils et des plaques élastiques. *Annales de chimie et de physique*, 1827.

[68] A. Erturk, P. A. Tarazaga, J. R. Farmer, and D. J. Inman. Effect of strain nodes and electrode configuration on piezoelectric energy harvesting from cantilevered beams. *Journal of Vibration and Acoustics*, 131:011010–1 – 011010–11, 2009.

[69] P. H. de Jong. Power harvesting in a helicopter rotor using a piezo stack in the lag damper. Technical Report CS JU/ITD GRC/RP/1.8/31017, University of Twente, April 2011.

[70] P. H. de Jong, A. de Boer, R. Loendersloot, and P. J. M. van der Hoogt. Power harvesting in a helicopter rotor using a piezo stack in the lag damper. *Journal of Intelligent Materials Systems and Structures*, 2012.

[71] P. H. de Jong. Power harvesting in a helicopter lag damper. In *International Workshop on Piezoelectric Materials and Actuators*, 2011.

[72] A. R. S. S. Bramwell, G. Done, and D. Balmford. *Bramwell's Helicopter Dynamics*. AIAA, 2nd edition, 2001.

[73] Z. A. Anderson. Regenerative dampers: Harvesting linear kinetic energy. In *Electric Vehicles: Land, sea & air*, 2011.

[74] J. Feenstra, J. Granstrom, and H. Sodano. Energy harvesting through a backpack employing a mechanically amplified piezoelectric stack. *Mechanical systems and signal processing*, 22:721–734, 2008.

[75] L. F. Shampine. *Numerical Solution of Ordinary Differential Equations*. Chapman & Hall, 1997.

[76] D. Guyomar, A. Badel, E Lefeuvre, and C. Richard. Toward energy harvesting using active materials and conversion improvement by nonlinear processing. *IEEE Transactions on Ultrasonics, ferroelectrics and frequency control*, 52:584–595, 2005.

[77] G. Yang, Z. Yue, Y. Ji, and L. Li. Dielectric nonlinearity of stack piezoelectric actuator under the combined uniaxial mechanical and electric loads. *Journal of Applied Physics*, 104, 2008.

[78] K. Schroeder, W. Ecke, J Apitz, E Lembke, and G. Lenschow. A fibre bragg grating sensor system monitors operational load in a wind turbine rotor blade. *Measurement Science and Technology*, 17:1167–1172, 2006.

[79] Y. Liu, A. Lacher, G. Wang, A. Purekar, and M. Yu. Wireless fiber optic sensor system for strain and pressure measurements on a rotor blade. In *Fiber Optic Sensors and Applications V*. SPIE, October 2007.

[80] P. H. de Jong, A. de Boer, R. Loendersloot, and P. J. M. van der Hoogt. Lab-scale experimental validation of a piezoelectric energy harvesting lag damper. In *ERF*. ERF, September 2012.

[81] Diotec Semiconductor. B40R - B500R datasheet. www.datasheetcatalog.org, 2001.

[82] Fairchild Semiconductor. BD135/137/139 datasheet. www.datasheetcatalog.org, 2000.

[83] Fairchild Semiconductor. BC556 / 557 / 558 / 559 / 560 datasheet. www.datasheetcatalog.org, 2002.

[84] D. G. Fink and D. Christiansen. *Electronics Engineers' Handbook*. McGraw Hill, 1989.

[85] Fairchild Semiconductor. 2N7000 / 2N7002 / NDS7002A N-channel enhancement mode field effect transistor datasheet. www.datasheetcatalog.org, 1995.

Scientific appendix

Journal papers

- P. H. de Jong, A. de Boer, R. Loendersloot, and P. J. M. van der Hoogt. Power harvesting in a helicopter rotor using a piezo stack in the lag damper. *Journal of Intelligent Materials Systems and Structures*, 2012.

Conference papers

- P. H. de Jong, A. de Boer, R. Loendersloot, and P. J. M. van der Hoogt. Lab-scale experimental validation of a piezoelectric energy harvesting lag damper. In *ERF*. ERF, September 2012.
- P. H. de Jong, A. de Boer, R. Loendersloot, and P. J. M. van der Hoogt. Power harvesting in a helicopter lag damper. In *ERF*. ERF, September 2011.
- P. H. de Jong, A. de Boer, R. Loendersloot and P. J. M. van der Hoogt. Power harvesting in a helicopter lag damper. In *SMART11*, Fraunhofer IZFP, July 2011.
- P. H. de Jong, A. de Boer, R. Loendersloot, and P. J. M. van der Hoogt. Power harvesting using piezo material in a helicopter rotor blade. In *ICSV17*, ICSV, July 2010.

Conference presentations

- P. H. de Jong. Power harvesting in a helicopter lag damper. In *International Workshop on Piezoelectric Materials and Actuators*, 2011.

Book chapters

- A. R. A. Paternoster, P. H. de Jong and A. de Boer. Piezoelectric energy conversions. In: A. Reinders, J. Carel Diehl and H. Brezet. *The Power of Design: Product Innovation in Sustainable Energy Technologies.* Wiley, 1st edition, 2012.

Technical reports

- P. H. de Jong. A preliminary investigation in to using model predictive control for the Gurney Flap mechansm. In: M. Pavel and M. Jones. Assessment of open loop effects of an active Gurney Flap System. GRC Technical Report CS JU/ITD GRC/RP/1.9/31033, 2011.

- P. H. de Jong and R. Loendersloot. Power harvesting in a helicopter rotor using a piezo stack in the lag damper. GRC Technical Report CS JU/ITD GRC/RP/1.8/31017, University of Twente, April 2011.

- P. H. de Jong. Power harvesting with piezo elements in the blade. In: W. Maybury, A. Visingardy, S.C. van't Hoff, J. Betran, and A. de Boer. GRC1.1 Technology Review Document. GRC Technical report, GRC Report CS JU/ITD GRC/RP/ 1.1/31005, 2010.

- P. H. de Jong. A study of power harvesting using piezo material in a helicopter rotor blade. University of Twente - Faculty CTW - Applied Mechanics group, September 2009.

Dankwoord

Pff, het is zover. Ik mag aan het dankwoord beginnen! Op het drukken en last-minute fine-tuning na is dit zo ongeveer de laatste formaliteit in het proefschrift. Het resultaat van 4 jaar werken, onderzoeken, frustratie en meetresultaten. Die andere formaliteiten doe je echter de dag voor het naar de drukker moet en kenmerken zich weer door paniek, zenuwen en stress. Anyhoo, to the point:

Allereerst dank ik Richard en André. Richard voor de dagelijkse begeleiding en de bakken met commentaar. Al jouw papieren zullen nog goed van pas komen voor het aanmaken van de barbecue! Hoewel je veel commentaar gaf, waren het vaak wel details die er toe deden. André is de andere kant van het spectrum. U keek naar de hoofdlijnen, structuur en hield het in goede banen. De onzichtbare hand die ongemerkt toch de deadlines kon pushen.

Als derde komt Alex. We hebben aan hetzelfde project gewerkt en hebben veel aan elkaar gehad. Niet alleen wat kennis betreft maar ook gezelligheid en onzin. Bedankt voor de LaTeX skills en het photoshoppen van enkele van mijn plaatjes, alsmede de kaft van dit proefschrift. Mijn excuses voor alle flauwe taalgrapjes... not! De ongewapende hamsters en opgewarmde (of waren het opgegeten?) lunches vlogen mij soms om de oren. Dat heet ‘een schot voor open doel’ in Nederland. Aan Charlène ben ik mijn excuses verschuldigd: S’il jure plus ces derniers temps, c’est de ma faute!

De kamergenoten, huidig en oud: Derka Derka, Urjun, Jurnan, Samuelle, Roel en Pablo. Met zijn allen hebben we flink aan onze voetbaltafelskills gewerkt. Roel, als afstudeerder was je ook super om mee te werken. Geen gelul, gewoon gaan en aan het einde van de dag een biertje. Totdat je zonder te morren in de blubber lag om je opstelling koste wat kost te fixen. Dat is nog eens aanpakken!

Bert en Axel voor de assistentie in het lab. Jullie hebben mooi spul staan waar ik als lomperik leuk mee zou kunnen spelen. Jammer dat het allemaal zo duur is!

Verder heel veel collega’s, in het bijzonder: Debbie voor het regelen van vanalles, van gratis kroketten tot vliegtickets. Al die flessen rum die ik heb meegenomen uit Oostenrijk is wel het minste wat ik terug kon doen! Knul, Erwin, je bent dan wel een stuk ouder maar wij hebben gelijke meningen en gedeelde humor. Ik heb enorm genoten van de collegialiteit. Sybren, als afstudeerder heb jij ook bijgedragen aan mijn begrip van het onderwerp. Voor een IOer heb je het niet slecht gedaan! Als extra tafelvoetballers ook nog Axel en de afvalligen Can en Anne. Can, de reis in Egypte na de conferentie was echt top, je bent een relaxte peer om mee op pad te gaan.

Ook de mannen van de werkplaats kan ik niet vergeten. Norbert, Theo, Theo, Leo,

Joop, Sprenkie en Jacob. Al sinds halverwege de studie mocht ik daar klooien aan studiegerelateerde of eigen projecten. Van het openfrezen van mijn kapotte versnellingsbak, het wikkelen van de laatste spoel voor mijn onderzoek en vorige week (!!) nog het beshcikbaar stellen voor ruimte ten behoeve van het spuiten en afbakken van de remklauwen van mijn auto. Dank voor de bijgebrachte werkplaats skills.

En dan nog de verplichte maar betekenisvolle alinea met namen die toch op de een of andere manier de tijd hebben gevonden mij te helpen met kleinigheidjes, of mijn tijd hier aangenamer hebben gemaakt. De EL-ers Jeroen Korterik, Henny Kuipers, Bram Verhoef en Tom van Hemert. De laatste ook als huisgenoot natuurlijk bedankt! Ik heb vast veel te veel geprofiteerd van jouw netheid en hopelijk reken je me dat niet teveel aan. Bjorn, Juan Carlos, Giovani, Juan, bRAXIS en iedereen die ik vergeet expliciet te melden. Bedankt voor de biertjes, gezelligheid, films, kerstdiners en al dat andere. Tim, succes nog met jouw laatste promotie-loodjes, hou je taai!

Mijn beste vrienden mogen uiteraad niet ontbreken: Toby, Lars en Dagmar. Jullie hebben een hoop van mijn frustraties aan mogen horen op alle gebieden van het leven maar we hebben ook mooie tijden beleefd. Onze vakanties waren briljant! Het eerste ‘lustrum’ is geweest en was een mooi weekend relaxen alvorens ik begon met de laatste push voor het proefschrift. Ik zeg op naar de tiende (lustrum welteverstaan, niet proefschrift). Tot we met rollators nog de wereld over reizen!

And of course the parental units, bro and sissy, for being here (I can’t be sure now, let’s hope the Eyjafjallajökull doesn’t almost screw this one up...) and around. Mom for keeping me decent, and dad for screwing it up again.

Dat is het, tijd voor vakantie! Whoohoo!

UNIVERSITY OF TWENTE.